INFORMATION TO USERS

This manuscript has been reproduced from the microfilm master. UMI films the text directly from the original or copy submitted. Thus, some thesis and dissertation copies are in typewriter face, while others may be from any type of computer printer.

The quality of this reproduction is dependent upon the quality of the copy submitted. Broken or indistinct print, colored or poor quality illustrations and photographs, print bleedthrough, substandard margins, and improper alignment can adversely affect reproduction.

In the unlikely event that the author did not send UMI a complete manuscript and there are missing pages, these will be noted. Also, if unauthorized copyright material had to be removed, a note will indicate the deletion.

Oversize materials (e.g., maps, drawings, charts) are reproduced by sectioning the original, beginning at the upper left-hand corner and continuing from left to right in equal sections with small overlaps.

Photographs included in the original manuscript have been reproduced xerographically in this copy. Higher quality 6" x 9" black and white photographic prints are available for any photographs or illustrations appearing in this copy for an additional charge. Contact UMI directly to order.

Bell & Howell Information and Learning
300 North Zeeb Road, Ann Arbor, MI 48106-1346 USA

UMI®
800-521-0600

DIFFUSION STUDIES IN InGaAs/GaAs AND AlGaAs/GaAs QUANTUM WELL STRUCTURES.

By

Kartik Ramanujachar, B.Tech.

M.Eng.

A Thesis

Submitted to the School of Graduate Studies

in Partial Fulfilment of the Requirements

for the Degree

Doctor of Philosophy

McMaster University

© Copyright by Kartik Ramanujachar, June 1998.

DIFFUSION STUDIES IN InGaAs/GaAs AND AlGaAs/GaAs QUANTUM WELL STRUCTURES.

"Would you tell me, please, which way I ought to go from here?" "That depends a good deal on where you want to get to," said the Cat. " I don't much care where," said Alice. "Then it doesn't matter which way you go," said the Cat. " So long as I get somewhere," Alice added as an explanation. " Oh, you're sure to do that," said the Cat, " if only you walk long enough."

Lewis Carroll. Alice and the Cheshire Cat.

To my parents, Ramya and Suresh.

DOCTOR OF PHILOSOPHY (1998) McMaster University

(Materials Science and Engineering) Hamilton, Ontario

TITLE: DIFFUSION STUDIES IN InGaAs/GaAs AND AlGaAs/GaAs QUANTUM WELL STRUCTURES.

AUTHOR : Kartik Ramanujachar, B.TECH (Indian Institute of Technology, Kanpur, INDIA)
M.Eng (McMaster University, Hamilton, Ontario Canada)

SUPERVISORS : Dr G.C. Weatherly
Dr G. Purdy.

NUMBER OF PAGES: xvi, 191.

ABSTRACT

This work has involved a study of diffusion and ion implantation enhanced diffusion in GaAs based semiconductor heterostructures. A knowledge of kinetic parameters underlying the diffusion process is of practical value in the fabrication of optoelectronic devices. Two main problems have been explored.

(a) **Thermal interdiffusion of (InGaAs/GaAs)quantum well structures and superlattices.**

Transmission electron microscopy, X-ray diffraction and photoluminescence experiments have been undertaken to follow the temporal evolution of the indium composition during annealing of the superlattice. A linear model of diffusion has been utilized to calculate the evolution of strain, indium composition and the X-ray diffraction intensity during annealing. Calculation of energy levels of the electrons and holes in the superlattice structure and their evolution with annealing have also been performed following a transfer matrix approach. This has been used to predict the experimentally observed trends in photoluminescence. Non linear aspects of diffusion including composition dependence and strain dependence (by growth on 311A substrates) have also been experimentally examined.

(b) **Ion implantation enhanced disordering of III-V compound semiconductor heterostructures (InGaAs/GaAs, GaAs/AlGaAs).**

Various parameters which influence the disordering process, namely the implant energy, ion species, implant temperature and heterostructure composition have been studied with transmission electron microscopy (conventional/high resolution) and photoluminescence techniques. Several interesting phenomena with respect to the position and crystallographic nature of implant damage have been observed. A phenomenological model to rationalize data has been developed by numerically solving the governing diffusion equations.

ACKNOWLEDGMENTS.

I would like to thank my supervisors, Dr G.C. Weatherly and Dr G. Purdy and the third member of my supervisory committee, Dr D.A.Thompson, for their encouragement and support throughout the Ph.D. program.

This work would not have been possible without the help of a number of people. Specifically I would like to thank Dr. S. Charbonneau for providing many of the samples used in this study and for help in acquiring data at the National Research Council of Canada at Ottawa. Help extended by Dr. I.V. Mitchell and Dr. R.D. Goldberg of the University of Western Ontario in implanting samples is greatly appreciated. Many interdiffusion experiments were run on M.B.E. samples grown by Dr. B.J. Robinson and Mr S. McMaster. I would like to thank Ms. D. Stevanovic for help with ion implantation and rapid thermal annealing. Jim Garrett has made possible the entire set of experiments on long term annealing of superlattice structures. Fred Pearson and Andy Duft were of invaluable help in TEM work.

As my formal education draws to a close, I am more than ever struck by the fact that none of this would ever have been possible without the constant encouragement of

my parents and sister. Specifically my father at times has been so concerned about the progress of this thesis, to almost qualify as supervisor in absentia! It is to them that I would like to dedicate this work.

TABLE OF CONTENTS.

1. **Chapter 1.** **pg**
Introduction. 1

2. **Chapter 2.**
Literature Review. 4

2.1.1 III-V compounds 4

2.1.2. Diffusion in GaAs based compound semiconductors. 13

2.2. Quantum well structures. 14

2.2.1. Particle in a one dimensional potential well. 14

2.2.2. Tunneling and one dimensional potential wells. 16

2.2.3. Absorption spectra of single quantum well structures and superlattices. 18

2.2.4. Devices constructed with quantum well superlattices. 22

2.3. Photoluminescence 24

2.4. Ion implantation enhanced quantum well interdiffusion. 30

2.4.1.Theory of disordering. 30

2.4.2. Implantation studies. 37

3. **Chapter3.**

Experimental Procedures. 46

3.1.

pg

3.1.1. Diffusional homogenization of superlattice structures. (SL10) 46

3.1.2. Annealing. 49

3.1.3. Photoluminescence. 50

3.1.3(b) X-ray Diffraction. 51

3.1.3(c) TEM (Transmission electron Microscopy) 51

3.1.4. Structures grown to investigate the compositional dependence of the diffusion coefficient. (SD10,SD15,SD20,SD25,SD30). 52

3.1.5. Structures grown to study the influence of strain on the diffusion coefficient. (100S3,311S3). 54

3.2

3.2.1.Ion Implantation enhanced diffusion. 55

4. **Chapter 4.**

Experimental Results. 64

4.1. Results from the homogenization of superlattice structures. (SL10) 64

4.1.1. Cross-sectional TEM results. 64

4.1.2. X-Ray diffraction. 68

4.1.3. Photoluminescence. 69

pg

4.1.4. Results from the diffusion of SD samples. 69

4.1.5. Results from the diffusion of 100S3, 311S3 structures. 71

4.2. Experimental findings on the ion implanted and rapid thermally annealed structures. 78

4.2.1. AlGaAs/GaAs structures. 78

4.2.2. (A2) structures. 89

4.2.3. AlGaAs/GaAs/InGaAs based structures (I1, I2) 91

4.2.4. I2 structures. 97

4.2.5. SD structure implantation. 97

5. **Chapter 5.**

Discussion. 102

5.1. Linear model for superlattice homogenization. 103

5.1.2. Computation of strain in the superlattice. 107

5.1.3. Computation of X-ray diffraction from the as grown and annealed structures. 107

5.1.4. Computation of the photoluminescent transition wavelengths. 111

5.1.5. The transfer matrix technique. 112

5.1.6. Discussion of the trends seen in the SD structures. 116

5.1.7. Influence of strain on the diffusion coefficient. 120

5.1.8. Discussion of ion implantation enhanced quantum well interdiffusion. 125

5.1.8.(a) Developing a model for ion implantation enhanced diffusion. 125

pg

5.1.8.(b)Numerical solution of the diffusion equations. 129

5.1.9 Implications of model : General discussion of trends in implantation experiments. 134

6. Chapter 6.
Summary and conclusions. 143

Appendix 1. Basic equations of diffusion. 146

Appendix 2. Monte Carlo/Fourier Transform based composition profile estimation. 149

Appendix 3. Time Resolved Spectroscopy. 167

Appendix 4 Code for the transfer matrix method. 170

Appendix 5. Code for the diffusion calculation. 177

Appendix 6. Contrast computation with the two beam theory of dynamical diffraction. 181

References 185

LIST OF FIGURES

Fig 2.1 A unit cell of the zinc blende structure. In this structure group III atoms occupy open circles and group V atoms occupy solid circles.[1]

Fig 2.2 The variation of band gap with composition for (a) the $Ga_xIn_{1-x}Sb$ ternary system which has a direct band gap over the entire composition range; (b) GaP_xAs_{1-x} alloys in which a transition from a direct to an indirect band gap occurs at x =0.45. [2]

Fig 2.3 A sketch of the relationship between band gap and lattice parameter for the quaternary III-V systems GaInAsP and GaAlAsSb. [2]

Fig 2.4 Composition diagram for $In_{1-x}Ga_xAs_yP_{1-y}$ alloy. The straight line represents the alloy compositions which have the same lattice constant as InP. (Lattice matched to InP). [1].

Fig 2.5 The Schroedinger equation, it's eigenvalues and eigenfunctions for an infinitely deep potential well. As shown, the two wells are of finite depth and apply to the electrons and holes in the GaAs layer of an $Al_{1-x}Ga_xAs$/GaAs heterostructure. [26]

Fig 2.6(a) Schematic representation of a parabolic energy band in the quantum limit. Two dimensional bands in the k_{x-y} plane give rise to a stepped cumulative density of states with increasing energy. [26].

Fig 2.6(b) Tunnel coupling between two wells. [61].

Fig 2.7 Absorption spectra (2K) of 4000, 210, 140 $\overset{0}{A}$ thick GaAs layers between $Al_{0.2}Ga_{0.8}As$ barriers. The quantum size effect manifests itself as an increase in the bulk exciton energy and by the appearance of higher energy peaks in the the thinner layers. [26].

Fig 2.8 Bound states and wave functions of quantized valence and conduction bands demonstrating the $\Delta n=0$ selection rule for interband transitions. [26].

Fig 2.9 Absorption spectrum (2K) of a series of double-well AlGaAs/GaAs structures. The inset is a schematic energy level scheme for a pair of coupled wells. A coupled -well selection rule (see text) limits to four the number of allowed transitions between the six discrete energy levels of the coupled wells. Calculated transition energies are included. [26].

Fig 2.10 (a) Energy level diagrams showing free carrier recombination with carrier close to the band edges of the material (a), electron-hole recombination with excited electron (b) and excited hole (c). [10].

Fig 2.10(b) Shallow transitions shown are (a) acceptor to valence band transition, (b) conduction band to donor transition. Deep transitions are (c) conduction band to acceptor transition and (d) donor to valence band transition. (e) shows a deep level transition. [10].

Fig 2.11 PL system at McMaster University. (For the experiments reported in this thesis a Helium Neon laser was used.)

Fig 2.12 Particle trajectories in the center of mass system, with the superimposed "scattering triangle," comprising the impact parameter P, distance of closest approach r_0, radii of curvature ρ_1 and ρ_2 (curvature of trajectories at closest approach) and correction terms δ_1 and δ_2. From this construction the scattering angle θ can be obtained. [39].

Fig 2.13 Schematic diagram showing the cross section of the quantum well structures used in [42]. The quantum wells are InGaAs and contain 10%,15%,20% and 25% indium respectively.

Fig 2.14 Low temperature (4K) PL spectrum of sample shown in Fig 2.13, before and after broad area ion implantation with $0.6*10^{13}$ ion/cm^2 Ga and annealing at 850^0 C for 60 seconds.

Fig 2.15 Schematic diagram of the structure used for experiments in [43].

Fig 2.16 Low temperature PL spectra of the as grown and implanted (As^+ 8 MeV, $2.5*10^{14}$ ion/cm^2) $In_{0.23}Ga_{0.77}As$ laser structure after annealing. Annealing was conducted at 850^0 C for 90 seconds. [43].

Fig 2.17 Schematic diagram showing the band structure of an InGaAs quantum well of width (w), (a) before and (b) after compositional disordering. [42].

Fig 3.1 High resolution micrograph of the as grown super lattice SL10. The diffraction pattern is inset.

Fig 3.2 As grown SD15 structure. **g** = (200).

Fig 3.3 (a) As grown 100S3 structure. **g** = (200). The indium contents in % are marked on the various wells.

Fig 3.3 (b) As grown 311S3 structure. **g** = (02$\bar{2}$).

Fig 3.4 As grown $Al_{0.7}Ga_{0.3}As$/ GaAs structure (A1). **g** = (002).

Fig 3.5 As grown $Al_{0.2}Ga_{0.8}$ As/GaAs structure (A2). **g** = (002).
(The two GaAs quantum wells are arrowed).

Fig 3.6 As grown AlGaAs/ GaAs/InGaAs graded index structure (I1). **g** = (002).

Fig 3.7 1.1 MeV As^{+} implanted GaAs/InGaAs structure (I2). **g** = (002).

Fig 4.1.1 As grown SL10 structure with diffraction pattern. **g** = (200)
The arrow in the diffraction pattern points to ($\bar{2}$00).

Fig 4.1.2 SL10 structure annealed at 850^{0} C for 20 minutes. **g** = (200)
(Note the superlattice is still visible)

Fig 4.1.3 SL10 structure annealed at 850^{0} C for 6 hours. **g** = (200)
(The superlattice at this stage is diffused out)

Fig 4.1.4 SL10 structure annealed at 850^{0} C for 8 hours. **g** = (200)

Fig 4.1.5 SL10 structure annealed at 850^{0} C for 12 hours **g** = (200)

Fig 4.2 Evolution of the X-ray diffraction intensity with annealing superlattice structure SL10.

Fig 4.3 Evolution of the PL from the superlattice SL10 structure.

Fig 4.4 SD20 structural evolution as a function of annealing temperature. **g** = (200).

Fig 4.5 Trends in the PL intensity from SD20 structure.

Fig 4.6 Evolution of the PL intensity from the [311] A structure.

Fig 4.7 Evolution of the PL intensity from the [100] structure.

Fig 4.8.1 A1 sample implanted with As^{+} 1.1 MeV. **g** = (2$\bar{2}$0)

Fig 4.8.2 A1 sample implanted with As^{+} 2.0 MeV. **g** = (2$\bar{2}$0)

Fig 4.8.3 A1 sample implanted with As^{+} 6.0 MeV. **g** = ($\bar{2}$20)

Fig 4.8.4 A1 sample implanted with As^+ 8.0 MeV. **g** = (004)

Fig 4.8.5 TRIM predictions of vacancy profiles in A1 samples after As^+ implants at varying energies. The approximate centres of the quantum wells are marked.

Fig 4.9 Evolution of well thickness in A1 sample with implant energy. As grown, As^+ 1.1 MeV, As^+ 8.0 MeV. **g** = (002)

Fig 4.10.1 Lower GaAs quantum well in A1 structure. R.T.A. only.

Fig 4.10.2 Lower GaAs quantum well in A1 structure. As^+ 8.0 MeV implant,105 second R.T.A. at 850 ^{0} C.

Fig 4.11 Implant and R.T.A. portion of sample A2 implanted with As^+ at 6 MeV. **g** = $(2\bar{2}0)$.

Fig 4.12 Evolution of the PL from I1 structures as a function of implant energy.

Fig 4.14(a) R.T.A. only portion of sample I1. **g** = (002).

Fig 4.14(b) Implanted with As^+ at 5 MeV and R.T.A at 850 ^{0} C for 90 seconds. **g** = (002).

Fig 4.14(c) Clustering of implant damage on GaAs planarization layers in I1. **g** = (004).

Fig 4.14(d) Fringes seen in dark field **g** = $(1\bar{1}1)$ image from 5 MeV As^+ implanted I1 sample, probably arising from composition modulations.

Fig 4.15.1 7 MeV As^+ implanted I1 sample (77K). R.T.A. at 850 ^{0} C for 90 seconds. **g** = $(\bar{2}2\bar{2})$.

Fig 4.15.2 7 MeV As^+ implanted I1 sample (300K). R.T.A. at 850 ^{0} C for 90 seconds. **g** = $(02\bar{2})$.

Fig 4.16.1 Doped I1 sample imaged near [110] zone axis. As^+ implanted at 1.0 MeV. **g** = (002)

Fig 4.16.2 Undoped I1 sample. As^+ implanted at 1.0 MeV. **g** = (002).

Fig 4.17(a) 1.1 MeV As^+ implanted I2 sample. **g** = $(0\,0\,\bar{4})$.

Fig 4.17(b) 8 MeV As^+ implanted I2 sample. g = (0 0 4).

Fig 5.1 Evolution of the concentration of the SL10 superlattice computed in a linear diffusion approximation.

Fig 5.2 Computed X-ray diffraction from as grown SL10 superlattice.

Fig 5.3 X-ray profile from 8 hours annealed SL10 superlattice.

Fig 5.4 Results of the transfer matrix calculation for the energy of the electron in in the SL10 structure annealed for 6 hours.

Fig 5.5 Node configuration for finite difference calculation.

Fig 5.6 (a) Vacancy and interstitial evolution after annealing at 850^0 C for 30 seconds. (6 MeV implant).

Fig 5.6(b) GaAs well evolution after 30 seconds and 90 seconds annealing at 850^0 C.

Fig 5.7(a) Evolution of the vacancy and interstitial profile after annealing at 850^0 C for 30 seconds. (2 MeV implant)

Fig 5.7(b) GaAs well after diffusion at 850^0 C for 30 seconds.

Fig 5.8 Evolution of $In_{0.2}Ga_{0.8}As$ quantum wells after diffusion at 850^0 C for 90 seconds. (5 MeV implant).

Fig 5.9 Evolution of the vacancy and interstitial concentration with 90 seconds annealing at 850^0 C.

Fig A2.1 Deconvoluted profile of single quantum well in SD20 structure annealed at 750^0 C for 8 hours.

Fig A2.2 Deconvoluted profile of single quantum well in SD20 structure annealed at 800^0 C for 8 hours.

Fig A3 Time resolved spectrum from SD20 structure.

Fig A6.1 Indium concentration profile.

Fig A6.2 Computed transmitted intensity.

List of tables.

pg

Table 4.1. Comparison of blue shifts from SD samples with various indium contents. 76

Table 4.2. Structure A1. Implant energies, blue shifts and well thickness after RTA at 850^0C for 105 seconds. 85

Table 4.3. Blue shift of SD type samples with implant dose. 101

Table 5.1. Results of the transfer matrix calculation for the transition wavelength, on annealing superlattice SL10 for varying periods of time. 116

Table 5.2. Transfer matrix results for the blue shift of luminescence from wells of different indium contents diffused at 850^0C for 8 hours. 120

Chapter 1.

INTRODUCTION.

This thesis is concerned with a study of diffusion and ion-implantation enhanced diffusion in GaAs and related compounds InGaAs and AlGaAs. Two problems were studied. The first of them is an examination of the annealing behavior of $In_{0.2}Ga_{0.8}As$ /GaAs based superlattice structures. These superlattice structures have been heat treated at 850 ^{0}C for various periods of time (ranging from 20 minutes to 12 hours) and the evolution of the composition profile followed. Associated experiments to study the composition and the strain dependence of the diffusion coefficient have also been undertaken. Two principal techniques have been utilized to follow the temporal evolution of composition. The first of them is photoluminescence (PL). In this technique compositional information has been obtained by studying the wavelengths of spontaneous emission from the diffused structures. The second technique is one of physical examination with cross-sectional transmission electron microscopy (XTEM).

The second problem which has been examined is ion-implantation enhanced quantum well interdiffusion. In these experiments the quantum well structures (InGaAs/GaAs, AlGaAs/GaAs) have been implanted with Ga^+ or As^+ ions, rapid thermally annealed at 850^0 C (for time periods typically of several tens of seconds) and

their interdiffusion followed with the same techniques of PL and XTEM. Both low energy (100 keV) and high energy (~5 MeV) implants have been studied.

The thesis is organized as follows. In Chapter 2, a literature review which surveys some of the areas of relevance to the problem is undertaken. Published work in the area of III-V compound semiconductor diffusion is reviewed. The existing theory of ion-implantation enhanced diffusion is elucidated. Chapters 3 and 4 present the experimental procedures and results. Chapter 3 is concerned with the details of the various structures examined, the diffusion experiments, the ion implantation enhanced diffusion experiments, PL and XTEM. Chapter 4 presents the results of the XTEM characterization experiments, PL and X-ray diffraction spectra. Chapter 5 is devoted to the development of a linear model of diffusion for the superlattice structures and a calculation of the PL transition wavelengths. In this model the effect of composition and strain on the interdiffusion coefficient is neglected and the temporal evolution of the indium (/aluminium) composition is obtained by convoluting the initial concentration profile with a Gaussian point spread function. This Gaussian point spread function is the solution of the diffusion equation for a Dirac delta function shaped initial concentration profile. The ability of a linear diffusion model in explaining the observed experimental trends is demonstrated. A model for ion-implantation enhanced diffusion is also developed. In this latter model the diffusion coefficient is allowed to vary both with position in the structure and with time. On the basis of this model a rationalization of the

main trends seen in the experiments on diffusional enhancement are also presented. Appendices are provided for the various computer programs developed to support the discussion of Chapter 5.

Chapter 2.

LITERATURE REVIEW

The crystallography and electronic properties of III-V compound semiconductor materials, followed by the basic physics of quantum well structures and superlattices are first reviewed. In order to review the theory of ion -implantation enhanced diffusion, a number of topics are considered. These include the penetration of ions into solids and diffusion mechanisms in III-V compound semiconductor materials. A brief review of the transitions involved in photoluminescence is presented. The review concludes with the published theory of ion-implantation enhanced diffusion and rationalisation of the trends seen in luminescence from implanted structures.

2.1

2.1.1 III-V Compounds

III-V compound semiconductors are extensively used for the fabrication of optoelectronic devices. This class includes binary compounds like GaAs or InP, ternary compounds like AlGaAs or GaAsSb and quaternary compounds such as InGaAsP. These III-V compound semiconductors have a sphalerite crystal structure which consists of two interpenetrating F.C.C. lattices, Fig(2.1) [1], with the second F.C.C. lattice at position (1/4a, 1/4a, 1/4a) with respect to the first. In a binary compound the two sublattices consist of the group III atoms and the group V atoms respectively. This arrangement of atoms makes the (111) plane and the ($\bar{1}\,\bar{1}\,\bar{1}$) dissimilar with the (111)

planes containing atoms of one kind and the ($\bar{1}\,\bar{1}\,\bar{1}$) planes containing the other. This makes their properties anisotropic. For example, the chemical dissolution and etching rates are very different on these surfaces.

When ternary or quaternary compounds are considered the group III alloying elements substitute on the group III sublattice and the group V atoms substitute on the group V sublattice. The ternary and quaternary compounds can be considered as constituted by appropriate binary compounds; for example an alloy of the kind $A_{(1-x)}B_xC$ can be considered as being composed of (1-x) moles of the binary AC and x moles of the binary BC. Substitution can occur either on the group III or the group V sublattice. The same approach can be extended to a description of quaternary compounds. In this case substitution occurs on both the group III and group V sublattices.

The binary compounds like GaAs and InP are characterized by unit cells with large lattice constants in the range of 0.5-0.65 nanometers. Additionally the band gap of binary III -V compounds lie in the range of 0-3 eV. This range is however not sufficient to cover the entire range of potential device applications. This is because of the difficulty in preparing pure and defect free material for some applications and the necessity to have very precise band gaps for many optoelectronic applications. Consequently considerable advantage has been taken of ternary and quaternary alloys wherein it is possible to vary

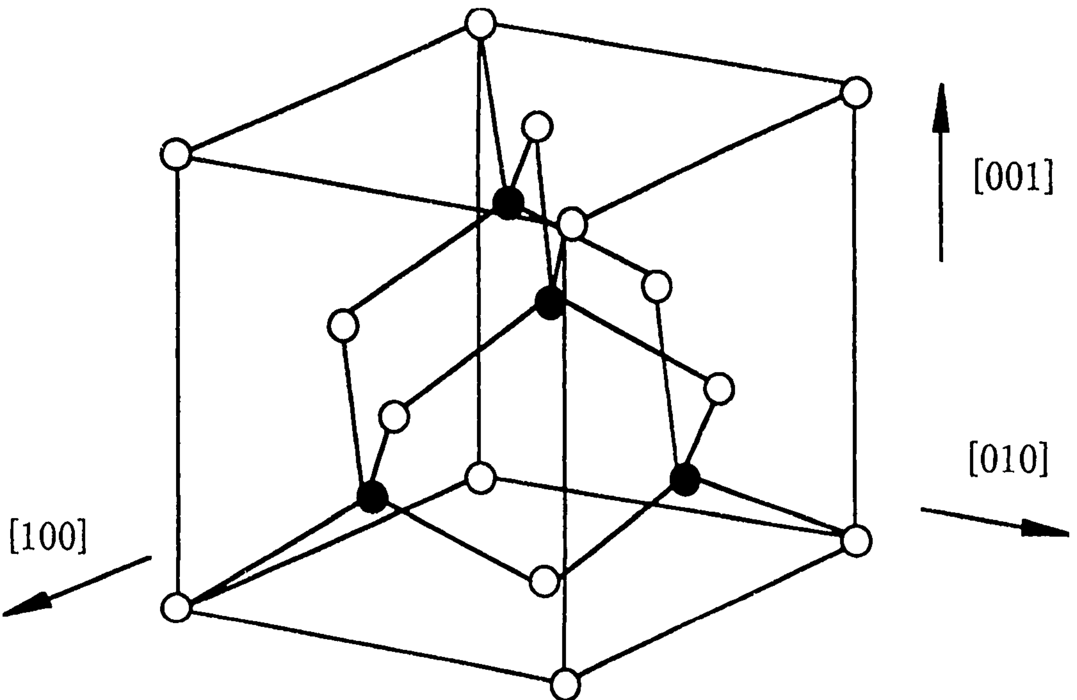

Fig 2.1 A unit cell of the zinc blende structure. In this structure group III atoms occupy open circles and group V atoms occupy solid circles.[1]

both the band gap and lattice parameter continuously. A compound $A_{(1-x)}B_xC$ will for example have a band gap which lies between that of the compounds AC and BC. If we wish to predict the band gap of this compound (assuming AC and BC are both direct band gap semiconductors) we can use for instance the fact that the band gap E_g is given by the equation

$$E_g(x) = E_g^{BC} + bx + cx^2 \qquad ..2.1$$

where b and c are constants, and the quantity E_g^{BC} is the band gap of BC. An alloy of appropriate composition can then be selected for a given device application. The variation of the band gap with composition for the case of $Ga_{1-x}In_x Sb$ is shown in Fig(2.2) [2]. In some compounds like $AlAs_xSb_{1-x}$ the band gap shows an almost linear variation with composition. In other semiconductor compounds, e.g., ternaries formed between GaAs and GaP, the band gap changes from being direct to indirect somewhere in the middle of the composition range. For application to luminescent devices it is important to know where this transition occurs.

Fig(2.3) [2] shows the band gap as well as the lattice parameter variation of the III-V alloy systems GaInAsP and GaAlAsSb. The ternary alloys discussed above lie on the lines joining individual binary compounds. The full lines indicate those compounds with a direct band gap and those with broken lines have an indirect band gap. The lattice parameters of these compounds vary roughly linearly with composition; this is referred to as Vegard's law [3,4]. The fabrication of a number of optoelectronic devices requires

growth of layers of a semiconducting material on a substrate. In such a situation it is necessary to match as closely as possible the lattice parameters of the overlayer with the substrate in order to avoid nucleating misfit dislocations at the substrate epilayer interface. These misfit dislocations may reduce the luminescence and for producing lasers or light emitting diodes need to be avoided. From Fig 2.3 it is quite clear that AlGaAs can be grown lattice matched to GaAs and hence this combination has been used to produce devices. When band gaps in the vicinity of 1.1-1.5 μm are desired it is necessary to look at quaternary compounds. For instance it is possible to obtain GaInAsP alloys which are lattice matched to both GaAs and InP. Fig(2.4) [1] shows those alloys which are lattice matched to InP. To the right of the line showing lattice matched compositions the layers are in tension and to the left the layers are in compression.

An interesting feature of III-V alloy growth is the fact that these alloys can both order during growth as well as decompose (phase separate). Thermodynamic arguments have been put forward to explain the suppression of decomposition in bulk alloys and its incidence in thin semiconductor layers. Early thermodynamic investigations of the (spinodal) decomposition process by Stringfellow et al. [5] seemed to indicate that bulk InGaAsP alloys were stable against phase separation. This conclusion was based on the observation that the calculated critical temperatures for the decomposition of bulk

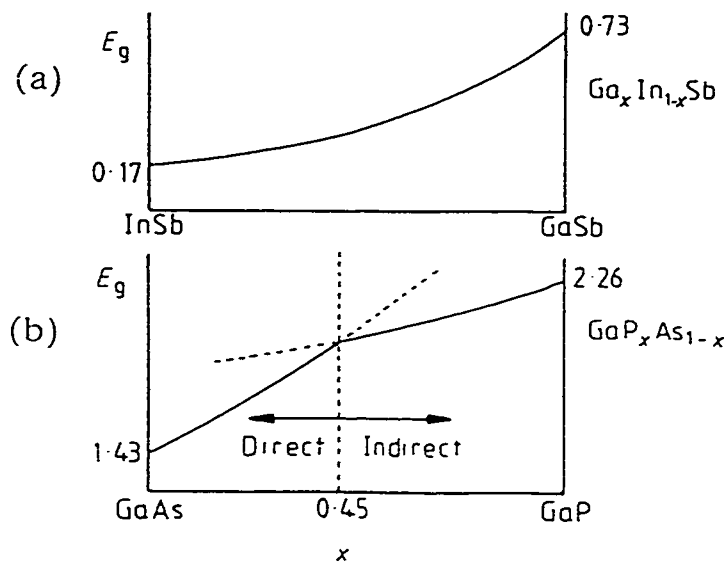

Fig 2.2 The variation of band gap with composition for (a) the $Ga_xIn_{1-x}Sb$ ternary system which has a direct band gap over the entire composition range; (b) GaP_xAs_{1-x} alloys in which a transition from a direct to an indirect band gap occurs at x =0.45. [2]

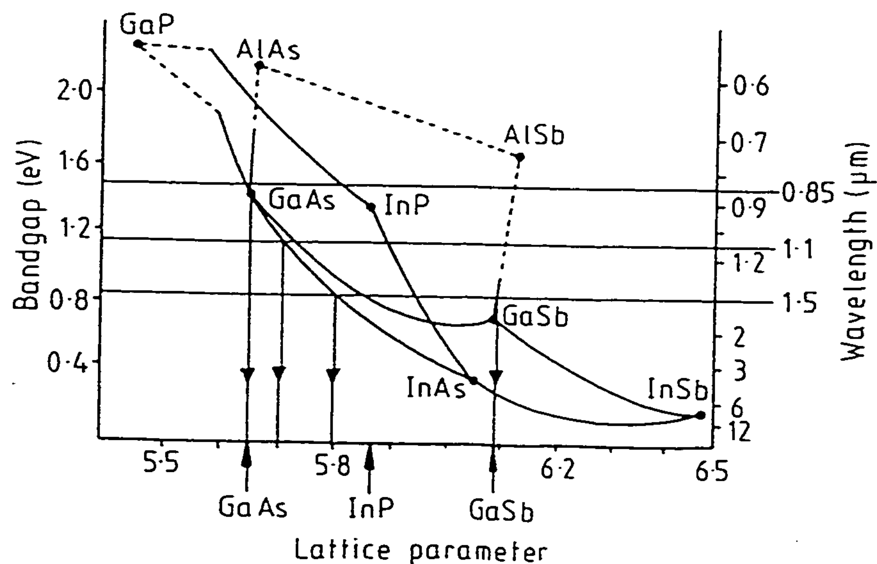

Fig 2.3 A sketch of the relationship between band gap and lattice parameter for the quaternary III-V systems GaInAsP and GaAlAsSb. [2]

$In_{1-x}Ga_xAs_yP_{1-y}$ alloys were below room temperature. However this calculation was found to be in conflict with experimentally observed phase separation in thin film $In_{1-x}Ga_xAs_yP_{1-y}$ alloys [6, 7] and $In_{1-x}Ga_xAs$ [8]. In consequence a modification of the theory was developed by Glas [9]. This analysis enabled a re-estimation of the strain energy stored by the film and showed that spinodal decomposition in $In_{1-x}Ga_xAs$ films could occur lower than about ~ 320K. However even this estimate is too low to account for the findings by Piero et al. [8] wherein composition modulations are reported for $In_{1-x}Ga_xAs$ films grown at ~ 515^0C. In $In_{1-x}Ga_xAs_yP_{1-y}$ alloys grown within the miscibility gap phase separation manifests itself in dark field T.E.M. [220] images as characteristic intensity modulations [1]. These correspond in $In_{1-x}Ga_xAs_yP_{1-y}$ alloys to regions enriched in InAs and GaP respectively. The presence of these composition modulations can also be inferred from PL measurements [10].

Strained semiconductor layers can also undergo ordering. In this phenomenon reported in GaAsSb [10] alternate $<111>_B$ planes become enriched in different group V constituents. A consistent model of this ordering was put forward by Philips et al. [11] by taking into consideration strain produced in an epilayer due to surface reconstruction. Group V stabilized surfaces near (001) are composed of large terraces and atomic steps of height equal to half the lattice parameter which compensates for the deviation of the surface from the singular orientation.

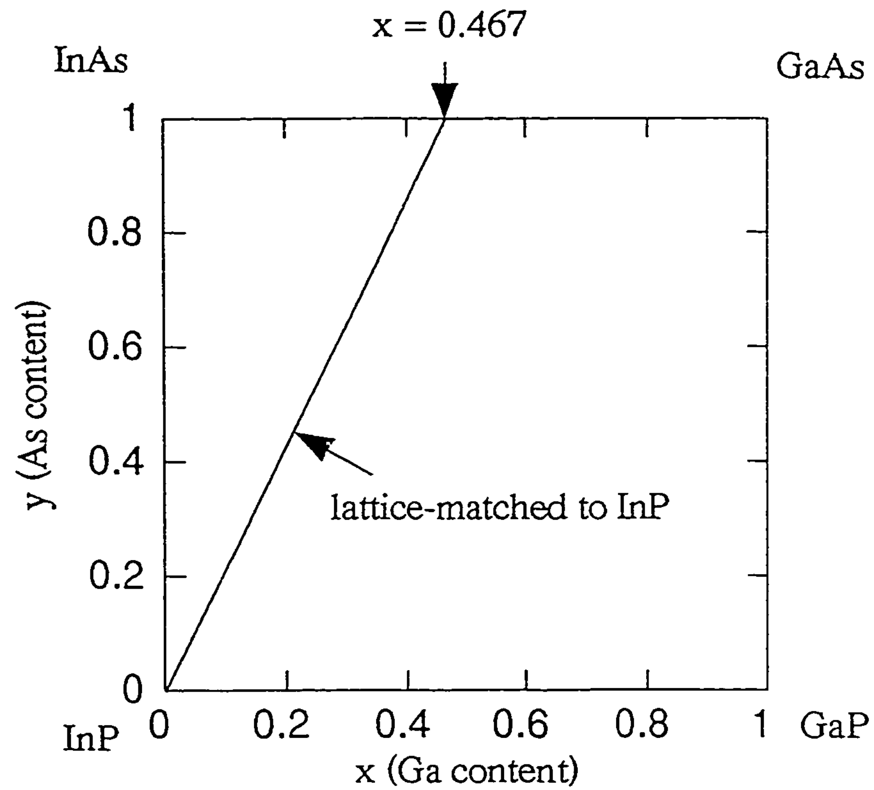

Fig 2.4 Composition diagram for $In_{1-x}Ga_xAs_yP_{1-y}$ alloy. The straight line represents the alloy compositions which have the same lattice constant as InP. (Lattice matched to InP). [1].

Depending on the direction of misorientation several different types of surface ordering can occur. The steps assume such a configuration that the group V atoms on the surface dimerize. The dimerization process results in sublayer strains with certain lattice sites suitable for the occupation of larger atoms and some others for the occupation of smaller atoms. This leads to the development of alternate rows of atomic planes which are respectively enriched and depleted in certain alloy constituents. Thus ordering is a growth-related strain driven effect.

A common feature in both the above phenomena is the role of elastic strains. In addition to its complicity in ordering and phase separation, strain can also drive a morphological instability of films away from a planar growth mode. Surface undulations which relieve strain energy in thin films have been widely reported [62] and theoretically modelled [12] following perturbative analysis of surface evolution equations. Perturbation analysis of the equations suggests that this evolution is linked to the surface energy, to the disregistry between the film and the substrate and the elastic moduli of the film and the substrate. Time scales for the evolution of the surface instability were also calculated from this perturbation analysis. It was shown that the morphological development would proceed more rapidly when the misfit strains were larger. A practical application of otherwise undesirable morphological evolution of thin films is in the recent upsurge of interest in three dimensional island growth which occurs in highly strained epitaxial layers, e.g. InAs grown on GaAs or SiGe films grown on Si. Concurrent

Concurrent research also proceeds on how to use these growth phenomena for the fabrication of laser devices. [13, 14, 15, 16].

2.1.2. Diffusion in GaAs based compound semiconductors.

In a compound semiconductor material like GaAs charged point defects are believed to be responsible both for Ga self diffusion and in AlGaAs for Al-Ga interdiffusion. Thermodynamic calculations have led to the conclusion that the point defect concentration in a GaAs crystal is dependent on the As partial pressure above the crystal [17]. Additional studies have also indicated that Ga self diffusion and Al-Ga interdiffusion are governed by a triply charged gallium vacancy V_{Ga}^{3-} [18, 19]. The diffusion of this complex defect results in high values for activation enthalpies and pre-exponential factors in the diffusion coefficient. Deppe et al. [20] estimate an activation enthalpy of ~ 4 eV for the V_{Ga}^{3-} mediated Ga self diffusion process. The identity of the point defect responsible for interdiffusion is also thought to be dependent on the doping of the crystal. It has been proposed that in intrinsic and n type crystals the governing defect is the triply charged Ga vacancy, while in p type crystals interstitial gallium I_{Ga}^{3+} is responsible for interdiffusion [21].

Experimental determinations of the Al-Ga interdiffusion coefficients have largely utilized X-Ray studies of superlattice structures (see section 2.2.2). By noting the

evolution of satellite peak intensities in AlAs-GaAs superlattice structures, Fleming et al. [22] estimate that in the vicinity of 850^0 C the Al-Ga interdiffusion coefficient $\sim 10^{-19}$ cm^2/s. Similar studies have also been made in the InGaAs/GaAs system by Joncour et al. [23]. These studies lead to an In-Ga interdiffusion coefficient of $\sim 10^{-18}$ cm^2/s at 850^0C. More recent studies have been concerned with the InGaAs/InP system. In this system interdiffusion operates on both the III lattice and the V lattice [24]. These studies reveal that the group V constituent diffuses faster than the group III constituent. The underlying defect types responsible for group V diffusion and group III diffusion are thought to be different [24]. The basic diffusion equations and the role of strain in the diffusion process are outlined in Appendix 1.

2.2 Quantum well structures.

Quantum well structures play a central role in the fabrication of several optoelectronic devices. These devices include semiconductor lasers, modulators and photodiodes. The restriction of electronic carrier motion in a direction normal to the film or layer may be viewed as carrier confinement in a one dimensional potential well. For films the well is considered to be an infinitely deep square well, whereas in the case of layers of semiconductors in a heterostructure the wells are of finite depth and very nearly rectangular in profile.

2.2.1 Particle in a one dimensional potential well.

The particle in a one dimensional potential well is one of the most elementary problems in quantum mechanics [25]. For the case where the well is infinitely deep the Schrödinger equation can be solved to yield the eigenvalues of energy which are listed in Fig (2.5), [26]. The particle motion is quantized giving rise to a series of discrete bound states in the well. For very large values of L_z a continuum of states results and the system is no longer in the quantum limit. In general however the well is not infinitely deep. This simply means that the particles may penetrate into the barrier and the boundary conditions have to be changed to reflect this possibility. The problem then resolves into two parts, i.e. to find solutions in the well and in the barrier region. The solutions for the well region are listed in Fig (2.5). In solving the wave equation it is assumed that the potential is 0 in the well and V_o in the barrier region. The solutions in the two regions however have to satisfy continuity of the wavefunction and its first derivative (scaled with the inverse of the effective mass m^*) at each interface. It is appropriate at this point to remark that the energy levels are dependent on the geometric dimensions of the well and would change as the dimension L_z changes. This is the quantum size effect (QSE). It is also interesting to note that the minimum energy of the confined carrier is not equal to zero. This is a consequence of the uncertainty principle. The wave function solutions in the wells themselves are sinusoidal while in the barriers they are exponentially decaying functions. If the dimension $L_z << L_x, L_y$ the energy levels in the k_x, k_y directions are very closely spaced and for each value of E_n a two dimensional energy band in the k_{xy} plane will form. It can be shown that the band density

of states is independent of energy so that the cumulative density of states for a series of bands will show a step wise character, Fig(2.6(a)) [26]. This is the model that applies to a thin film. It is clear that as a result of the quantization of particle motion normal to the film, discrete bound states will emerge and the energy of the lowest state will increase as the thickness of the film decreases.

2.2.2. Tunnelling and one dimensional potential wells.

Tunnelling in a multibarrier structure consisting of rectangular barriers and wells of III -V semiconductors has been discussed by Tsu and Esaki [27]. When the barrier separating two quantum wells is reduced in extent it is possible that the decaying tail of the wavefunction in the barrier has a non zero value in the adjoining well Fig(2.6(b)) [61]. This sets up a situation in which there is a finite probability of finding the electron in the second well; in this case the electron is said to have tunnelled into the second well. The energy levels in the coupled wells can be computed [61] and calculations show that the initially degenerate levels in the isolated wells split into a symmetric and antisymmetric combination. As the number of coupled wells increases the energy level splitting also increases. In the limit of a large number of coupled wells a band like condition analogous to a Kronig Penney one dimensional crystal, is ultimately reached [28]. This coupled quantum well structure is referred to as a superlattice. The central feature of a superlattice is the nature of the density of states.

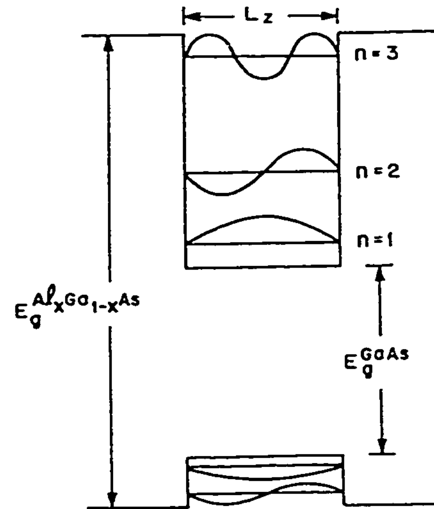

$$-\left(\frac{\hbar^2}{2m}\right) d^2\,\psi/dz^2 = E\psi$$

$$E_n = \frac{\hbar^2}{2m}\left(\frac{n\pi}{L_z}\right)^2$$

$$n = 1, 2, 3, \ldots$$

Fig 2.5 The Schroedinger equation, it's eigen values and eigen functions for an infinitely deep potential well. As shown, the two wells are of finite depth and apply to the electrons and holes in the GaAs layer of an $Al_{1-x}Ga_xAs$/GaAs heterostructure. [26]

$$\psi_n = A \sin \frac{n\pi z}{L_z}.$$

$$E = E_n + \frac{\hbar^2}{2m}\left(k_x^2 + k_y^2\right)$$

$$E_n = \frac{\hbar^2}{2m}\left(\frac{n\pi}{L_z}\right)^2$$

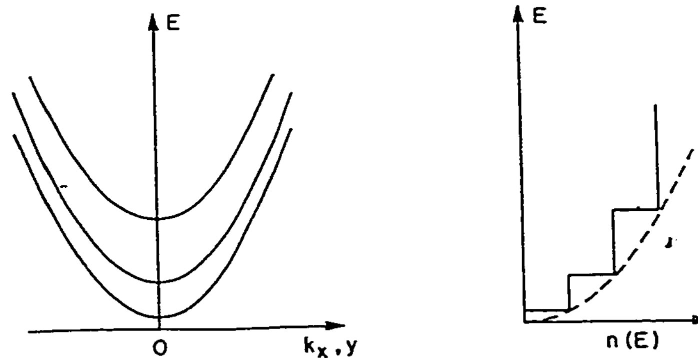

Fig 2.6(a) Schematic representation of a parabolic energy band in the quantum limit. Two dimensional bands in the $k_{x\text{-}y}$ plane give rise to a stepped cumulative density of states with increasing energy. [26].

The cumulative density of states no longer shows a step wise character as in the isolated well. The superlattice impresses on the structure a periodic potential that is considerably larger than atomic dimensions and as a result the original Brillouin Zone is reduced into a series of minizones and gaps in the E-k dispersion in the superlattice direction [29].

2.2.3 Absorption spectra of single quantum well structures and superlattices.

Absorption studies provide valuable information about the energy levels of the quantum wells and superlattices. Absorption, unlike spontaneous emission, is also capable of providing information about higher energy levels (n>1). Consequently early fundamental studies were performed on quantum well structures to explore the effects of confinement on absorption wavelengths [30].

Optical absorption of a beam normal to the layers of a superlattice AlGaAs /GaAs structure has been investigated [30], Fig (2.7). In this case the GaAs layers varied in thickness from 40 $\mathring{A}$ to 500 $\mathring{A}$ and were separated by barriers of AlGaAs thick enough to ensure that the carriers were confined to the GaAs layer. In order to obtain sufficient absorption from the structure, samples containing up to 100 layers were grown, while to ensure that any absorption effects arose only from the layers the substrate and the buffer layers were removed. Any absorption effects below the band gap of AlGaAs can be attributed to the energy states from the GaAs potential wells.

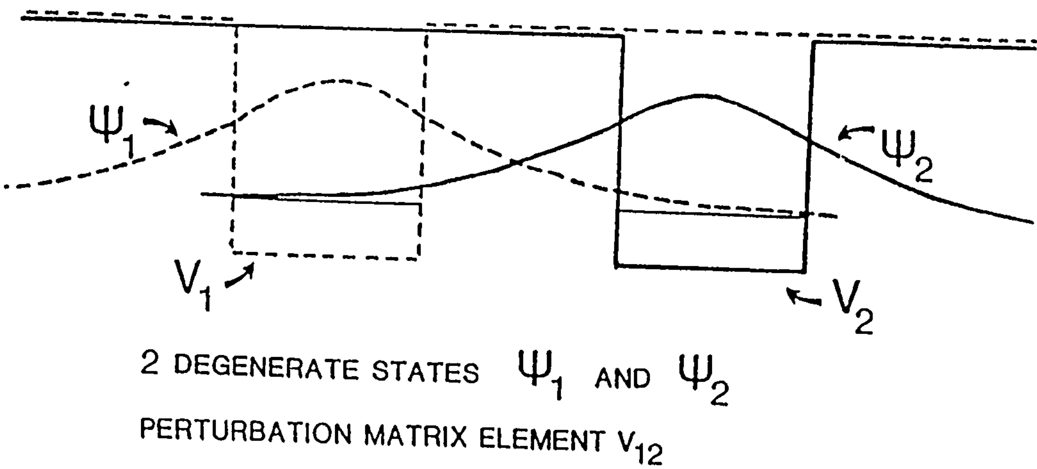

Fig 2.6(b) Tunnel coupling between two wells. [61].

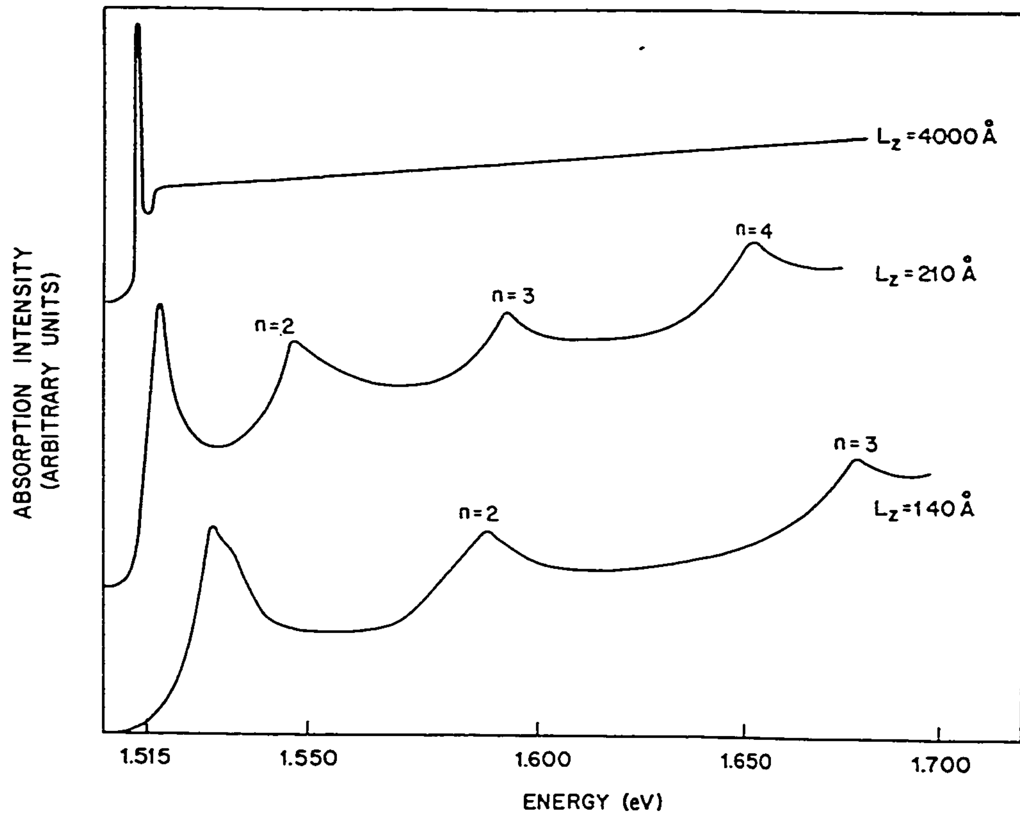

Fig 2.7 Absorption spectra (2K) of 4000, 210, 140 Å thick GaAs layers between $Al_{0.2}Ga_{0.8}As$ barriers. The quantum size effect manifests itself as an increase in the bulk exciton energy and by the appearance of higher energy peaks in the the thinner layers. [26].

The direct band gap of GaAs is 1.52 eV at 2K and corresponds to the transition from the k=0 edge of the valence band to the k=0 edge of the conduction band. Coulombic attraction between the electron in the conduction band and the hole left in the valence band results in the formation of an exciton which has a binding energy of 4.2 meV. This exciton makes a dominant contribution to the band edge absorption spectrum. For $L_z >$ 500 $\overset{0}{A}$ the multilayer spectra were essentially indistinguishable from the bulk spectrum. However below 500 $\overset{0}{A}$ dramatic changes occured in the spectrum. They are associated with the quantum size effect. After a slight shift to lower energy, the bulk exciton moves to higher energy as the thickness decreases. The rate of change varies roughly as the inverse square of L_z. In addition new absorption peaks developed in the previously smooth absorption spectrum above the band edge and the whole spectrum took on a stepwise character with a peak preceding each step. A qualitative understanding of these phenomena can be achieved with the admission of excitonic effects and the stepwise density of states alluded to earlier. On closer scrutiny, especially as the layers get thinner, other features emerge. The lowest excitonic peak shows a small splitting. A complete understanding of this can be achieved by applying the QSE to both the conduction band and the valence band. This results in the splitting of the originally degenerate valence band into $J,m_j\rangle$= 3/2, 3/2 $\rangle$, 3/2, 1/2 $\rangle$ values with effective masses which are given by $m(\gamma^{-}_{1} - 2\gamma_2)^{-1}$ and $m(\gamma^{-}_{1} + 2\gamma_2)^{-1.}$ These are respectively referred to as heavy hole and light hole masses. The selection rule governing the transitions in the

quantum well is $\Delta n=0$ where n refers to the excitation state, Fig(2.8).

The coupling of quantum well structures to produce superlattices also leads to changes in the absorption spectrum. The coupling of wells (as has been discussed earlier) leads to the development of symmetric and antisymmetric energy levels. A further optical selection rule is observed: that is transitions only between symmetric levels or antisymmetric levels are allowed. The spectrum from a double well structure is shown in the inset in Fig (2.9). The calculated transition energies using electron and hole energies from a coupled well barrier transmission calculation and adjusted for excitonic effects are also included in the inset. The effect of the additional selection rule is to limit to four the number of possible transitions.

2.2.4 Devices constructed with quantum well superlattices.

A number of devices have been fabricated based on the confinement properties of quantum wells. The multilayer superlattice structure embodies two principal requirements of double heterostructure laser devices, namely carrier confinement by the quantum well and photon confinement by the intervening barrier layers. Optically pumped laser action has been demonstrated in these structures. The laser action is associated with the n=1 quantum state. One of the earliest studies in this area is that due to Van der Ziel et al. [31]. More recent work with GaN has resulted in blue laser

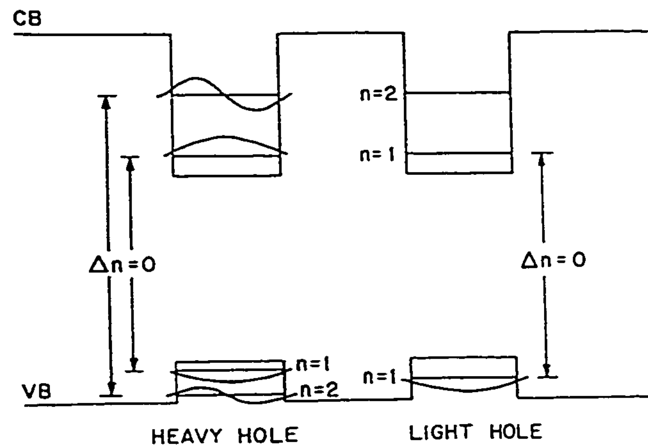

Fig 2.8 Bound states and wave functions of quantized valence and conduction bands demonstrating the Δn=0 selection rule for interband transitions. [26].

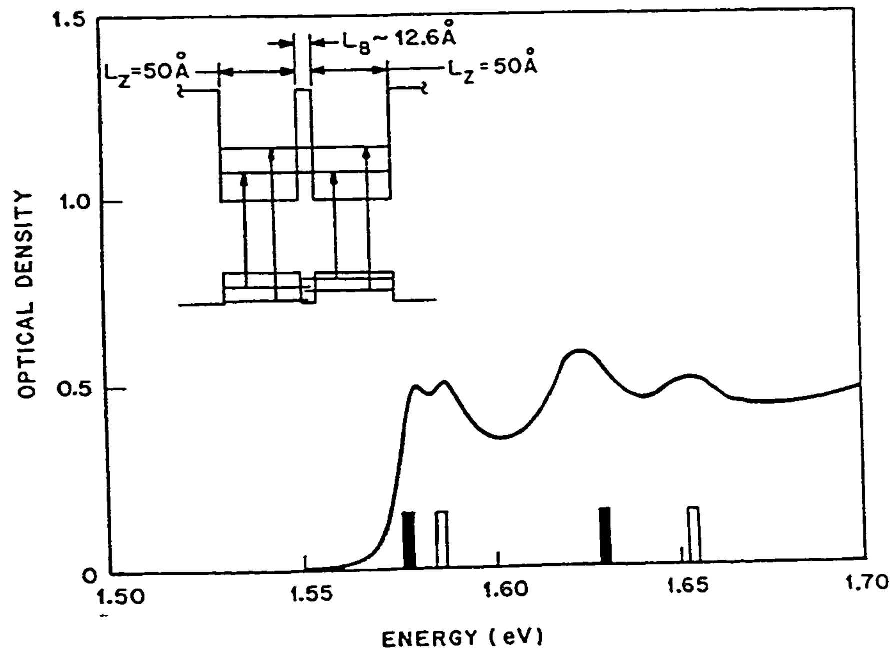

Fig 2.9 Absorption spectrum (2K) of a series of double -well AlGaAs /GaAs structures. The inset is a schematic energy level scheme for a pair of coupled wells. A coupled -well selection rule (see text) limits to four the number of allowed transitions between the six discrete energy levels of the coupled wells. Calculated transition energies are included. [26].

diodes [32]. The electron and hole wave functions are dependent on the applied bias across the superlattice structure and the absorption peaks show a marked red shift as the applied bias across the structure is increased. This effect is called the quantum confined Stark effect and has been utilized for the construction of modulators. Additionally, infrared radiation can excite conduction band electrons to higher energy levels from which they can effectively be pulled out of the well through an applied bias. This manifests itself as an infrared radiation enhanced conductivity and is the principle of the quantum well infrared photodiode, which can be used for the construction of infrared cameras. The infrared photoconductivity and electro-optic effect has been used in conjunction to construct an interesting device called S.E.E.D. (self electro-optic effect device). In this device the infrared radiation excites a current which causes a voltage drop across a resistor connected across the device. This changes the transmissivity of the device through the Stark effect. S.E.E.D. devices coupled with heterojunction bipolar transistors can be used as photonic switches [33].

2.3 Photoluminescence

While the preceding section discussed in some detail the transitions that are responsible for absorption in quantum well structures, of central concern to this study is spontaneous emission from semiconductors. Consequently we discuss briefly the transitions which

can give rise to luminescence from semiconductors.

The possible transitions are listed in Fig (2.10). The first of them corresponds to the decay of a free exciton at low temperature. This is the situation in the case of a pure semiconductor. Excitons can be of two types [34]:

1. Localized or Frenkel excitons.
2. Wannier Mott excitons which loosely resemble a hydrogen atom in that an electron revolves around a hole and both of them are mobile in the crystal lattice. The energy levels that the electron can occupy can be obtained by analogy with the levels of the electron in the hydrogen atom and are given by :

$$E_x = (13.6)\,(m^*_r/m_o)\,(1/\varepsilon_r^2)(1/n^2) \quad \text{(eV)} \qquad ..2.2$$

where

$$1/m^*_r = 1/m^*_e + 1/m^*_h \qquad ..2.3$$

is the reduced mass and the quantities m^*_e , m^*_h are the electron and hole effective masses respectively. ε_r is the relative di-electric constant. The free exciton energy levels lie close to the bottom of the conduction band in the forbidden energy gap. In materials with indirect energy gaps the free exciton is accompanied by the formation of a phonon in order to conserve crystal lattice momentum. This results in the free exciton peak developing a number of phonon replicas at energies given by

$$E_{pl} = E_g - E_x - nE_p \qquad ..2.4$$

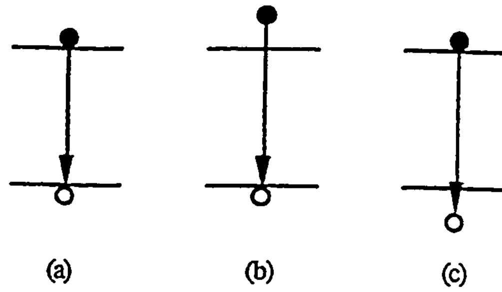

Fig 2.10 (a) Energy level diagrams showing free carrier recombination with carrier close to the band edges of the material (a), electron-hole recombination with excited electron (b) and excited hole (c). [10].

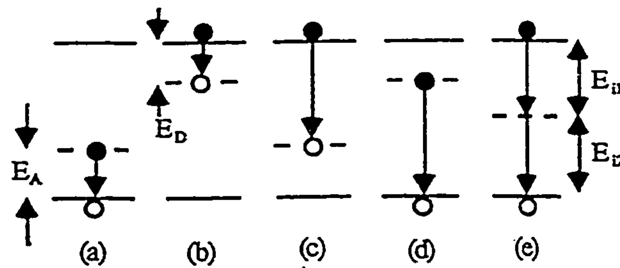

Fig 2.10(b) Shallow transitions shown are (a) acceptor to valence band transition, (b) conduction band to donor transition. Deep transitions are (c) conduction band to acceptor transition and (d) donor to valence band transition. (e) shows a deep level transition. [10].

where the quantities E_g, E_x, E_p are the band gap, exciton binding energy and the phonon energies respectively.

In the case of a doped semiconductor the excitons can be bound to either a donor or an acceptor and the corresponding peak is reduced in energy as compared to the free exciton peak. The energy levels in this case are given by:

$$E = E_g - E_x - nE_p - E_b \qquad ..2.5$$

where the quantity E_b is the binding energy of the exciton to the donor or acceptor atom. The energy of the bound exciton lines are dependent on the nature of the dopant and hence the lines can be used to determine the presence of certain elements like boron or aluminium in silicon. In addition calibration curves for these elements can be obtained by comparison of the peak heights of the no phonon bound exciton peak with the phonon assisted free exciton peak and can be used for the determination of elemental concentrations ~ $10^{17}/cm^3$ [35].

Other possible transitions include those between bands and impurity states. The transition between the conduction band and donor level or that between the acceptor and valence level are luminescent in the far infrared region. Transitions between the donor

and valence levels, conduction and acceptor levels are possible. The donor acceptor transitions give useful information about donor concentrations, as the peak intensity depends on the donor concentration levels. Time resolved PL can be conducted as well and information regarding radiative life times can be obtained. Additionally polarization resolved photoluminescence can be used to extract information of stresses in laser diodes [36].

In quantum well samples luminescence involves the recombination of bi-dimensional excitons. Selection rules that were discussed for absorption in quantum well structures (section 2.2.3) also operate for the case of luminescence. Since the confinement energy of the carriers depends on the dimensions and composition of the quantum well, photoluminescence can be used to follow the compositional evolution during interdiffusion of superlattice structures. This technique has been utilized in this study.

Typically luminescence is excited by irradiating the sample with a laser beam with photon energy greater than the band gap energy. When a laser beam illuminates the semiconductor sample, electrons and holes are created. These charge carriers can recombine radiatively or non radiatively. They can also diffuse into the material or recombine at the surface. The low energy photons created by radiative recombination may be reabsorbed by the material or emitted from the surface. There is also the

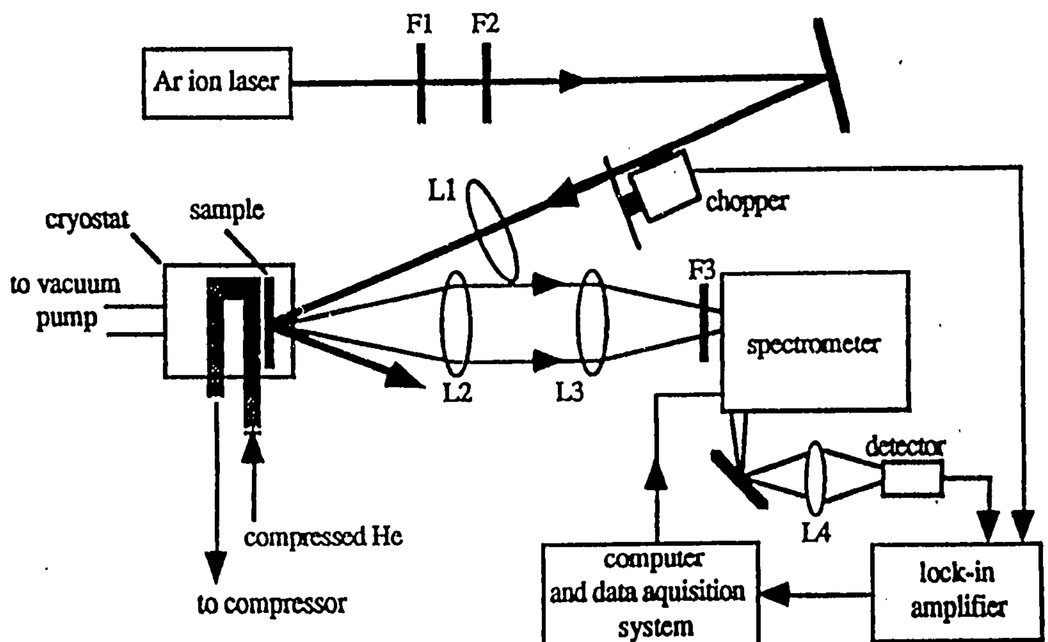

Fig 2.11 PL system at McMaster University. (For the experiments reported in this thesis a Helium Neon laser was used.)

possibility that the photons directed at the back surface might be reflected back to the front and included in the emission. All these processes determine the luminescent output [37]. A schematic diagram of the experimental setup used for photoluminescence studies in this thesis is shown in Fig(2.11).

2.4 Ion implantation enhanced quantum well interdiffusion.

The primary requirement for the integration of optoelectronic devices is the mutual compatibility of the band gap energies among various devices. Consider the example of a laser coupled to a modulator and waveguide. In such a device it is necessary for the band gap of the laser to be lower than that of the modulator which in turn has to be lower than that of the wave guide. This would conventionally involve complicated etch and regrowth processes which are possible in principle but difficult in practice. A technique which has started to generate considerable interest is the selective interdiffusion of quantum well structures. Selective interdiffusion or quantum well disordering, offers a planar technology which can be used to laterally integrate regions of different band gaps within the same epitaxial layer. By intermixing the quantum well and the barrier material, the absorption, emission and the refractive properties can be altered in a controlled manner through the resulting change of band gap energies. Although various methods have been reported for this disordering we shall concentrate on ion implantation enhanced interdiffusion.

2.4.1 Theory of disordering.

As energetic ions enter an attenuating medium they lose energy through two principal processes. The atoms, which were initially at rest are displaced from their equilibrium positions resulting in loss of energy of the incoming beam. Additionally ions lose energy to the electron cloud.

There is a well developed theory to account for the loss of energy due to both of the above mentioned processes. The numerical results, based on 50 years of work in this area, have been summarized in a paper by Biersack at al. [38]. This work also lays out the essential formulae used for simulating the ion trajectories in amorphous targets. This is the basis of the Monte Carlo program TRIM (TRansport of Ions in Matter). The same theory is discussed at length in the monograph of Ziegler et al. [39]. The incoming energetic ions interact with the nuclei in the target material as a result of the existence of a Coulombic potential and are scattered. This results in the ion performing a random walk on a hypothetical diffusion sphere. Between nuclear scattering events the ion interacts with the electron cloud initiating more scattering events and hence more loss in energy. The model basically develops formulas for the energy loss and deflection angles following nuclear scattering events and energy loss to the electron cloud during the time of flight between nuclear scattering events.

Nuclear scattering is treated in a centre of mass co-ordinate system Fig (2.12),

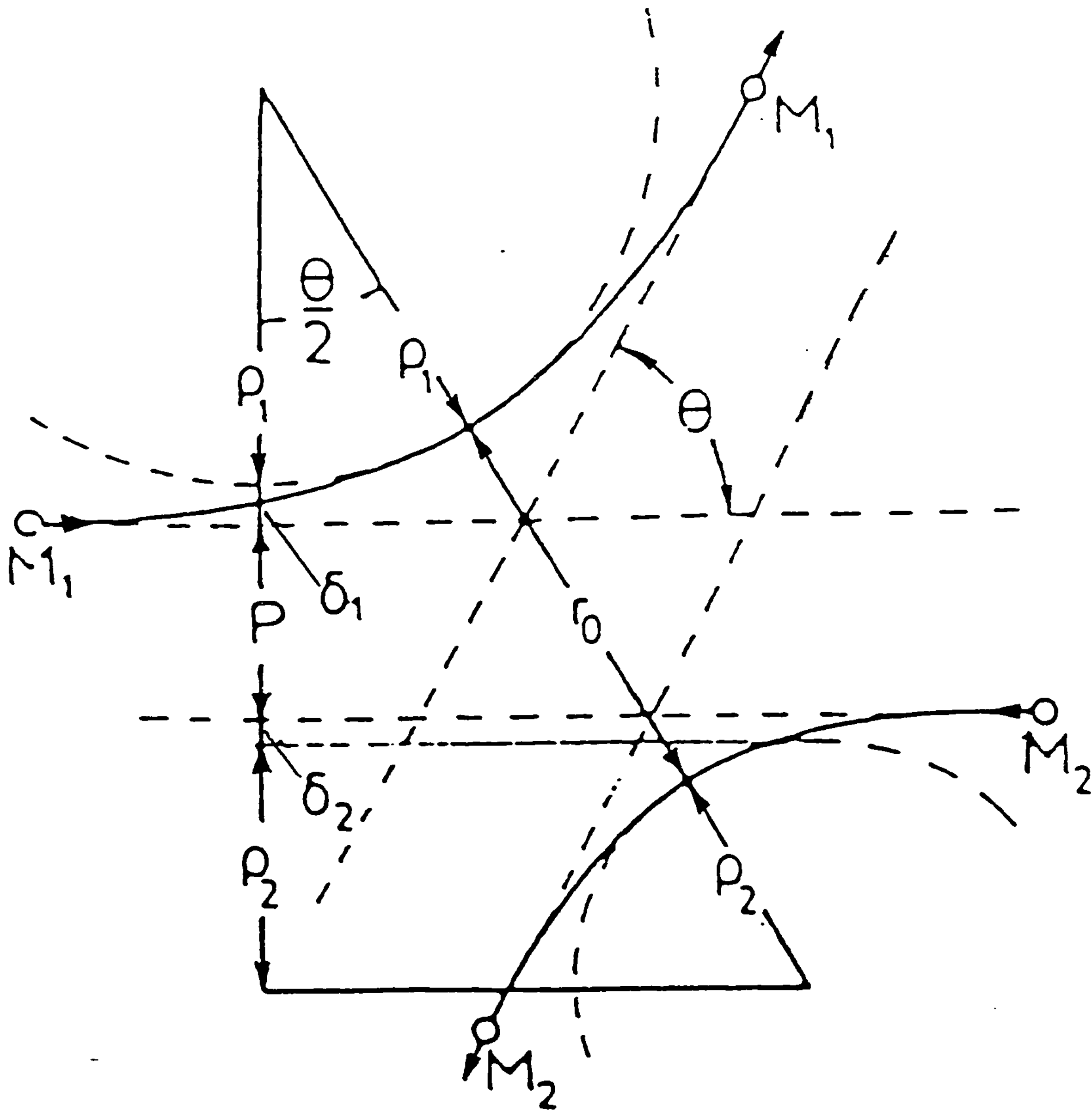

Fig 2.12 Particle trajectories in the center of mass system, with the superimposed "scattering triangle," comprising the impact parameter P, distance of closest approach r_0, radii of curvature ρ_1 and ρ_2 (curvature of trajectories at closest approach) and correction terms δ_1 and δ_2. From this construction the scattering angle θ can be obtained. [39].

[39]. The incident particle of mass M1 and kinetic energy E is scattered by a particle of mass M2 which is initially stationary. There exists a potential V(r) between the particles. This potential has nuclear-nuclear, electron-nuclear and electron -electron contributions. Ziegler et al. [39] develop an universal screening function for calculating the interaction potential between any ion and target atom. A knowledge of this screening function enables a computation of the deflection angle θ of the ion due to Coulombic interaction.

Calculation of the deflection angle θ of the ion from first principles dynamics of a charged particle in a central potential is a computationally expensive procedure. Consequently efforts have been expended to obtain a simple formulation for the scattering angle. These generally go by the descriptive name of magic formulae. One such procedure is elaborated by Ziegler et al. [39] and is shown in Fig(2.12). The scattering angle θ (which is the most important parameter as far as energy loss is concerned) can be easily derived from this figure as equal to

$$\cos(\theta /2) = \rho+P+\delta /\rho+r_o \qquad ..2.6$$

where $\rho = \rho_1 + \rho_2$ (radii of curvature of particle trajectories)

$\delta = \delta_1 + \delta_2$ (are small correction terms defined in Fig 2.12) ..2.7

P is the impact parameter.

The closest distance of approach r_o can be obtained from the expression

$$1 - V(r_o)/E_c - (P/r_o)^2 = 0 \quad ..2.8$$

E_c is the amount of energy present in the centre of mass co-ordinate system given by

$$E/(1 + M1/M2) \quad ..2.9$$

The nuclear energy loss or energy transfer T to the target atom in a single collision is proportional to $\sin^2(\theta/2)$ and is given by

$$T = 4\, M1\, M2\, E \sin^2(\theta/2) / (M1 + M2)^2 \quad ..2.10$$

This angle θ in the centre of mass co-ordinate system can be converted back to the laboratory co-ordinate system using the conversion formula

$$\Psi = \tan^{-1}[\sin(\theta)/(\cos(\theta) + M1/M2)] \quad ..2.11$$

where the angle Ψ is the laboratory angle of scattering. The azimuthal angle φ is randomly selected from the range [0 to 2π]. A recursive relation which connects the angles of scattering between successive collisions can then be used to follow the trajectory of the ions as it loses energy to the target particles. It then remains to specify the impact parameter P. This is once again a randomly generated quantity with a functional relation which depends on both the target atomic density and mean free path of ions between nuclear collisional events. During each of these free flight paths the ions interact with the target electron cloud and lose energy. The equations which relate the loss of energy of the ion to the target electron cloud have been developed in two different energy regimes of the ions. The basic form of these equations is given by

$$\delta E_e = L\, N\, S_e \qquad ..2.12$$

where L is the mean free path between nuclear collisional events.

S_e is the electronic stopping cross section.

N is the atomic density of the target.

The electronic stopping cross section is given in the low energy range by the formula due to Lindhard [40] and in the high energy range by the formula due to Bethe and Bloch. [38]. In the intermediate ion energy range, the scattering cross section is obtained by summing the reciprocal of the cross sections in the low energy range and the high energy range.

The Lindhard cross section is dependent on the velocity of the ion and is given by

$$S_L = k_L\, E^{1/2} \qquad ..2.13$$

The quantity k_L is a function of the atomic numbers of the colliding particles (Z) and the mass of the incident particle (M_1), but is velocity independent. It is given by

$$k_L = 1.2\ Z_1^{7/6} Z_2 M_1^{-1/2} / (Z_1^{2/3} + Z_2^{2/3})^{3/2} \qquad ..2.14$$

This theory can then be used to predict the range of ions in solids.

In the high velocity regime scaling rules have been developed to predict electronic stopping on the basis of an exact theory for the penetration of protons into solids. [39].

Scaling refers to a principle whereby the theoretically computed electronic stopping of protons in a solid (S_H) can be used to predict the stopping of a heavy ion (S_{HI}) simply by using the formula

$$S_{HI} = S_H (Z^{*}_{HI})^2 = S_H(Z^2_{HI})(\gamma^2) \qquad ..2.15$$

The quantity γ determines the effective charge of a heavy ion penetrating a solid and depends on the velocity of the ion. Brant and Kitagawa [41] have developed the theory of velocity dependent charge which enables a calculation of the electronic stopping through use of scaling concepts.

With that brief look at stopping theory let us next consider the production of vacancies by an ion penetrating a solid. This is of course of central concern as it determines the diffusional enhancement available following ion implantation. Vacancy production in TRIM is calculated on the basis of a model due to Kinchin et al. [87]. In the Kinchin-Pease model [87] the vacancy production is related to the nuclear component of the energy lost by an ion penetrating the solid T, equation (2.10). In this model the number of vacancies produced by an ion is obtained by dividing the defect production energy E_v (which is related to T, the nuclear deposited energy corrected for electronic losses) by $2E_d$. E_d is the energy required to knock an atom out of its site in the solid. Typically vacancy production depends not only on the energy of the ion but also on the implant temperature (a feature which we will see in the section on experimental results.)

In summary then nuclear scattering results in collisional mixing of the implanted material. This purely ballistic component is dominant at high beam energies. At lower ion energies the vacancies and the interstitials which are left in the wake of the beam can contribute to intermixing by enhancement of diffusion. This isssue is considered in the next section.

2.4.2 Implantation studies

The central idea behind the use of quantum well interdiffusion is the enhancement of the interdiffusion coefficient by the defects introduced by ion implantation. In order to illustrate the general nature of implant enhanced interdiffusion studies, two specific studies of ion implantation induced disordering reported in the literature will be considered. The first study, conducted by Allard et al. [42], involves low energy 100 keV implantation of Ga^+ ions into the structure shown in Fig(2.13). The dose was 10^{+13} ions /cm^2. The implanted structure was subsequently subjected to rapid thermal annealing at 850^{0}C for 60 seconds. During implantation the beam was normal to the wafer and this enabled channelling of the beam to the lowest quantum well in the structure located 450 nm from the top of the structure. The photoluminescence peaks from the four quantum wells showed a blue shift following implantation and annealing Fig(2.14). The blue shifts were of the order of 20 meV. The amount of the blue shift depended on the composition of the $In_xGa_{1-x}As$ quantum wells which in this case increased from 10% In at

the top well to 25% at the lowest well [42].

A second study by Charbonneau et al. [43] involves the high energy implantation of As^+ beams at energies ranging from 2 -8 MeV into the structure shown in Fig(2.15). This structure was once again a laser structure but had a graded AlGaAs region which helped in confinement of the optical mode of the laser and hence the device has a lower threshold current density. The energy of the beam was sufficient to cause disordering at depths of 2 μm, which roughly corresponds to the location of the $In_{0.23}Ga_{0.77}As$ quantum wells. Subsequent to the implantation the structure was rapid thermally annealed at 850^0C for 90 seconds, and characterized by both photoluminescence and cross sectional T.E.M. Fig(2.16) shows the photoluminescent peak blue shifted following the treatment. This study also confirmed that annealing of the original structure did not cause any blue shifting of the peaks at temperatures lower than 850°C. Photoluminescent characterization of the as implanted structure did not exhibit any blue shifting either. Blue shifting is thus a consequence of both the implantation and annealing. The blue shifted peak in Fig(2.16) had an integrated intensity which was 1/3 of the intensity of the original peak and was also considerably broadened as compared to the original peak [43]. The loss of photoluminescent intensity is a consequence of the defects created following implantation which are sites of non radiant recombination.

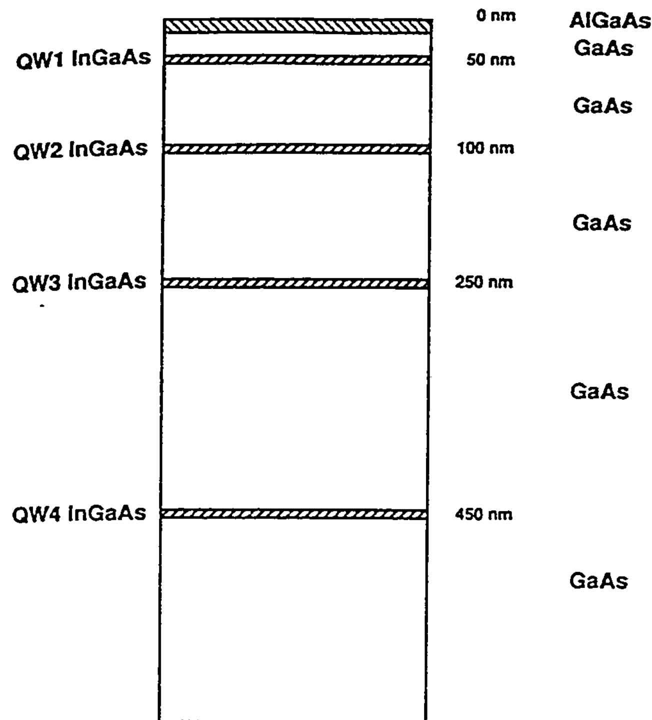

Fig 2.13 Schematic diagram showing the cross section of the quantum well structures used in [42]. The quantum wells are InGaAs and contain 10%,15%,20% and 25% indium respectively.

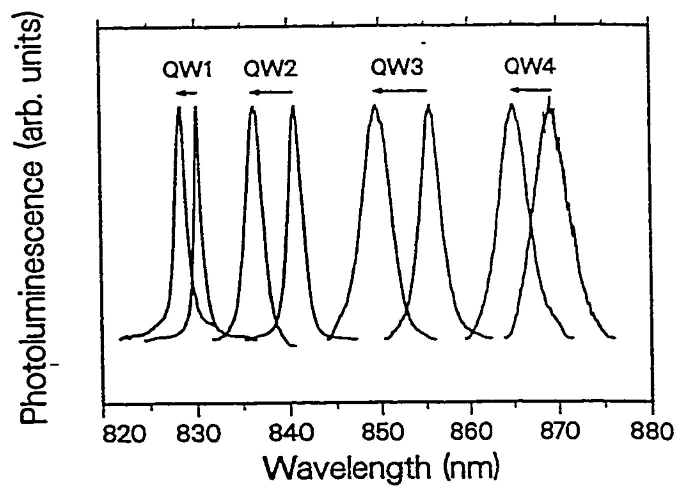

Fig 2.14 Low temperature (4K) PL spectrum of sample shown in Fig 2.13, before and after broad area ion implantation with $0.6*10^{13}$ ion/cm^2 Ga and annealing at 850^0 C for 60 seconds.

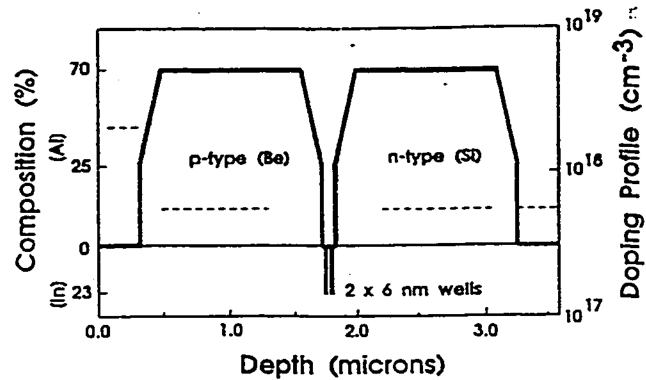

Fig 2.15 Schematic diagram of the structure used for experiments in [43].

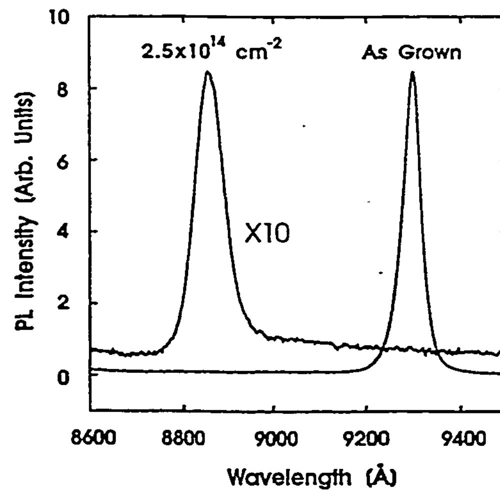

Fig 2.16 Low temperature PL spectra of the as grown and implanted (As^+ 8 MeV, $2.5*10^{14}$ ion/cm^2) $In_{0.23}Ga_{0.77}As$ laser structure after annealing. Annealing was conducted at 850^0 C for 90 seconds. [43].

The broadening of the PL peak following implantation and annealing has been attributed [43] both to the variation in quantum well thickness across the sample and the variation in the indium concentration across the well. The PL peak intensity recovers dramatically following annealing as a consequence of the elimination of these non radiant recombination centres. These conclusions have been supported by TRIM simulations which predict the range of ions in materials.

TRIM simulations conducted with AlGaAs/GaAs quantum well structures corroborate the finding that the maximum attenuation in PL intensity occurs when the peak of the ion distribution coincides with the quantum well. The maximum blue shift occurs when the peak of the vacancy distribution coincides with the quantum well [44].

However major differences were reported in the case of InGaAs/InGaAsP/InP multilayers. In these structures the extent of PL peak blue shifting did not show the same correlation with the TRIM profiles as in the case of AlGaAs/GaAs structures [45]. Rather the amount of blue shifting of the PL peak showed only a correlation with the total amount of vacancy creation in the sample. Poole et al. [45] have rationalized this difference in the two cases in terms of the differences in the vacancy diffusion rates in the two structures. The preponderance of local vacancy concentration in determining blue shifting in the case of AlGaAs /GaAs was attributed to the low rates of vacancy diffusion on the group III lattice of this structure. The results in the case of InGaAs/InP were

attributed to the fast rates of vacancy diffusion on the group V lattice. In the case of the InGaAs/InP additional studies [46] have indicated that the extent of interdiffusion is also governed by the indium content of the wells. Larger indium contents lead to greater blue shifts.

The extent of blue shifting of the peak also depends on the implantation and thermal anneal schedules. Generally there is a maximum vacancy concentration and hence a maximum achievable energy shift that can be delivered to the crystal during one implant cycle. Beyond this threshold, vacancies begin to group themselves into defect clusters that do not diffuse during the subsequent rapid thermal anneal [47]. This situation can generally be improved by multiple implant anneal techniques. The first thermal anneal restores sample crystallinity and frees many of the defects acquired during the implantation process. This allows the following implantation process to create more vacancies without immediately adding to the undesirable growth of defect complexes. Experiments conducted on AlGaAs/GaAs structures by Piva et al. [48] have shown that a blue shift of as much as 30 meV can be achieved after 4 implants and 5 anneals as compared to less than 5 meV for one implant anneal cycle. Finally we need to describe the origin of the blue shift itself. The theory behind the origin of the blue shift is elucidated in [42]. This study was conducted on InGaAs quantum wells with GaAs barriers. Vacancy assisted disordering of the quantum well interfaces changes the light and heavy hole - electron band gap.

The heavy hole - electron band gap is given by the equation

$$E^{hh}{}_{h} = E_g{}^{0} + \delta E_h - \delta E_s \qquad ..2.16$$

In the above equation E_g^0 is the unstrained band gap and is dependent on the In content x. It is given by

$$E_g{}^{0} = 1519.2 - 1594x + 485x^2 \ \ (\text{meV}) \qquad ..2.17$$

The other terms δE_h and δE_s in equation (2.16) refer to the hydrostatic pressure shift and stress induced valence band shift respectively. These are given by

$$\delta E_h = 2a[(C_{11} - C_{12})/C_{11})]\varepsilon \qquad ..2.18$$

$$\delta E_s = b[(C_{11} + 2C_{12}/C_{11})]\varepsilon \qquad ..2.19$$

In the above expressions a, b are the interband hydrostatic pressure and uniaxial deformation potentials respectively. The constants C_{ij} are the elastic constants of the InGaAs well material and ε refers to the misfit strain between the InGaAs well and the GaAs barrier. The effective masses for the heavy and light holes (in terms of the Luttinger parameters γ) and electrons (as a fraction of the free electron mass) are given by

$$m_e = 0.067 - 0.044x$$

$$m_{hh} = (\gamma_1 - 2\gamma_2)^{-1}$$

$$m_{lh} = (\gamma_1 + 2\gamma_2)^{-1} \qquad ..2.20$$

Interdiffused concentration profiles as developed in a simple model by Cibert et al. [49]

can be used to compute the variation of indium across the well. The indium concentration is given by

$$x_i\,(y) = x(\,1 - 1/2\mathrm{erf}((1/2w - y)/2\Delta_i\,) - 1/2\;\mathrm{erf}((1/2w + y)\,/2\Delta_i\,) \quad ..2.21$$

The quantities w and y are listed in Fig(2.17). The parameter Δ_i is defined such that $4\Delta_i$ is the distance over which the indium concentration drops from 90% to 10% of its initial value.

The transition energy (heavy hole electron transition) can hence be computed as

$$E^{tr} = E_1^{hh} + E_1^{e} + E_g^{hh} - E_{ex} \quad ..2.22$$

The quantity E_1^{hh} is the confinement energy of the heavy hole. Similarly E_1^{e} is the confinement energy of the electron. E_{ex} is the exciton binding energy.

The nature of the band gap following interdiffusion can be computed using the composition profile given by (2.21). As a result of interdiffusion the initially rectangular profile adopts the form shown in Fig(2.17). These calculations can qualitatively explain the dependence of the blue shift on the indium content of the quantum wells.

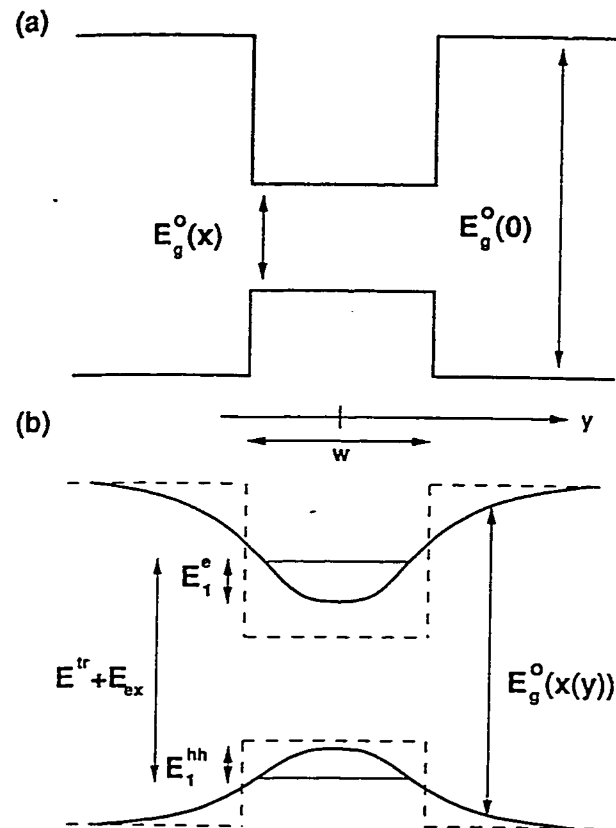

Fig 2.17 Schematic diagram showing the band structure of an InGaAs quantum well of width (w), (a) before and (b) after compositional disordering. [42].

Chapter 3.

EXPERIMENTAL PROCEDURES

In this chapter the experiments undertaken to study the diffusional homogenization of superlattice structures and associated experiments to examine the composition and strain dependence of the diffusion coefficient are outlined. Also experimental details of the ion implantation enhanced diffusion studies are covered.

The chapter is divided into two sections. In the first section the procedures followed in the long term (several hours in duration) diffusion experiments will be presented. Following this, details of the ion implantation enhanced diffusion experiments which involved rapid thermal annealing after implantation are discussed.

3.1.

3.1.1. Diffusional homogenization of superlattice structures. (SL10)

The superlattice structure used for this study consisted of $In_{0.2}Ga_{0.8}As$ quantum wells with GaAs as barrier layers. The $In_{0.2}Ga_{0.8}As$ wells were nominally 15 Å thick while the GaAs barriers were nominally 25 Å thick. A repeat structure consisting of ten such wells was grown to form the superlattice. The structure was grown on a [100] n GaAs substrate by molecular beam epitaxy (MBE) at McMaster.

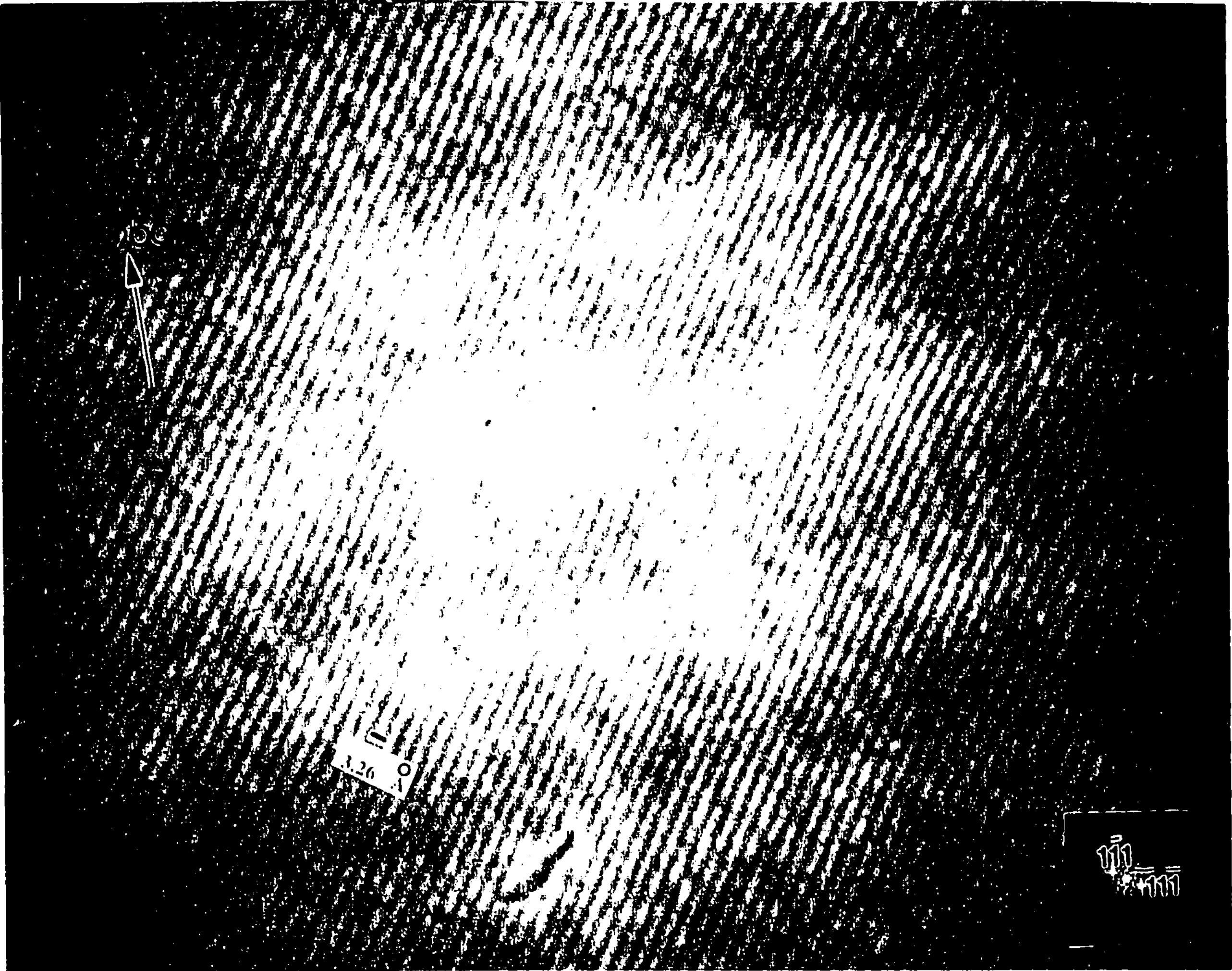

Fig 3.1 High resolution micrograph of the as grown superlattice SL10. The diffraction pattern is inset.

The thickness of the quantum well and the period of the superlattice were chosen to prevent any relaxation of the strained structure during annealing [50]. A high resolution TEM micrograph of the as grown structure is shown in Fig 3.1. In this micrograph the $In_{0.2}Ga_{0.8}As$ quantum wells are visible as darker bands and the GaAs barriers are visible as lighter bands. The spacing of the (111) fringes is marked on the micrograph. The superlattice periodicity was measured from similar micrographs.

During MBE growth the substrate was maintained at 515^0C and rotated at 30 rpm in order to maintain uniformity of composition over the wafer. The as - grown structure was characterized by X-Ray diffraction, Transmission Electron Microscopy (TEM) and low temperature (~15 K) photoluminescence (PL). By utilizing the position of the satellite peak in the X-Ray diffractogram a structural periodicity of 42.9 $\overset{0}{A}$ was deduced. Cross-sectional TEM samples were prepared by mechanical back polishing, dimpling and ion milling to electron transparency. Measurements on high resolution micrographs of the as grown structure (summarized above) yielded values for the period of the superlattice in good agreement with the values deduced from X-Ray diffraction. Transfer matrix simulations (described in more detail in section 5.1.5) of the as grown structure yielded values for the (N=1 level) transition wavelength which were also in good agreement with the experimental PL values. The nominal composition of the quantum well constituting the superlattice is therefore close to the target figure of 20% indium.

3.1.2. Annealing:

Homogenization of the above structures was conducted in a tubular resistance furnace at 850^0C for time periods ranging from 20 minutes to 12 hours. All heat treatments were carried out by evacuating the furnace to better than $2*10^{-5}$ Torr, back filling with high purity argon and maintaining an argon flow during annealing. The temperature was stabilized during homogenization to better than $\pm3^0$C. The evacuation is necessary as oxygen tarnishes the surface of the sample and this is deleterious to the intensity of the PL signal. During annealing the sample was covered with a block of GaAs to prevent loss of As. The sample covered with the GaAs block was enclosed in a graphite holder. For short term annealing experiments (20 - 40 minutes in duration) the graphite holder was held at the end of a long rod (also acting as a conduit for the thermocouple leads), which was inserted into the hot zone of the furnace when the temperature reached 850^0C and was quickly withdrawn when the annealing procedure was completed. For the longer time experiments (3 or more hours) the graphite holder was put on a porcelain boat which was inserted into the furnace before evacuation. In this case the temperature reached 850^0C after about 1 hour. Following annealing the diffused structures were characterized by photoluminescence, X-ray diffraction and TEM.

3.1.3. Photoluminescence:

A schematic diagram of the experimental setup used for photoluminescence studies in this thesis is shown in Fig (2.11) in the literature review. [10]. Low temperature photoluminescence was conducted by exciting a sample cooled to ~15 K with the 632.8 nm line of a He-Ne laser. The maximum output power of the laser was 10 milliwatt. Neutral density filters F2 help to vary the excitation power. The sample itself was maintained at a low temperature (~ 15K) with the help of a helium cryostat. The cooling of the sample is necessary to:

1. prevent thermal ionization of optically active centres.
2. to minimize thermally activated non radiative recombination processes.
3. minimize thermal broadening of otherwise sharp spectral features.

The laser beam is focused onto the surface of the sample by means of the lens. If the light originates in the surface layer or is attenuated in passing through a long path in the sample, a front surface geometry is usually employed. The physical condition of the incident surface of the sample is very important as it must be free from oxide layers and strain. The light emanating from the sample is focused on the entrance slits of the spectrometer by lenses L2 and L3. It can subsequently be focused by lens L4 onto the detector. The luminescence emanating from the sample was dispersed with a grating

and detected with a p-i-n InGaAs detector. From the calibrated spectral resolution of the grating, a resolution for the experimental setup of ~ 1.5 nm was deduced.

3.1.3(b) X-ray diffraction.

X-ray diffraction spectra were obtained on a Nicolet diffractometer. The source for the experiment was Cu Kα radiation at 1.54 Å. The 2θ range of interest in diffraction from the superlattice SL10 structure is 60 - 70 ^{0}. Typically, while acquiring the spectra from the diffused SL10 structures, this angular range was scanned with a step size of 0.01^0. As is described later in section 5.1.3, the X-ray diffraction spectra from the superlattice structure were characterized by satellite peaks about an average (400) peak. The position of these satellite peaks provides information about the periodicity of the structure. The intensity variation of these satellite peaks with annealing can also provide information about the In - Ga interdiffusion coefficient during annealing.

3.1.3(c) TEM (Transmission electron Microscopy)

Physical examination of several diffused and ion implanted structures were undertaken with both conventional and high resolution electron microscopy. As already mentioned above, TEM samples were prepared by mechanical polishing, dimpling and ion milling. Examination of samples using conventional bright field imaging was undertaken in a 120 kV Philips CM12 instrument. Conventional imaging provides information about the structural changes following diffusion and ion implantation. It also

provides crystallographic and size information about any extended lattice defects that accompany ion implantation and annealing.

High resolution imaging was performed with a 200 kV JEOL 2010F microscope. High resolution imaging was useful in quantifying the quantum well thickness changes that accompany diffusion and ion implantation. This data was used to obtain estimates of the In-Ga interdiffusion coefficient.

Attempts were also made to obtain the indium composition profile across some diffused InGaAs quantum wells. The data necessary to estimate such a composition profile was obtained through energy dispersive X-ray analysis undertaken in the JEOL 2010F microscope. In this experiment, a fine static, nominally $5\overset{0}{A}$ in size, electron probe is used to excite X-rays from a region of interest in the sample. The X-ray spectrum so obtained contains peaks from the elemental constituents of the excited area. The integrated intensity under characteristic peaks in the X-ray spectrum can be used to obtain compositional information from the region of interest. Further details of the experimental procedure and computational techniques used to extract compositional information from such experiments is provided in Appendix 2.

3.1.4. Structures grown to investigate the compositional dependence of the diffusion coefficient. (SD10, SD15, SD20, SD25, SD30)

Separate structures were grown to study the dependence of the diffusion coefficient on the composition. These structures consisted of a single and a double quantum well. A micrograph of the structure is provided in Fig 3.2. The structure consists of 2000 $\mathring{A}$ of GaAs on a [100] n GaAs substrate, on top of which is grown a 60 $\mathring{A}$ InGaAs quantum well. After further growth of 250 $\mathring{A}$ of GaAs, a double quantum well consisting of two 60 $\mathring{A}$ InGaAs quantum wells separated by a 25 $\mathring{A}$ GaAs barrier was grown. Finally the structure was capped with 100 $\mathring{A}$ of GaAs. The InGaAs wells were of varying In composition, 10%, 15%, 20%, 25% and 30%. It was later observed that the double quantum well in the 25% In structure had developed a non planar morphology. This was also the case for the 30% structure. The influence of strain on the morphological evolution of the quantum well-barrier interface can be understood in terms of discussion in section 2.1 of the literature review [12]. In consequence the subsequent analysis concentrated on structures that contained up to 20% indium. As will be explained in section 5.1 a linear one dimensional model of diffusion is used to explain the trends seen in PL from the diffused structures. Since this approach is valid only if the quantum well-barrier interface has a planar morphology attention was confined to structures containing up to 20% In.

Diffusional homogenization of the above structures was conducted following the same procedures used for the superlattice structure. Most of the work concentrated on

the 20% In sample in order to extract kinetic parameters required for modeling the evolution of the superlattice. Diffusion anneals were conducted on the 20% In structure for 8 hours at 750 ^{0}C and 800 ^{0}C and for 6, 8 and 12 hours at 850 ^{0}C. 8 hour anneals at 850 ^{0}C were also carried out for the 10% and 15% In structures to compare the PL shift with the 20% In structure. 8 hour anneals were also conducted on the 25% In and 30% In samples, again to characterize the PL shift and to compare the data with that of the 20% In structure treated under identical conditions.

3.1.5. Structures grown to study the influence of strain on the diffusion coefficient. (100S3, 311S3)

In a strained system like InGaAs/GaAs the strain energy due to lattice misfit may be an important factor in the diffusion process. In order to assess the importance of strain enhanced diffusivity, nominally identical structures consisting of three quantum wells of different compositions were grown on two different substrate orientations [100] and [311]A. (Conventionally group III terminated planes are labeled A). These structures consisted of 2000 Å of GaAs grown on the substrate followed by three 60 Å InGaAs quantum wells separated by 200 Å GaAs barriers. The quantum wells nominally contained 20%, 15% and 10% In with the 10% well situated nearest to the surface. The structure was capped with 200 Å of GaAs (Fig 3.3).

Diffusional homogenization of these structures was carried out following the same procedure as the previous samples. After the diffusion runs, PL was used to compare the shifts in luminescence from the various quantum wells in the two substrate orientations and hence gauge the influence of strain on interdiffusion.

3.2

3.2.1 Ion Implantation enhanced diffusion

This portion of the project involved active collaboration with the National Research Council (NRC) at Ottawa and the University of Western Ontario (UWO) in London. Samples implanted at the Tandetron ion implanter at the UWO and rapid thermally annealed (RTA) at 850^{0}C for various periods of time at NRC were characterized by TEM.

Two sets of samples were examined. The first set were AlGaAs/GaAs based structures. The second set of samples consisted of InGaAs/GaAs based structures. The AlGaAs/GaAs structure consisted of two 60$\overset{0}{A}$ GaAs wells enclosed by AlGaAs cladding. The upper quantum well was located 1.8μm below the surface of the sample, and was covered with AlGaAs cladding. The cladding had two different Al compositions. One set of structures (A1) consisted of $Al_{0.7}Ga_{0.3}As$ barriers while the second (A2) consisted of $Al_{0.2}Ga_{0.8}As$ barriers. The A1 specimens contained a set of 15$\overset{0}{A}$ thick GaAs planarization layers in the lower $Al_{0.7}Ga_{0.3}As$ cladding while in the A2

Fig 3.2 As grown SD15 structure, **g**=(200)

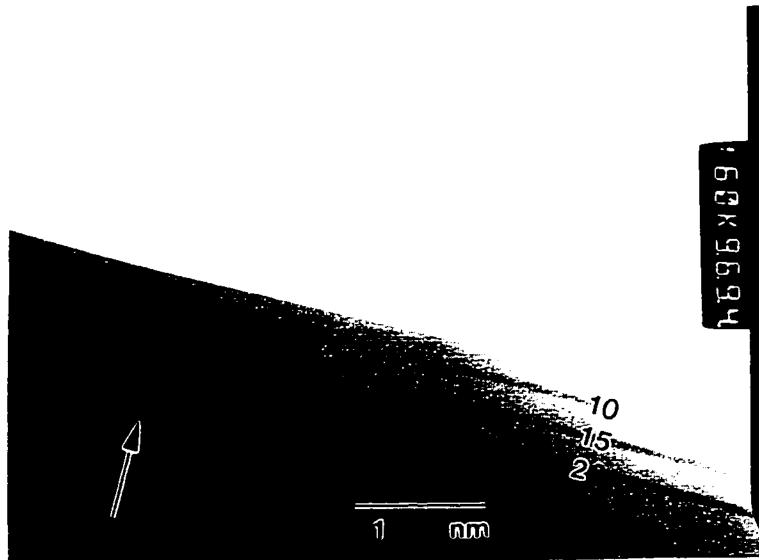

Fig 3.3 (a) As grown 100S3 structure. **g** = (200). The indium contents in % are marked on the various wells.

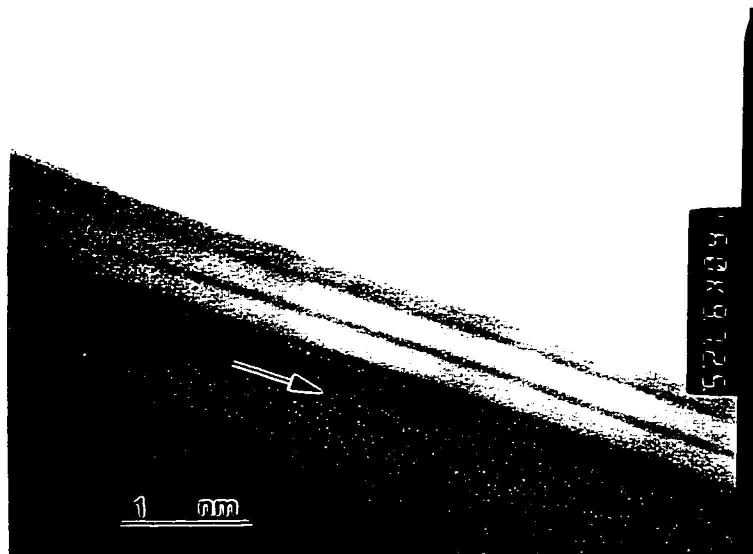

Fig 3.3 (b) As grown 311S3 structure. **g** = (02$\bar{2}$).

structure there were no planarization layers. The $Al_{0.7}Ga_{0.3}As$ based structures(A1) were implanted with As^+ at energies ranging from 1.1 to 8 MeV (dose of $2.5*10^{13}$ /cm^2 at a temperature of 200^{0}C) and rapid thermally annealed at 850 ^{0}C for a total of 105 seconds. TEM characterization of the above samples was undertaken to study the crystallographic nature of implant damage, the location of implant damage and quantum well thickness changes following implantation and annealing. A micrograph of the as grown (RTA only) A1 structure is provided in Fig 3.4. In this micrograph two 60 $\overset{0}{A}$ GaAs quantum wells are visible in the middle of the photograph. Three 15 $\overset{0}{A}$ GaAs planarization layers are also visible in the lower cladding. With similar objectives in mind characterization of the structure A2 was also undertaken. The (RTA only) structure is seen in Fig 3.5. The GaAs quantum wells are arrowed in the micrograph. There is less contrast between the GaAs quantum wells and the $Al_{0.2}Ga_{0.8}As$ barrier in this sample as compared to A1 (Fig 3.4), because of the smaller composition difference between the well and the barrier.

The second set of samples were AlGaAs/ GaAs/InGaAs/ AlGaAs based. Once again two sets of structures were studied. The first (I1) was a graded index, separate confinement structure consisting of AlGaAs cladding 1.8μm thick, graded in composition from 20% to 70% Al. The separate confinement portion of the heterostructure consists of two $In_{0.21}Ga_{0.79}As$ quantum wells 60 $\overset{0}{A}$ thick separated by

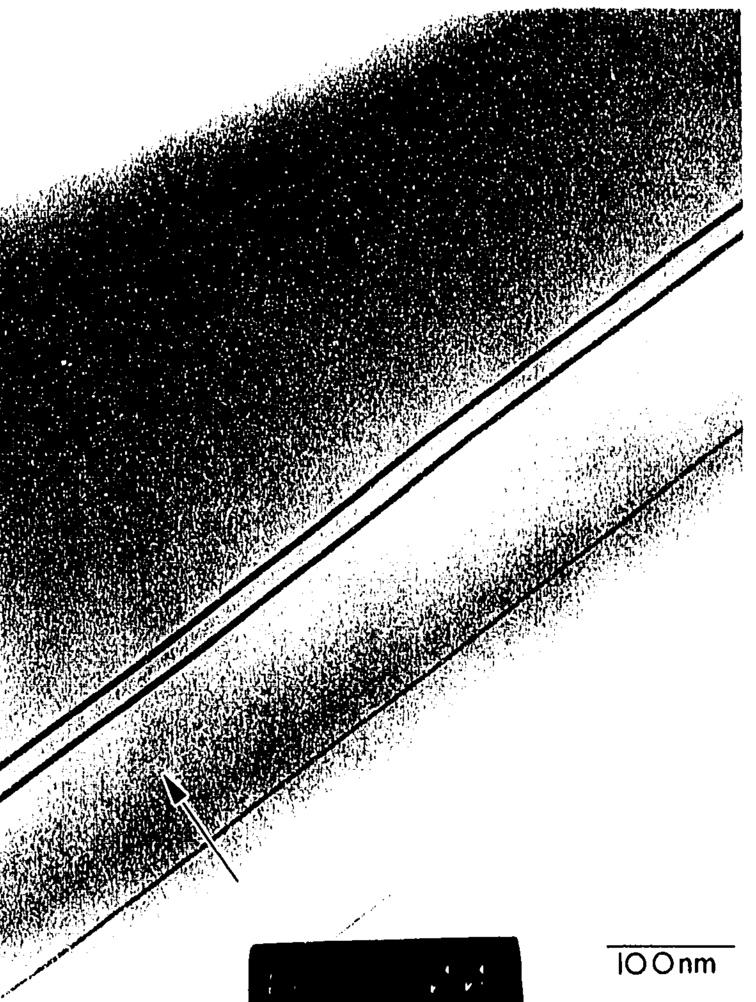

Fig 3.4 As grown $Al_{0.7}Ga_{0.3}As$/ GaAs structure (A1). g= (002).

Fig 3.5 As grown $Al_{0.2}Ga_{0.8}As$/GaAs structure (A2). **g** = (002).
(The two GaAs quantum wells are arrowed).

GaAs barriers. In this structure (as in the case of A1) planarizing GaAs layers were grown in the lower graded AlGaAs cladding. It has been demonstrated that growth of these planarizing layers getters impurities during growth and dramatically improves the electrical properties of the heterostructure (carrier mobilities are reported to be superior). [25]. Stucture I1 was grown in both doped and undoped configurations. In the doped configuration the structure was of the p-i-n type with the upper cladding doped P type ($\sim 10^{19}/cm^3$ with Be) while the lower cladding was doped N type (to the same level) with Si. Fig 3.6 provides a micrograph of the as grown undoped I1 structure, showing clearly the planarization layer in the lower cladding. Also visible at the top of this micrograph is the separate confinement portion of the structure. The two $In_{0.21}Ga_{0.79}As$ quantum wells with GaAs barriers can easily be discerned. In the second set of structures (I2) the cladding layer was uniformly GaAs. Two $In_{0.23}Ga_{0.77}As$ 60 $\mathring{A}$ thick, quantum wells were grown with 1.7μm of GaAs cladding. A micrograph of a 1.1 MeV As^+ implanted structure is seen in Fig 3.7. The quantum wells can be seen in the middle of the figure. Structure I1 was implanted with As^+ ions having energies varying from 1 to 8 MeV. While the dose was maintained at $2.5*10^{13}$ /cm^2 the implant temperature was varied from 77K to 473 K. The purpose of these temperature variation experiments was to study the variation of the photoluminescent blue shift as a function of implant temperature. The results of these experiments are provided in the next chapter. Rapid thermal anneals at 850^0C were conducted for a total of 90 seconds. Following PL characterization of these

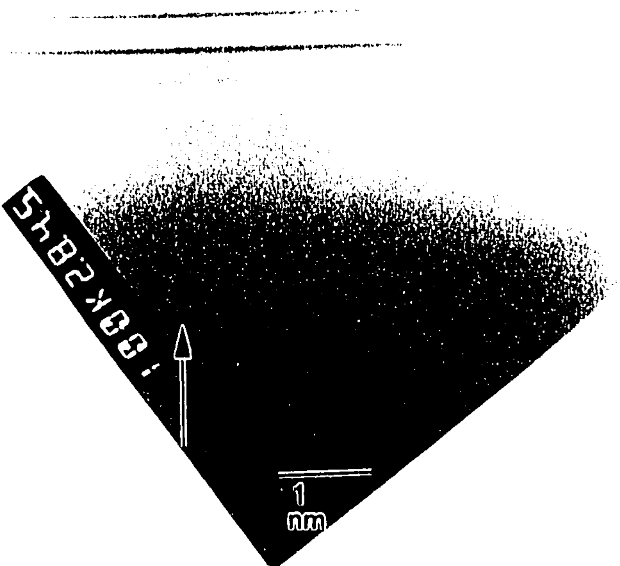

Fig 3.6 As grown AlGaAs/ GaAs/InGaAs graded index structure (11). g = (002).

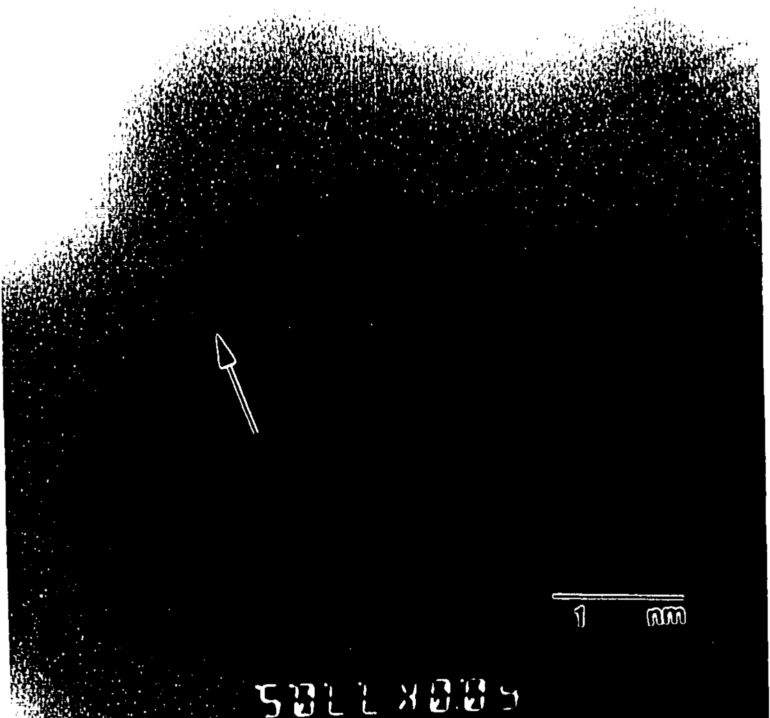

Fig 3.7 1.1 MeV As^{+} implanted GaAs/InGaAs structure (12). g = (002) .

structures, only certain samples showing interesting features in the PL tests were examined by TEM. While the objectives remained the same as in the case of the AlGaAs/GaAs experiments, the effects of implantation temperature and sample doping on the position of implant damage were also examined. PL examination of the A1, A2 samples revealed that at high implant energies (6-8 MeV) intensity recovery after implant and annealing was poor. Consequently longer annealing times (105 seconds) were used in these structures as compared to the I1, I2 structures which were annealed for 90 seconds. In all the implants mentioned above one half of the sample was masked before implantation, so that only half of the sample was disordered by the ion-beam. This enabled a comparison of the RTA only and implant and RTA effects in the same sample.

Chapter 4.

EXPERIMENTAL RESULTS.

In this chapter results from the superlattice homogenization experiments, followed by results from the samples chosen to study the compositional dependence and the strain dependence of the diffusion coefficient are summarized. The latter half of this chapter compiles the characterization results from the ion implanted samples.

4.1. Results from the homogenization of superlattice SL10 structures.

The SL10 superlattice consisted of 10 $In_{0.2}Ga_{0.8}As$ quantum wells with GaAs barrier layers. The quantum wells were nominally 15 Å thick, while the intervening GaAs barrier layers were 25 Å thick. As was outlined in the previous chapter, three different techniques were used to characterize the diffused samples. Low temperature photoluminescence (PL) was used to follow the movement of the luminescent wavelength with compositional change. Physical examination of the structures was conducted through TEM. Both a 120 kV (Philips CM12) and a high resolution (JEOL 200 kV) microscope were employed. X-ray diffraction spectra were obtained using a Nicolet ω-2θ diffractometer.

4.1.1. Cross-sectional TEM results:

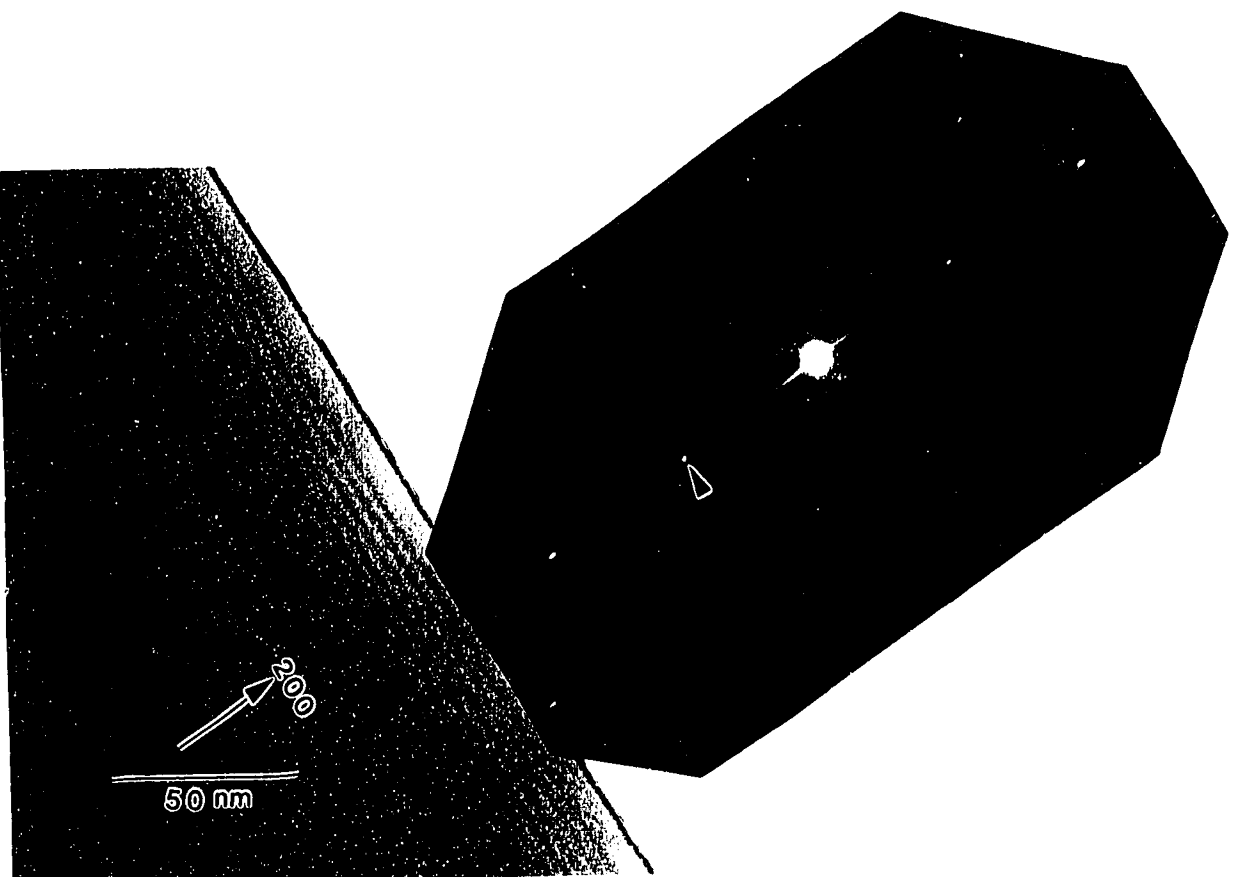

Fig 4.1.1 As grown SL10 structure with diffraction pattern. g= (200)
The arrow in the diffraction pattern points to ($\bar{2}00$)

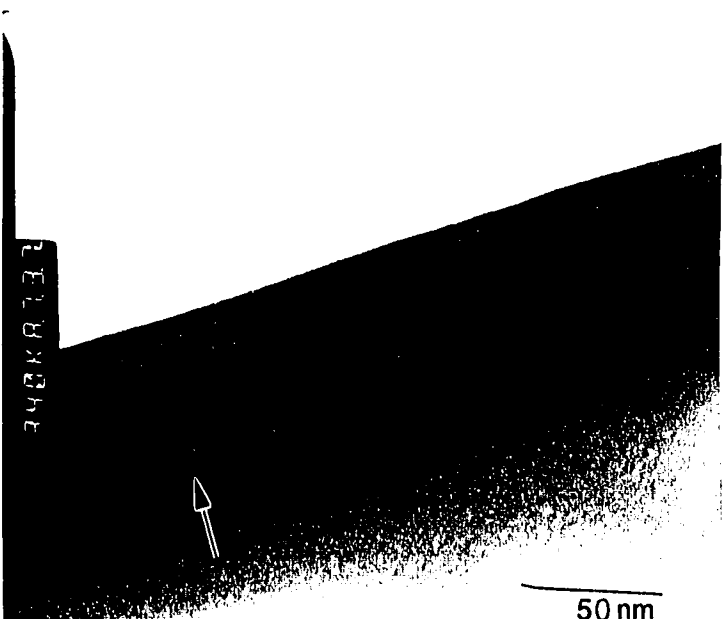

Fig 4.1.2 SL10 structure annealed at 850^0 C for 20 minutes. **g**=(200)
(Note the superlattice is still visible)

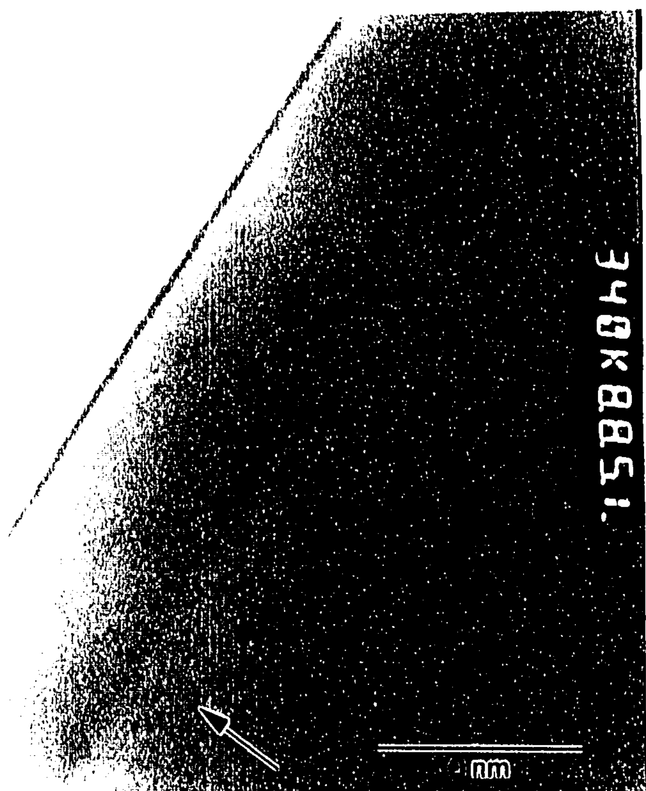

Fig 4.1.3 SL10 structure annealed at 850^0 C for 6 hours . **g** = (200)
(The superlattice at this stage is diffused out)

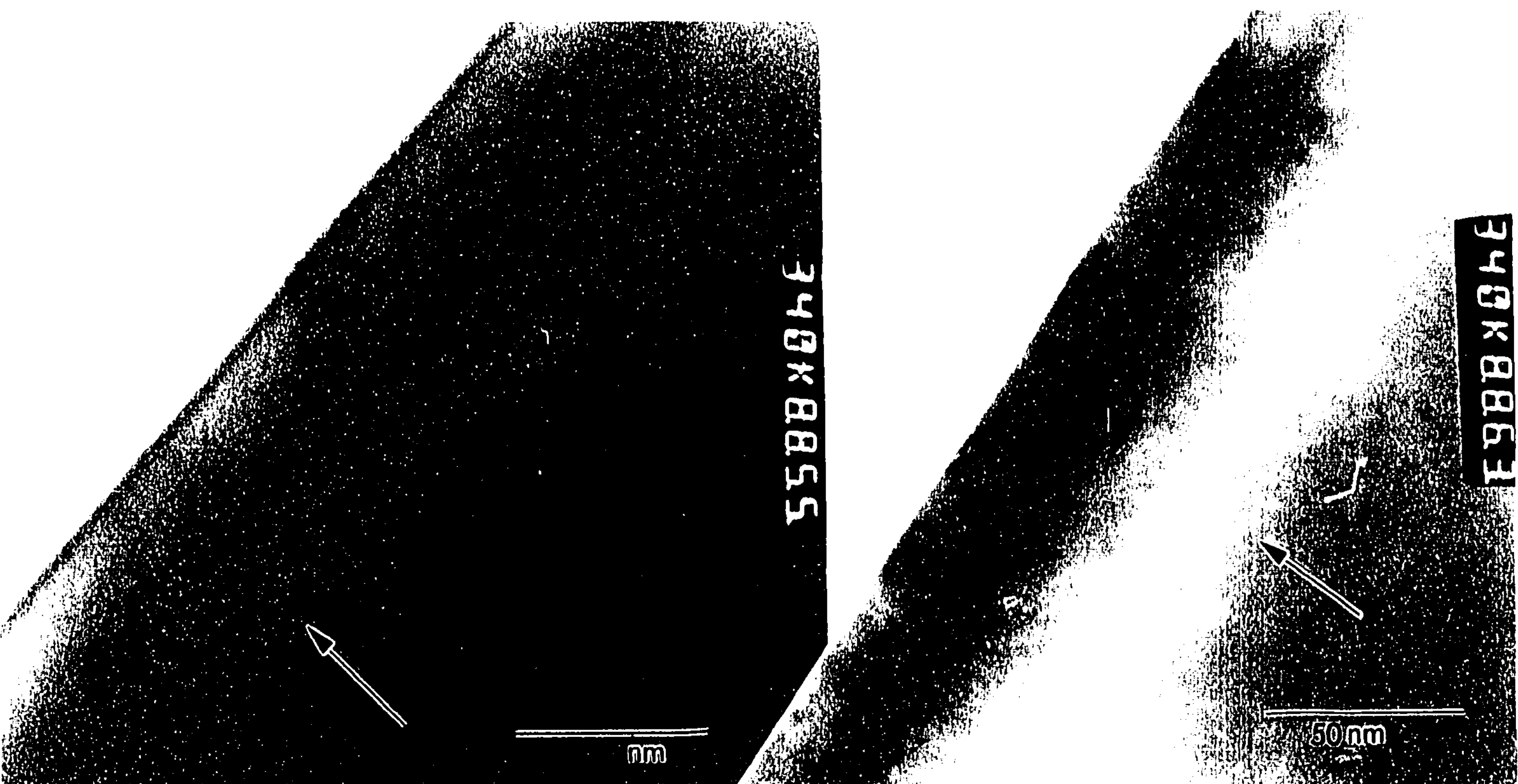

Fig 4.1.4 SL10 structure annealed at 850^0 C for 8 hours . g= (200)   Fig 4.1.5 SL 10 structure annealed at 850^0 C for 12 hours g = (200)

Fig 4.1.1 is a micrograph from the as-grown structure and the corresponding diffraction pattern. The satellite peaks about the $(\bar{2}00)$ spot in the diffraction pattern are arrowed and can easily be seen. These satellite peaks are a consequence of the periodicity presented to the incoming electrons by the superlattice structure. A high resolution micrograph of the as-grown structure (Fig 3.1) confirms that the period of the superlattice is ~ 42 $\overset{0}{A}$. Micrographs from the 20 minutes, 6 hours, 8 hours and 12 hours annealed structures are shown in figures 4.1.2, 4.1.3, 4.1.4, 4.1.5 respectively. As can be seen at the end of 20 minutes annealing the $In_{0.2}Ga_{0.8}As$ quantum wells are still visible (Fig 4.1.2) while in the six hour annealed structure (Fig 4.1.3) the individual wells are no longer visible. Following diffusion for 6 hours at 850^0C the superlattice anneals out to give an indium enriched region ~ 400 $\overset{0}{A}$ thick. Simulations based on the two beam theory of electron diffraction suggest that after 12 hours of annealing only a region slightly enriched in indium remains. (Appendix 6).

4.1.2. X-Ray diffraction:

Fig 4.2 presents the evolution of the X-Ray diffraction spectra with annealing. The as grown structure clearly shows the (400) diffraction peak from the substrate(marked S), a peak from the average superlattice (marked A) and satellite peaks about this average peak (marked S1 and S2). From the position of the satellite peak marked S1 the periodicity of the superlattice is calculated to be 42.9 $\overset{0}{A}$, in good agreement with the value obtained from high resolution TEM. Following diffusion for 6 hours it is clear that

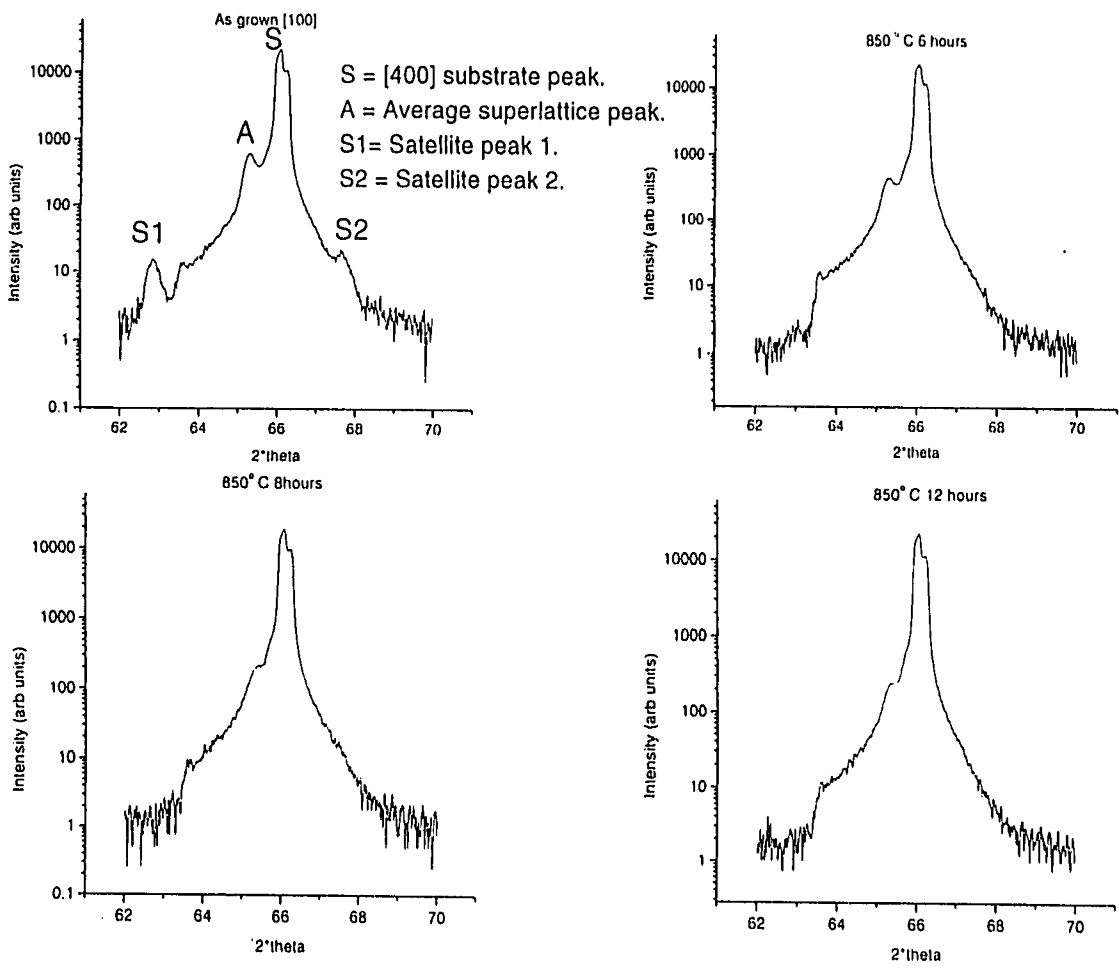

Fig 4.2 Evolution of the X-ray diffraction intensity with annealing superlattice structure SL10.

the satellite peak can no longer be distinguished. The same observations were made for both the 8 hours and the 12 hours annealed samples.

4.1.3. Photoluminescence.

A number of interesting trends were seen in the photoluminescence results summarized in Fig 4.3. The peak from the as grown sample was located at 877 nm. PL measurements of a few as grown samples did not reveal any significant variations in the position of the peak. Following diffusion for 20 minutes this peak has shifted to a longer wavelength of 890 nm. Still longer annealing times of 6 hours and 8 hours, however result in the peak shifting to shorter wavelengths, 883 nm and 878 nm respectively. The peak widths of the PL also show a few notable features. As the quantum well interfaces become diffuse over an annealing time of 8 hours the PL peak width increases. In summary at annealing times of upto 8 hours there was a red shift of luminescence followed by a blue shift after 12 hours annealing. The spectrum of the 20 minute annealed sample was acquired at NRC, while the remaining spectra were acquired at McMaster. In consequence the wavelength range and intensity scales of the 20 minute spectrum differ from the remaining spectra. Elucidation of the nature of the transitions

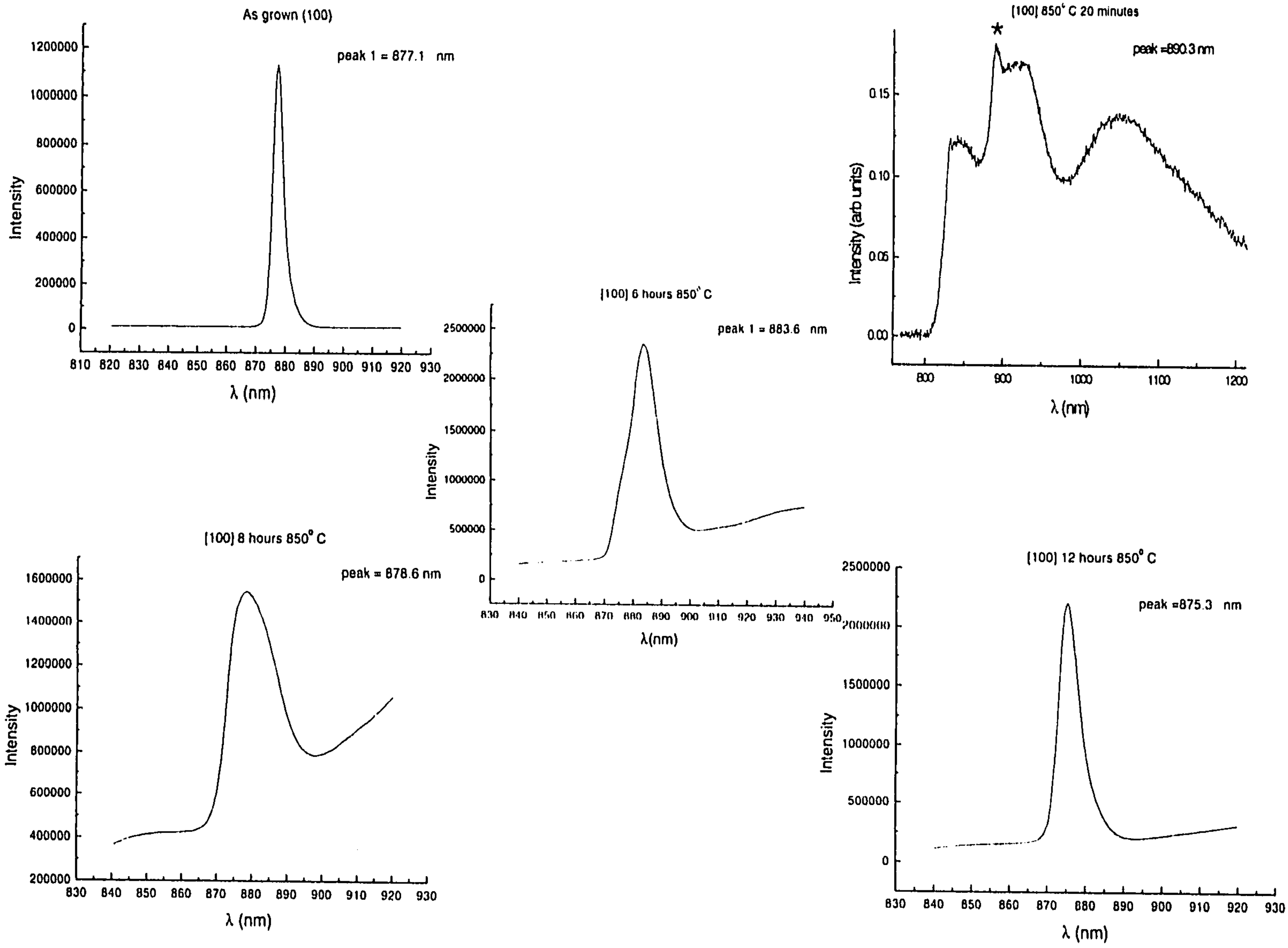

Fig 4.3 Evolution of the PL from the superlattice SL10 structure.

on the lower energy shoulder of the superlattice peak in this spectrum would require time resolved studies. Such studies were however not undertaken in this work.

4.1.4. Results from the diffusion of SD samples.

To recapitulate these structures consisted of a single and double quantum well. The structure was composed of 2000 $\mathring{A}$ of GaAs on a [100] n GaAs substrate, on top of which was grown a 60 $\mathring{A}$ InGaAs quantum well. After further growth of 250 $\mathring{A}$ of GaAs, a double quantum well consisting of two 60 $\mathring{A}$ InGaAs quantum wells separated by a 25 $\mathring{A}$ GaAs barrier was grown. Finally the structure was capped with 100 $\mathring{A}$ of GaAs. The quantum wells in this structure were grown in various indium compositions ranging from 10 to 30% In. (SD10, SD15, SD20, SD25, SD30).

Extensive TEM characterization of only the SD20 structures was undertaken. Low temperature PL spectra from structures ranging in composition from (10-30% In) were used to follow the shifts in luminescence. A set of micrographs is provided in Fig 4.4 which trace the thickness increase of the single quantum well in the SD20 structure for the experimental conditions indicated on each micrograph. The thickness increase with annealing was obtained by taking the average of the quantum well thickness measured at several places in high resolution micrographs. The thickness of the single quantum well

in the as - grown structure was ~ 60 $\overset{0}{A}$ ± 3 $\overset{0}{A}$, while the 750 ^{0} C, 800 ^{0} C and 850 ^{0} C samples have thickness ~ 67 $\overset{0}{A}$, 75 $\overset{0}{A}$, 92 $\overset{0}{A}$ respectively. There is an error of ± 3 $\overset{0}{A}$ associated with each of these measurements. As is explained later in section 4.2.1 this error is associated with the (002) fringe spacing in high resolution micrographs. The trends seen in the photoluminescence from some of these structures are presented in Fig 4.5 as a function of annealing temperature and time. These spectra trace the movement of the PL peak as a result of annealing the SD20 structure. The PL peak due to the single quantum well in the SD20 structure is marked as peak1 in all the spectra. As can easily be seen annealing the structure results in the peak shifting to shorter wavelengths, (blue shifting). The extent of shifting increases with increasing temperature for the same annealing time. Table 4.1 summarizes the results from the PL measurements of samples of other compositions. From the resolution of the PL measurement an error value of ~0.5 meV was deduced for the blue shifts reported in the table. Clearly on comparing the blue shift of samples with quantum wells of increasing indium content, for the same annealing conditions, an increase in the blue shift can be discerned. As noted earlier the sample with 30% In probably has a non planar well morphology in the as grown state. This was apparent from examination of the 25% In sample which already had a non planar interface at the junction with the barrier layer. Nevertheless a distinct trend of increasing blue shift with increasing indium content is clearly evident. However in the discussion section (Chapter 5) an argument will be

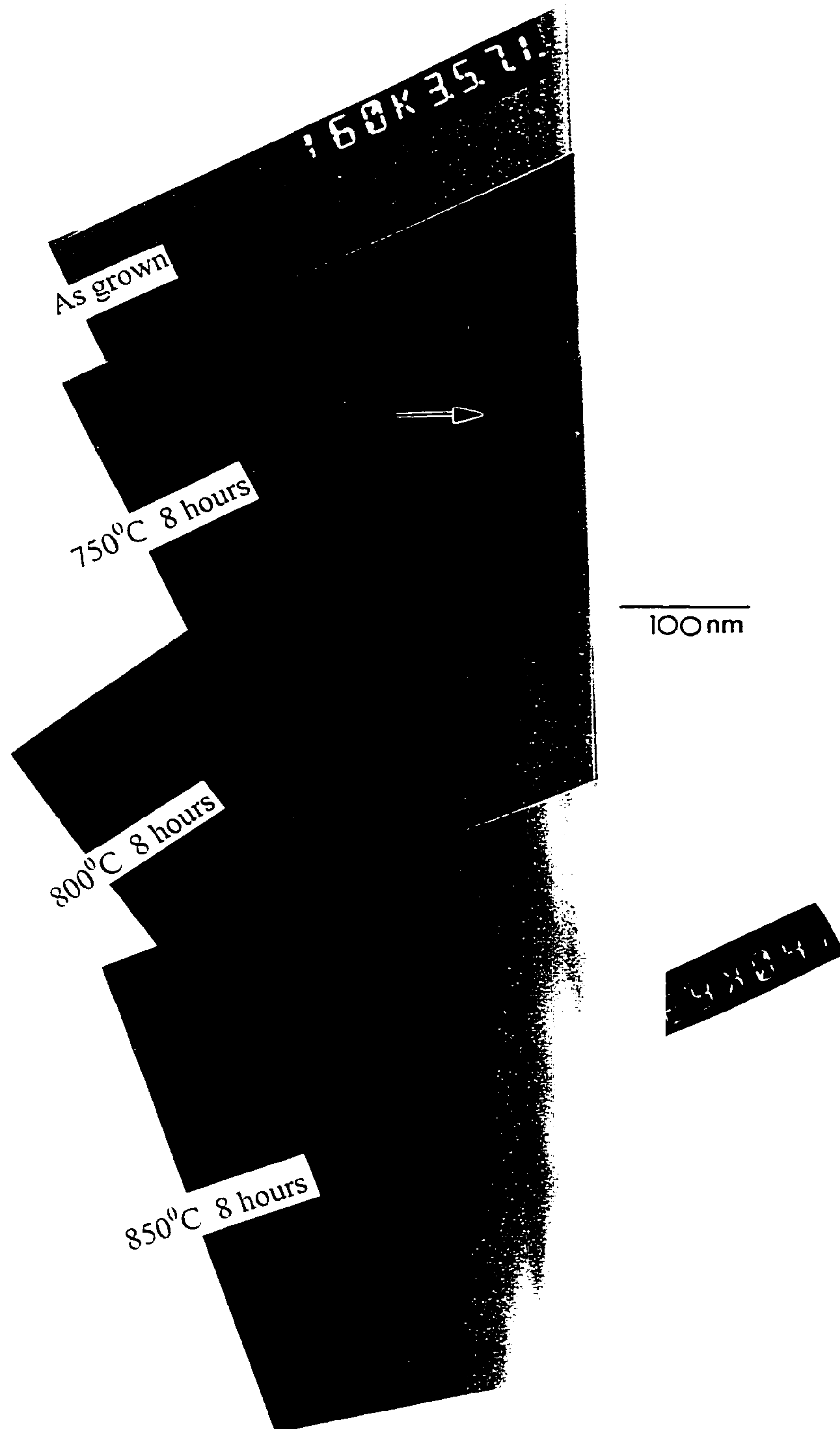

Fig 4.4 SD20 structural evolution as a function of annealing temperature. **g** = (200) .

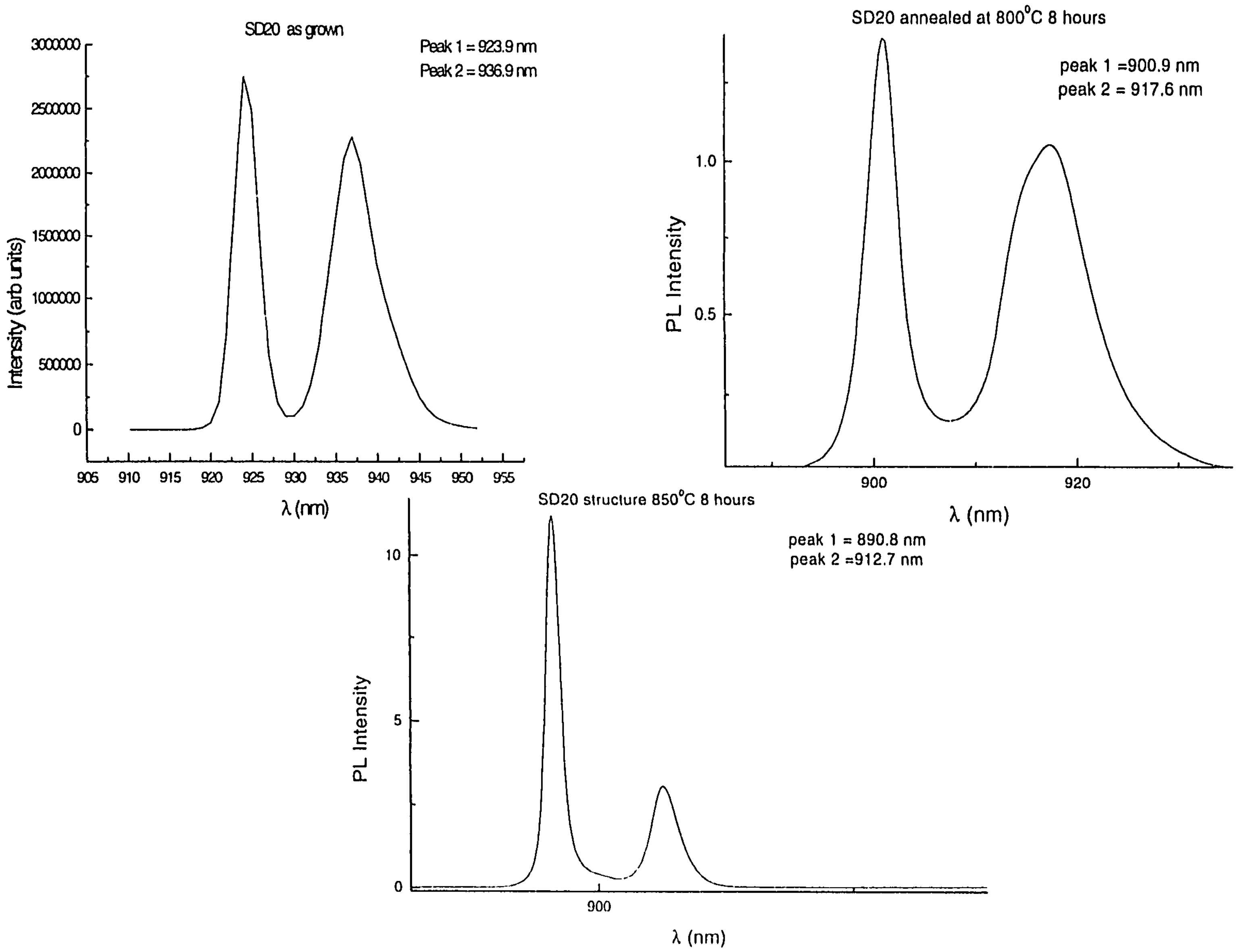

Fig 4.5 Trends in the PL intensity from SD20 structure.

Table 4.1. Comparison of blue shifts from SD samples with various indium contents.

Sample	As grown	750^{0}C 8 hours(nm)	Shift (meV)	800^{0}C 8 hours(nm)	Shift (meV)	850^{0}C 6 hours(nm)	Shift (meV)	850^{0}C 8 hours(nm)	Shift (meV)	850^{0}C12 hours (nm)	Shift (meV)
SD10	866							857.6	14.1		
SD15	906.3							887.8	28.4		
SD20	924	911	19	900.9	34.2	899	37.1	890.8	50.7	884.9	59
SD25	965							904	86.4		
SD30	1066.6							947	146.2		

presented to show that this alone is not evidence of a composition dependence of the diffusion coefficient.

4.1.5. Results from the diffusion of 100S3, 311S3 structures. As explained in section 3.1.5 of Chapter 3 these structures were grown to examine the effect of strain on the diffusion coefficient. They consisted of 2000 $\overset{0}{A}$ GaAs grown on the substrate followed by three 60 $\overset{0}{A}$ InGaAs quantum wells separated by 200 $\overset{0}{A}$ GaAs barriers. The quantum wells nominally contained 20%, 15% and 10% In, with the 10% well situated nearest to the surface. In the 100S3 structure the GaAs substrate was oriented along [100] while in the 311S3 structure the substrate was oriented along a [311] A direction.

PL results from samples annealed under identical conditions are compared in figures 4.6 and 4.7. In both cases the luminescence from the 10%,15% and 20% wells can be clearly discerned in the as-grown sample. The 10% well has the largest band gap and hence the shortest luminescent wavelength, while the 20% In well has the longest wavelength. The value for the 15% In well lies between the values for the 10% and 20% In samples. The luminescent wavelengths of the wells from the [100] substrate and [311]A substrates in the as-grown sample are comparable. As will be explained at some length in the discussion section, a difference in the wavelengths of PL from [100] and [311] oriented structures is expected, because in the [311] oriented structure an extra potential drop is present because of the piezoelectric effect. Since the experimentally

determined wavelengths are comparable it appears that the effect of the piezoelectric potential drop across the wells (which tends to tilt the quantum well) in the case of the [311] A type substrate is not significant. For both orientations of the substrate on 6 hours and 8 hours of annealing two transitions were found to emanate from the 15% well. This situation can potentially arise if the quantum wells relax and misfit dislocations are introduced. A TEM examination of annealed samples did not reveal the presence of misfit dislocations. Consequently it appears that the lower energy (longer wavelength) transition probably arises from a heavy hole energy level and the higher energy transition (shorter wavelength) arises from a light hole level. A comparison of the shifts of the 10% In well from the 6 hour anneal reveals that in the case of the [311] A type substrate a larger blue shift of 1.6 nm is obtained as compared to the [100] type structure. A comparison of the shifts of the lower energy transition of the 15% In well for the two substrate orientations in the 8 hour annealed samples, reveals that in the case of the [311] A orientation, the blue shift is larger by 4.9 nm as compared to the [100] oriented structure. The blue shift of the luminescence from the 15% In well in [311]A oriented sample is 42.3 meV. In the [100] oriented structure the shift is 34.1 meV. The difference between the two blue shifts is just ~ 8 meV. This result suggests that the effect of strain on the interdiffusion is not marked for the composition range studied. In the discussion section an estimate of the enhancement of the diffusion coefficient due to strain in the structure is made. As a result of those calculations it is shown that the above experimental results are to be expected.

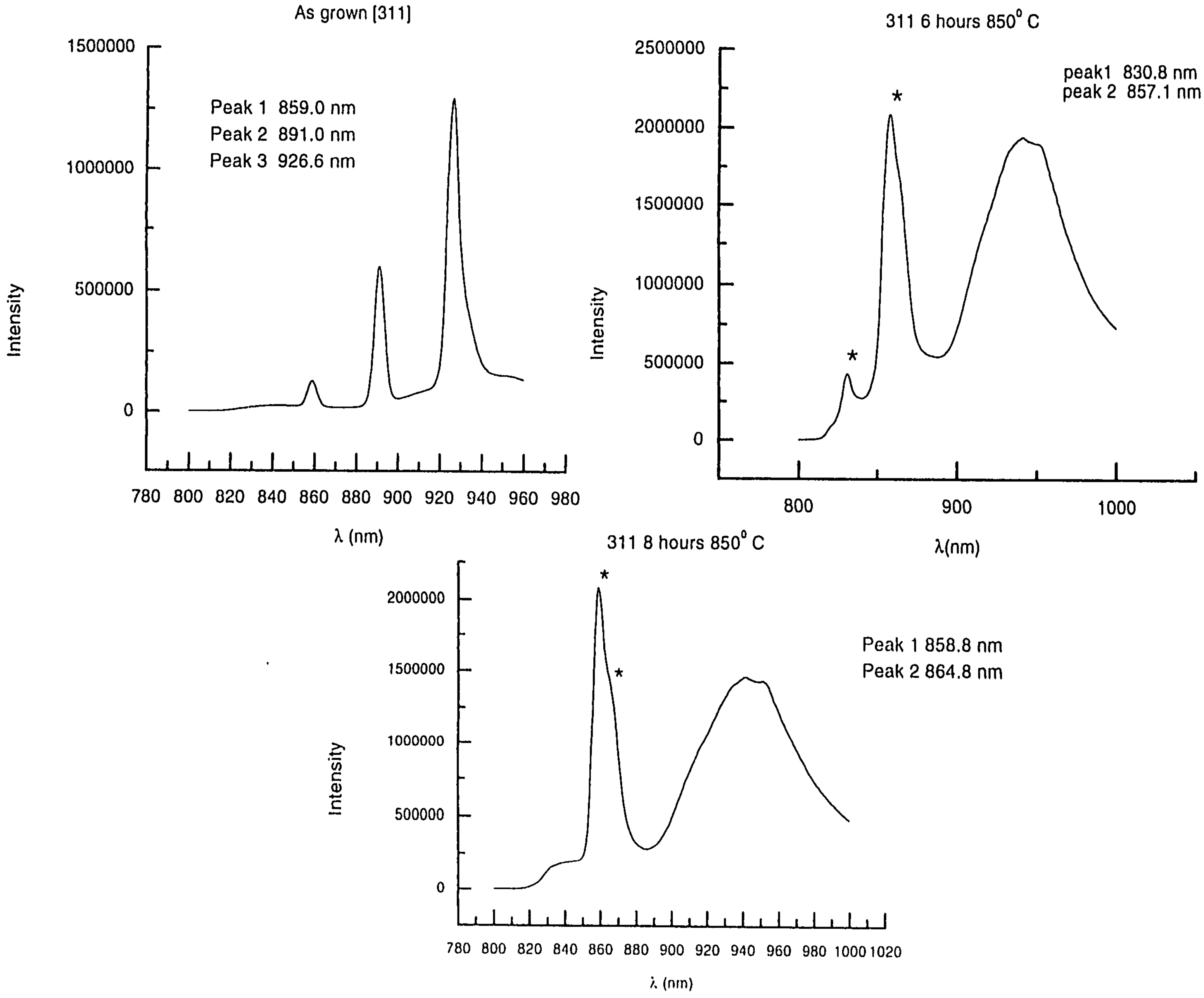

Fig 4.6 Evolution of the PL intensity from the [311] A structure.

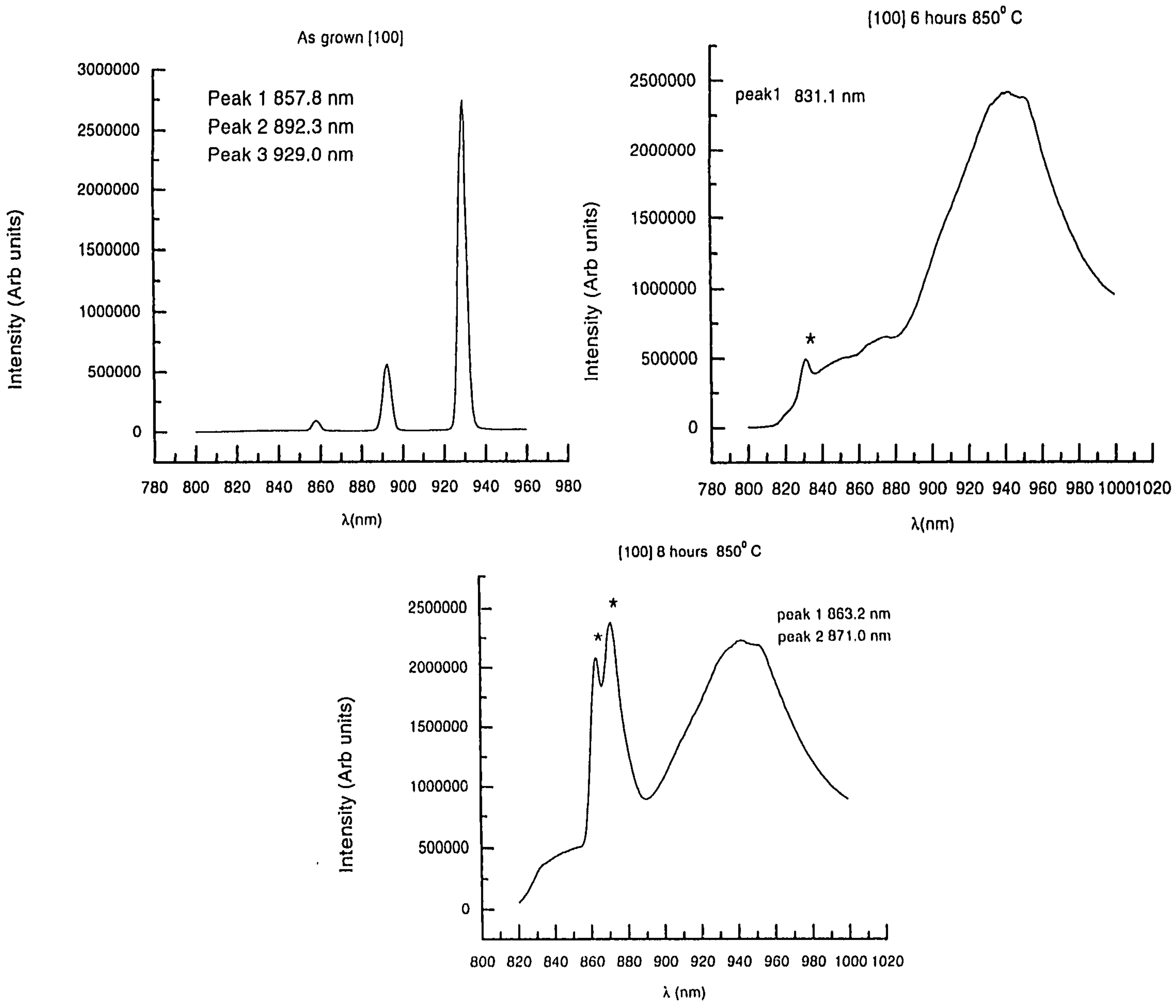

Fig 4.7 Evolution of the PL intensity from the [100] structure.

4.2. Experimental findings on the ion implanted and rapid thermally annealed structures.

4.2.1. AlGaAs/GaAs structures: As was explained in the experimental details of Chapter 3 two different structures were examined. The first of these, **A1**, was an $Al_{0.7}Ga_{0.3}As/GaAs$ structure with two 60 $\overset{0}{A}$ GaAs quantum wells. The cladding was 1.8 μm thick. The lower $Al_{0.7}Ga_{0.3}As$ cladding had a set of 15 $\overset{0}{A}$ thick GaAs planarization layers. The second structure A2, was a $Al_{0.2}Ga_{0.8}As/GaAs$ structure with two 60 $\overset{0}{A}$ thick GaAs quantum wells and no planarization layers in the lower cladding. The results of ion implantation and annealing of these structures are discussed below.

(A1) : These structures were implanted with As^+ ions with energies in the range of 1.1 MeV to 8 MeV. The projected range of the ions at 1.1 MeV is considerably less than the depth of the quantum well ; at 2 MeV the projected range is in the vicinity of the quantum well, while it is well below the depth of the quantum wells at 6 and 8 MeV respectively. The progression of implant damage following rapid thermal annealing at 850^0 C for a total of 105 seconds is shown in the micrographs of Fig 4.8. For the case of the 1.1 MeV implant the end of range damage, marked by dislocation loops, is located ~ 1 μm below the surface. For the 2 MeV implant the end of range is within 0.5 μm of the quantum wells, which are located 1.8 μm below the surface of the sample. In this case the occasional loop at the depth of the well can be discerned. The 6 MeV implant produces dislocation loops located ~ 0.6 μm below the quantum wells. These dislocation loops were preferentially located at the GaAs planarization layers in the

Fig 4.8.1 Al sample implanted with As^+ 1.1 MeV, **g** = $(2\bar{2}0)$ Fig 4.8.2 Al sample implanted with As^+ 2.0 MeV, **g** = $(2\bar{2}0)$

Fig 4.8.3 Al sample implanted with As^+ 6.0 MeV. g = ($\bar{2}$20)

Fig 4.8.4 Al sample implanted with As^+ 8.0 MeV. g = (004)

$Al_{0.7}Ga_{0.3}As$ cladding. A similar feature was found in the case of the 8 MeV implanted sample. By **g.b** analysis it was determined that most loops vanished when the TEM specimen (foil) was oriented so that the (002) reciprocal lattice vector was diffracting. This indicates that the loops have a $[\bar{1}10]$ Burgers vector. The loops were also determined to be interstitial in character following the method proposed by Edmondson et al. [51]. The blue shift in the photoluminescence as determined by the group at NRC [52], also increases with the implant energy. These are tabulated in Table 4.2. A monotonic increase in the blue shift with implantation energy is discerned. Fig 4.8.5 exhibits TRIM predictions of the vacancy profile produced in the sample as a function of the As^{+} implant energy. The implications of the location of the quantum well with respect to the vacancy concentration profile are discussed in section (5.1.8) of Chapter 5. Fig 4.9 illustrates a set of micrographs that correspond to the as-grown, 1.1 MeV implanted and 8 MeV implanted samples. The thickness increase in the case of the 8 MeV structure can be clearly discerned. High resolution micrographs were used to measure the thickness increase with increasing implantation energy in the range spanning 1.1 MeV to 8 MeV. These are tabulated in Table 4.2. The TEM sample from the 1.1 MeV implant was too thick to perform high resolution imaging. Consequently only the other samples are reported. An error in the well thickness determination of ~ $3\overset{0}{A}$ is present in all these measurements. This error roughly corresponds to the fringe spacing in the micrographs of Fig 4.10. Finally Fig 4.10.1 and Fig 4.10.2 are high resolution images from the RTA (rapid thermal anneal) and implanted and RTA

Table 4.2. Structure A1. Implant energies, blue shifts and well thickness after RTA at 850^{0}C for 105 seconds.

Treatment	PL(nm)	Shift(nm)	Shift(meV)	Thickness Å
As Grown	764.3			60
1.1 Mev As^+	762.3	− 2	4.3	
2 Mev As^+	731.6	− 32.7	72.7	72
6 Mev As^+	686.6	− 77.7	184.1	91
8 Mev As^+	671.8	− 92.5	224.0	98

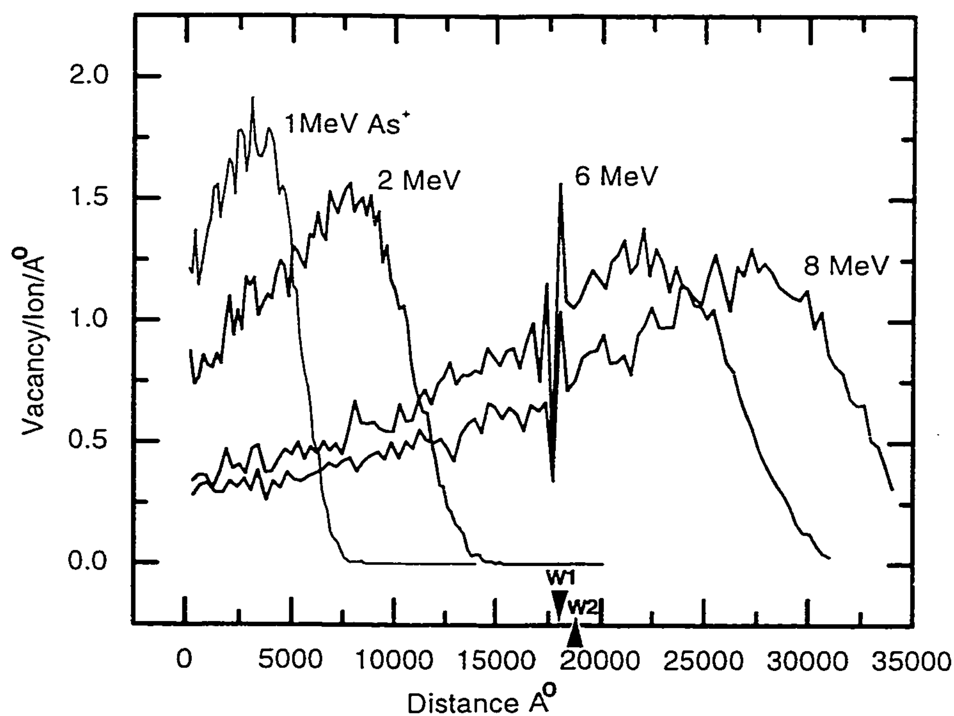

Fig 4.8.5 TRIM predictions of vacancy profiles in A1 samples after As^+ implants at varying energies. The approximate centres of the quantum wells are marked.

Fig 4.9 Evolution of well thickness in A1 sample with implant energy.

g = (002)

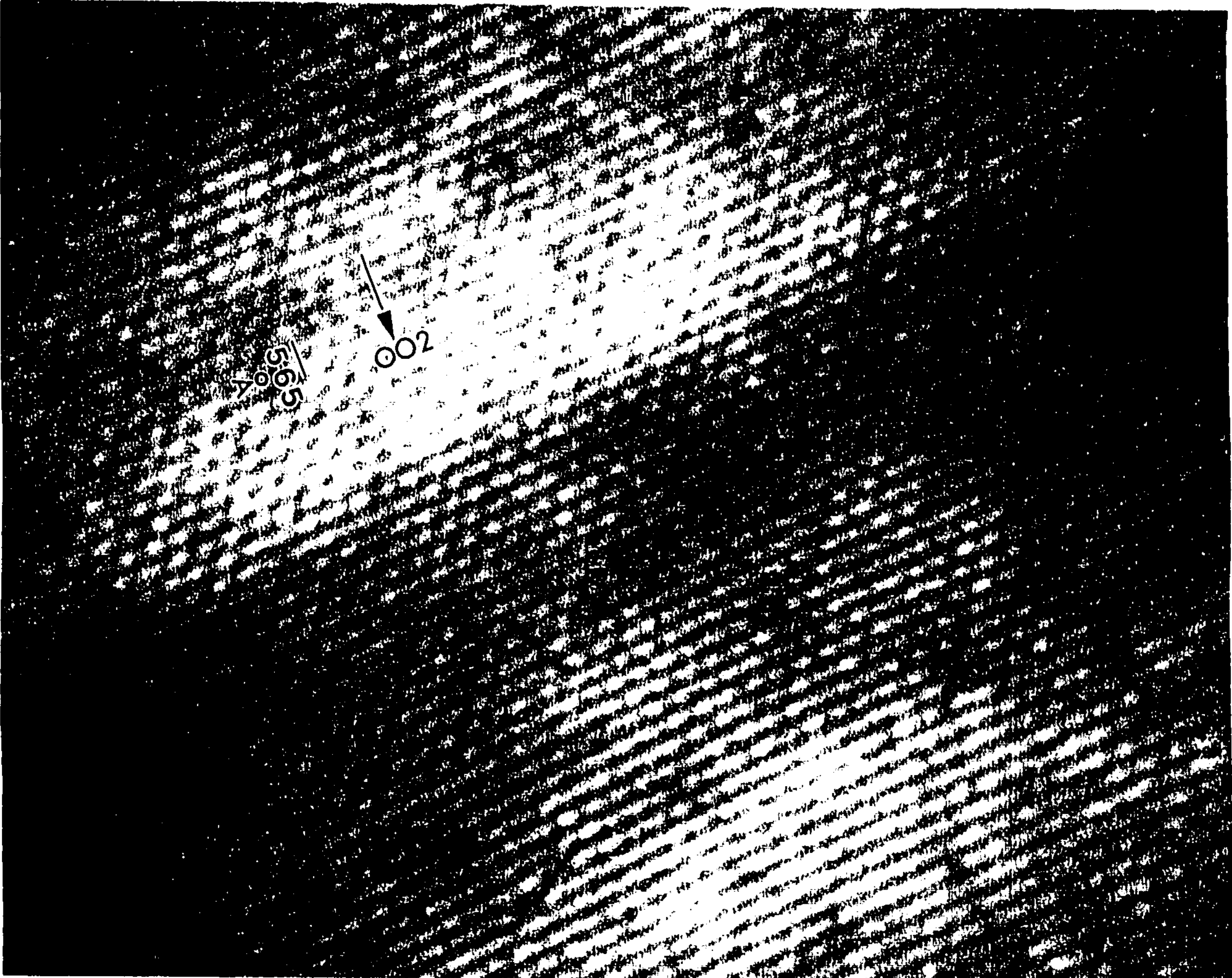

Fig 4.10 .1 Lower GaAs quantum well in A1 structure, R.T.A. only.

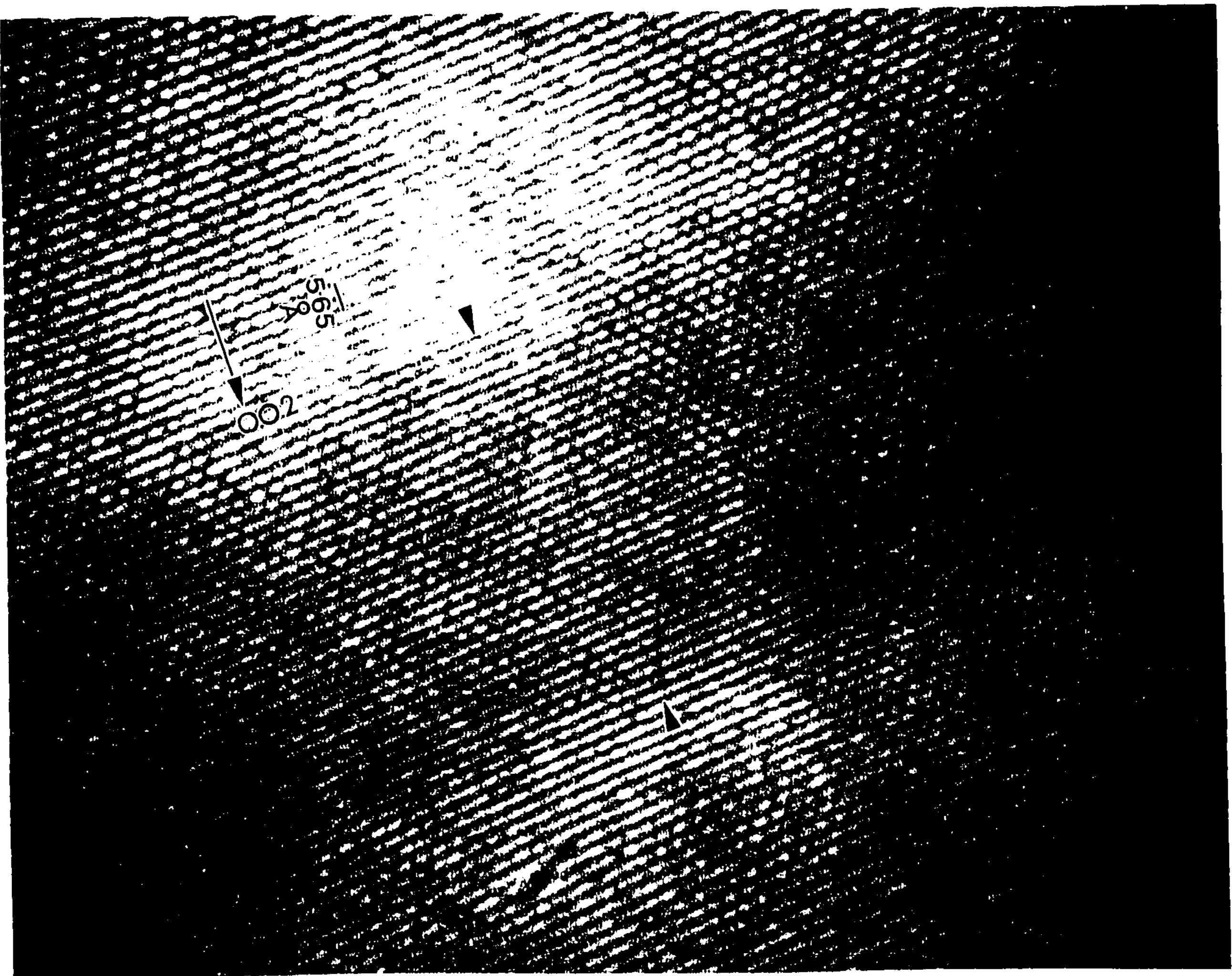

Fig 4.10.2 Lower GaAs quantum well in A1 structure. As^+ 8.0 MeV implant ,105 second R.T.A. at 850 ^{0} C

portions of the same sample implanted at 8 MeV. The well thickness increase following different treatments were obtained from such micrographs. The thickness of the GaAs wells were measured using the image processing software Digital Micrograph [53]. This software enables calibration of known distances on the micrograph, e.g. the (002) lattice spacing of GaAs. With such a calibration it is possible to measure the thickness of the quantum well at several locations. While the periphery of the well in the implanted and annealed structure is diffuse, an upper bound estimate of the well thickness is still possible. The extremities of the GaAs quantum well in the 8 MeV implanted and annealed A1 sample are marked in Fig 4.10.2.

4.2.2. (A2) structures.

As already pointed out above, these structures had $Al_{0.2}Ga_{0.8}As$ barriers and GaAs quantum wells. No planarization layers were grown in the lower cladding. The depth of the quantum wells was once again 1.8μm below the surface of the sample. The implanted and RTA portion of the 6 MeV As^+ implanted sample is seen in Fig 4.11. The contrast from the GaAs quantum wells is very weak because of the small structure factor difference between the well and its barrier. Following implantation with As^+ at 6 MeV and rapid thermally annealing at 850^0C for a total of 105 seconds dislocation loops were again found below the quantum wells. However in this structure the position of the dislocation loops is random and shows no specific spatial preference. The loops

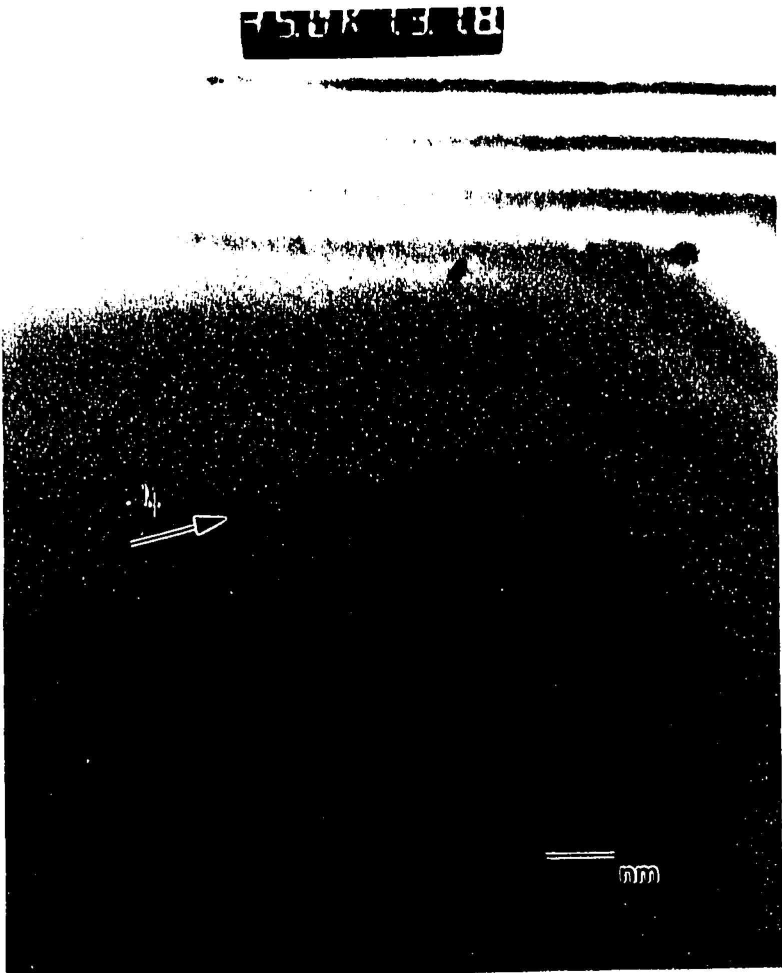

Fig 4.11 Implant and R.T.A. portion of sample A2 implanted with As^+ at 6 MeV. g = $(2\bar{2}0)$

again were found to exhibit very little strain contrast when the (002) reciprocal lattice vector was diffracting.

4.2.3. AlGaAs/GaAs/InGaAs based structures (I1, I2)

As was documented in Chapter 3, two kinds of structures were once again examined. The first **(I1)** was a graded index, separate confinement structure consisting of AlGaAs cladding 1.8μm thick, graded in composition from 20% to 70% Al. The separate confinement portion of the heterostructure consists of two $In_{0.21}Ga_{0.79}As$ quantum wells 60 $\mathring{A}$ thick separated by GaAs barriers. In this structure (as in the case of A1) planarizing GaAs layers were grown in the lower graded AlGaAs cladding. The trends seen in the photoluminescence when this structure was implanted with As^{+} at a dose of ($2.5*10^{13}$ /cm^2, T= 200^{0}C) at energies ranging from 1 to 8 MeV is reproduced from the data provided by the NRC group in Fig 4.12, [52]. The samples were annealed at 850^0 C for 90 seconds. An increasing blue shift of luminescence with increasing implantation energy is once again clearly discerned. A curious feature is seen in the case of the 5 MeV implanted sample where a double peak in the PL is obtained.

In order to probe the origin of this double peak a careful examination of this particular sample was undertaken. Fig 4.14 displays some of the features which were observed in this sample. An examination of the implanted region of the sample clearly

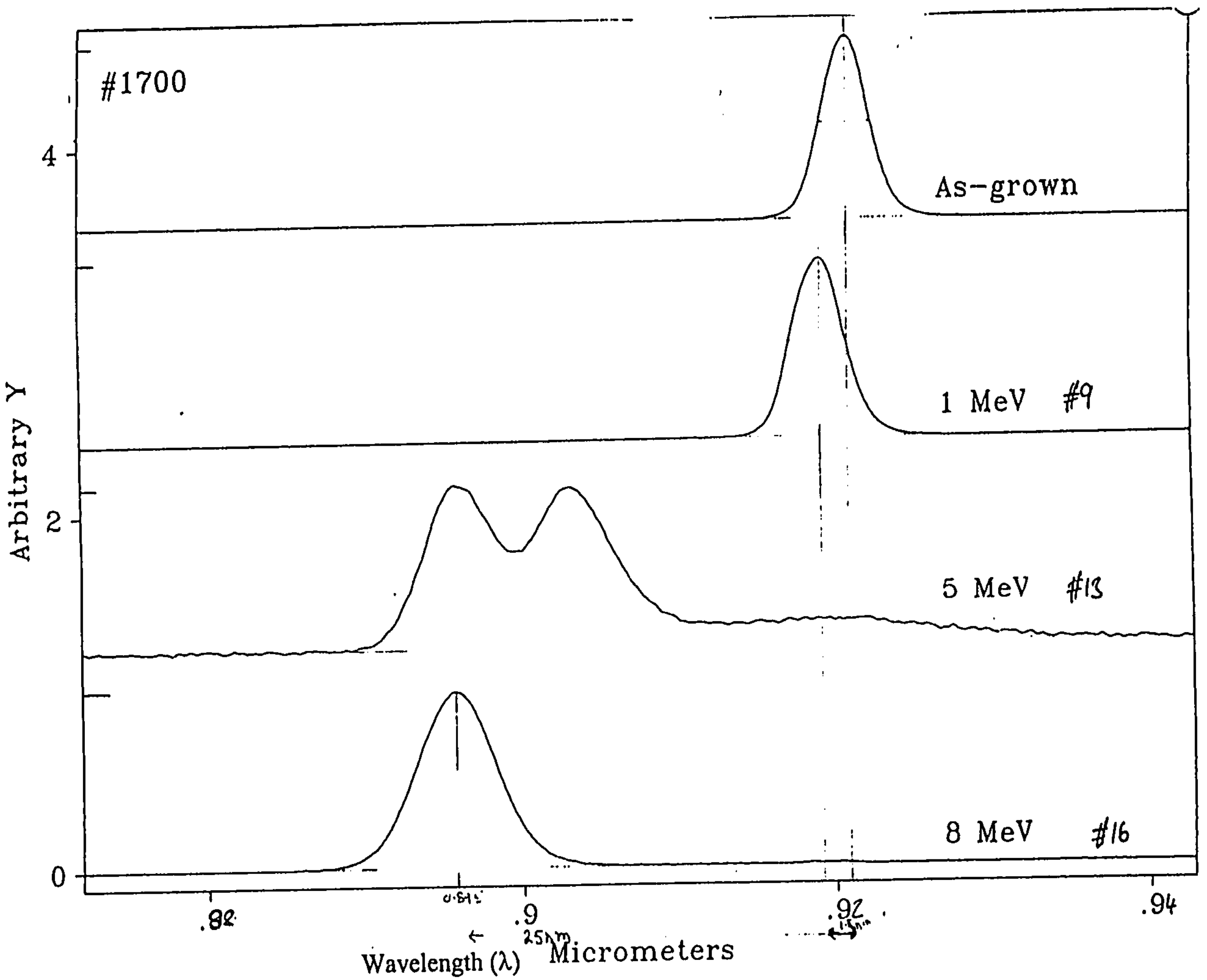

PP250763

BOMEM Michelson FTIR

Fig 4.12 Evolution of the PL from I1 structures as a function of implant energy.

showed substantial broadening of the wells. The range of the ions for this implantation energy as predicted by TRIM simulation is ~ 2.3 μm about 0.5 μm below the quantum wells. It was found that the wells have increased in thickness from 62 Å ± 3 Å to 100 Å ± 3 Å on implantation and rapid thermal annealing at 850^0C for a total of 90 seconds. No significant thickness differences between the two wells could be obtained within the resolution (~ 3 Å) of this determination. In this particular sample and in other samples of the same kind, the $(1\bar{1}1)$ diffraction spot was split. On dark field imaging using this split diffraction spot the sample subjected to RTA exhibited pronounced fringes, which are seen in Fig 4.14(d). As was already noted in the case of the AlGaAs/GaAs based structures, loops in this sample also tended to accumulate at the GaAs planarization layers in the graded cladding. These loops were once again interstitial in character with $[\bar{1}10]$ Burgers vectors.

Some samples in this set were implanted at low temperature (77K) while some others were implanted at room temperature. Fig 4.15 shows a comparison between the low temperature (77K) implanted sample and the room temperature(300K) implanted sample. Both samples were implanted at 7 MeV. The ion range at this energy as calculated (from TRIM) is ~ 2.84 μm, about a micron below the quantum well. Clearly in the case of the low temperature implant (77K) clustering of dislocation loops in the vicinity of the quantum wells and (seen somewhat more faintly) at the planarization layers takes place. This clustering of defects in the vicinity of the well is obviously

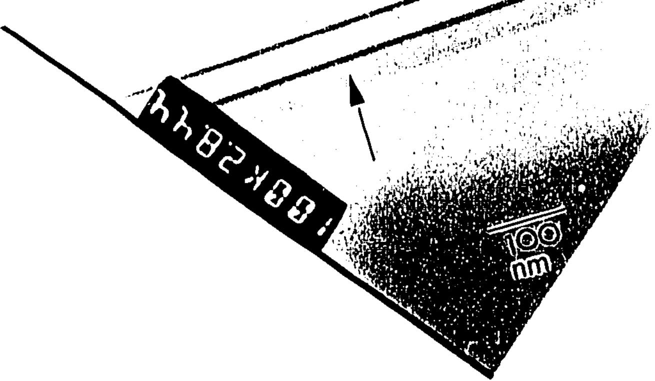

Fig 4.14(a) R.T.A. only portion of sample II. **g** = (002).

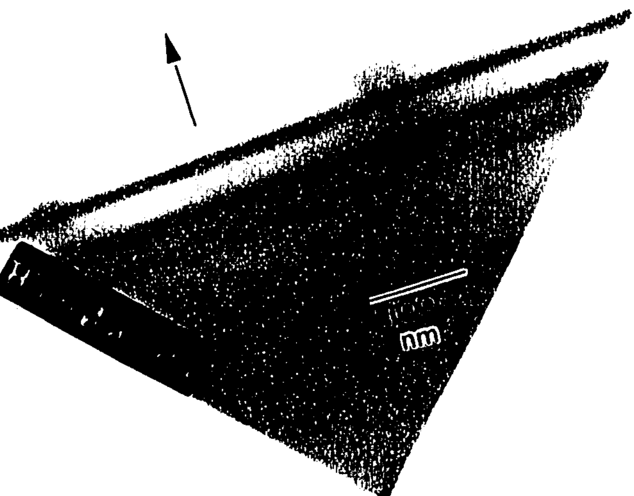

Fig 4.14(b) Implanted with As^+ at 5 MeV and R.T.A at 850 ^{0} C for 90 seconds. **g** = (002).

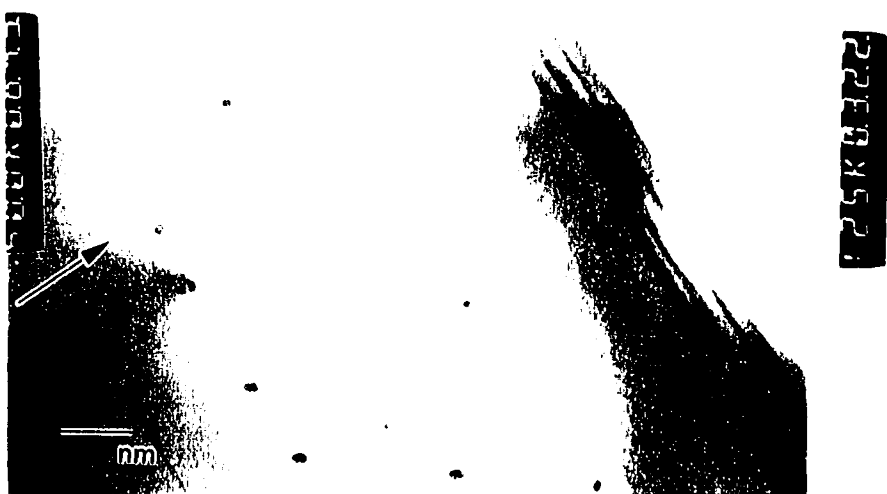

Fig 4.14(c) Clustering of implant damage on GaAs planarization layers in I1. **g**= (004).

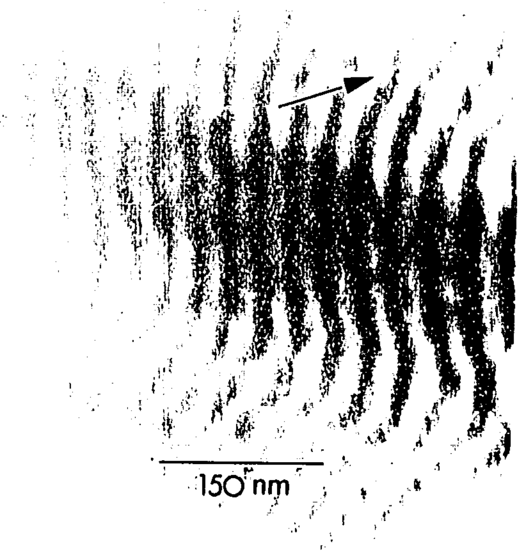

Fig 4.14(d) Fringes seen in dark field **g** = $(1\bar{1}1)$ image from 5 MeV As^+ implanted I1 sample, probably arising from composition modulations

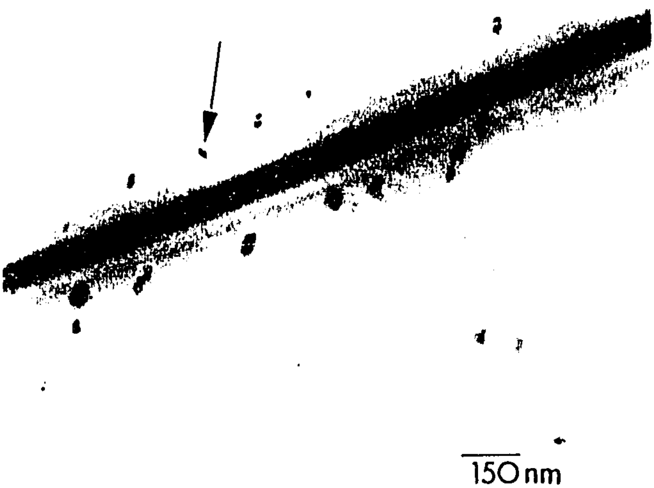

Fig 4.15.1 7 MeV As^+ implanted II sample (77K). R.T.A. at 850 ^{0}C for 90 seconds. $\mathbf{g} = (\bar{2}\,2\bar{2})$.

Fig 4.15.2 7 MeV As^+ implanted II sample (300K). R.T.A. at 850 ^{0}C for 90 seconds. $\mathbf{g} = (02\bar{2})$.

absent in the case of the room temperature implanted sample, although a tendency of the loops to be located on the planarization layers can still be seen. The blue shift in the case of the 77K implanted sample was 63 meV as compared to the room temperature implanted sample which exhibited a blue shift of 39 meV.

Finally in the micrographs shown in Fig 4.16 a comparison is made of dislocation loops in doped and in undoped samples with the same geometry implanted with As^+ at 1 MeV and rapid thermally annealed at 850^0 C for a total of 90 seconds. In the undoped sample dislocation loops are found even at a depth ~ 0.4 μm below the wells, while in the doped sample only the occasional loop could be found at the depth of the well. The NRC group [52] found experimentally that the blue shift in the PL was ~ 0.5 nm in the case of the doped structure while it was ~ 2 nm for the undoped structure.

4.2.4. I2 structures.

In these structures the cladding layers were GaAs and no planarization layers were grown. Two $In_{0.23}Ga_{0.77}As$ 60 $\overset{0}{A}$, quantum wells were grown with 1.7μm of GaAs cladding. Fig 4.17 presents micrographs from a 1.1 MeV (micrograph (a)) and 8 MeV (micrograph (b)) implanted sample. The tendency of loops to be found at the well in the 1.1 MeV implanted sample, and the random location of the loops when no planarization layers are grown (8 MeV implantation) is once again observed, as in the case of all previous structures. The loops were once again interstitial with $[\bar{1}10]$ Burgers vector.

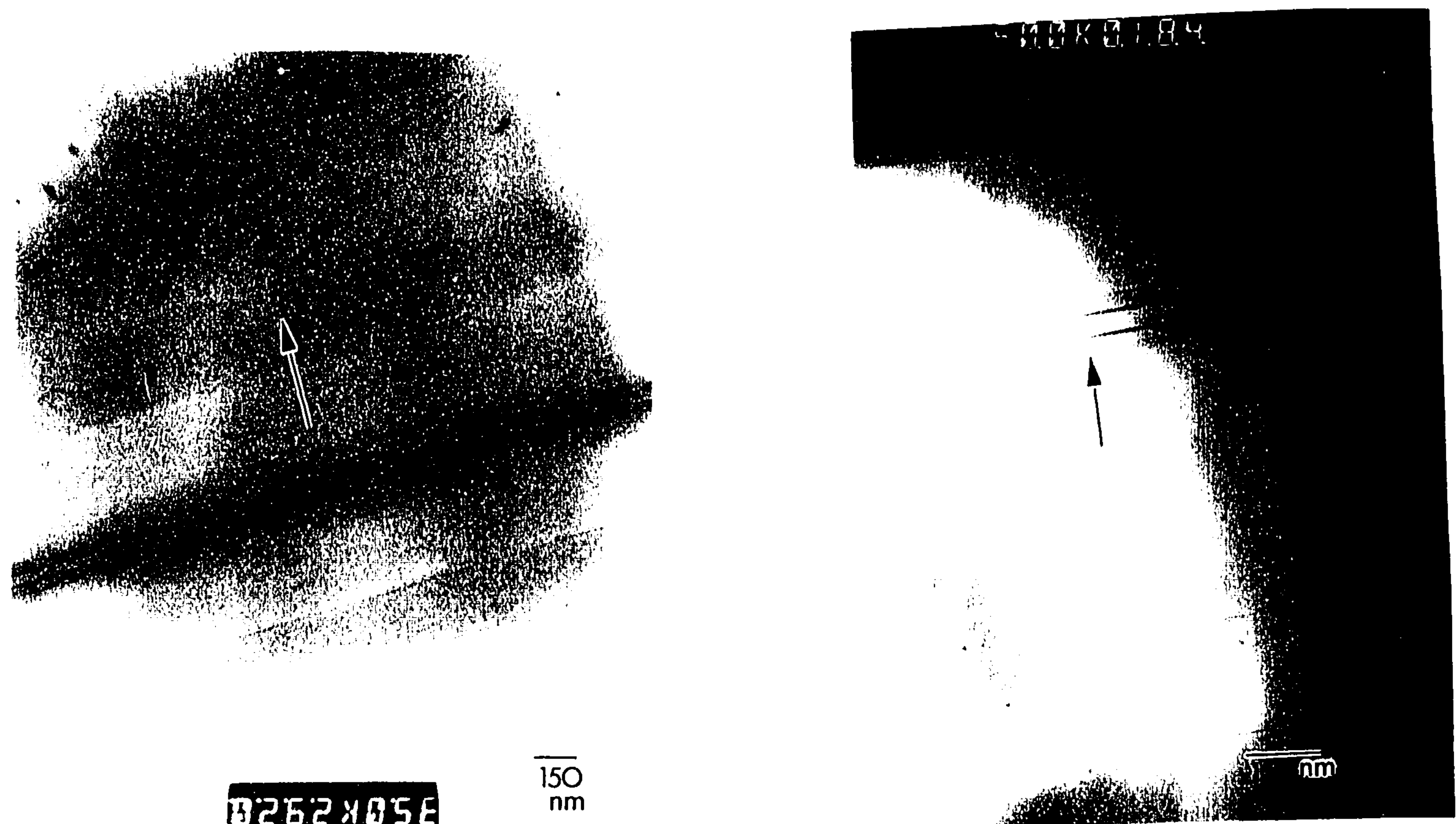

Fig 4.16.1 Doped II sample imaged near [110] zone axis. As^+ implanted at 1.0 MeV. **g** = (002)

Fig 4.16.2 Undoped II sample . As^+ implanted at 1.0 MeV. **g** = (002)

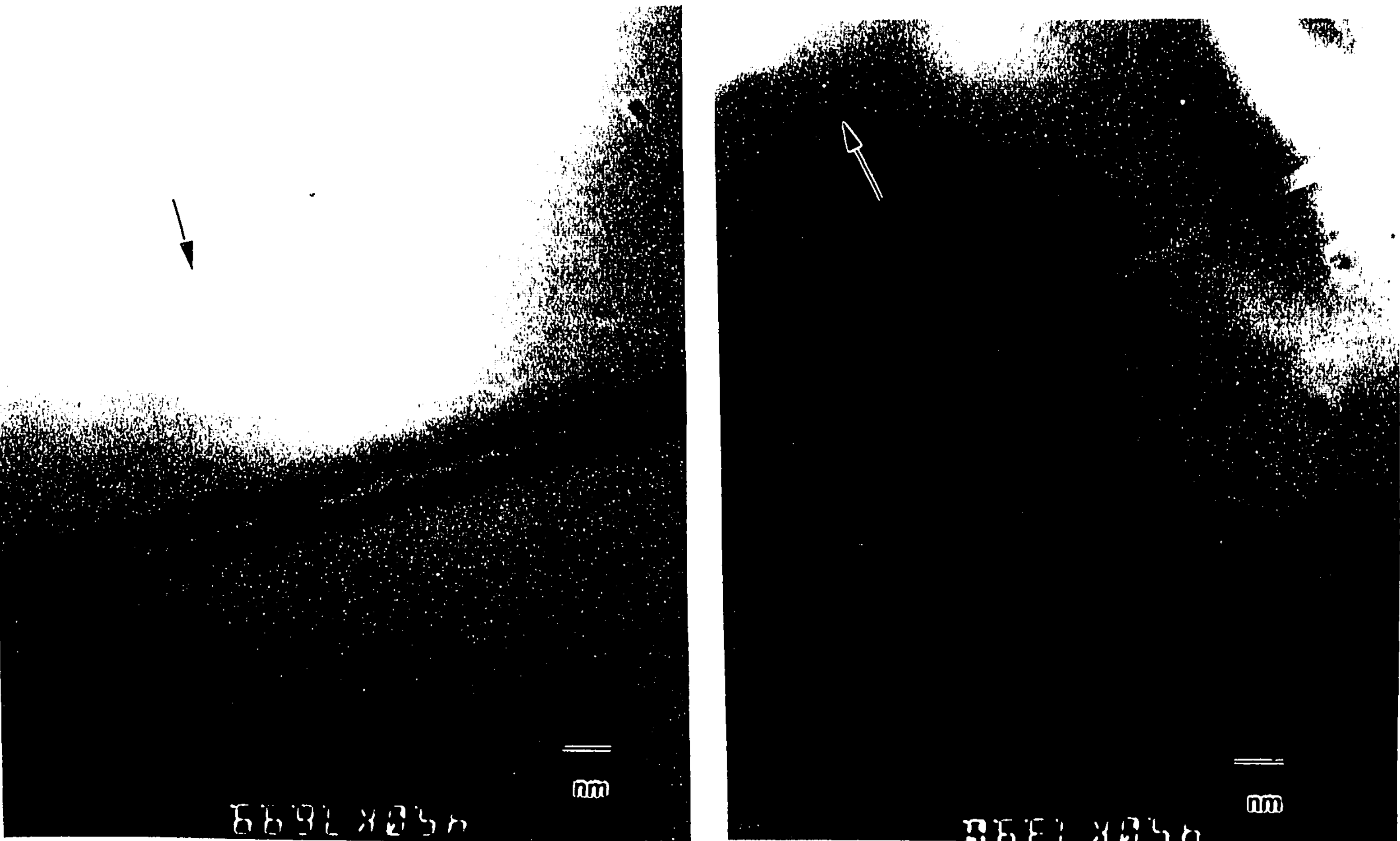

Fig 4.17 (a) 1.1 MeV As^+ implanted I2 sample. **g** = (0 0 $\bar{4}$).

Fig 4.17 (b) 8 MeV As^+ implanted I2 sample. **g** = (0 0 4).

4.2.5. SD structure implantation. Finally implantation studies were also undertaken on (SD) structures. The configuration of these structures was described in section 4.1.4. The purpose of these experiments was to determine the influence of the dose on the PL blue shift. All implants were conducted at 300 keV in the Tandetron accelerator at UWO. The beam dose examined ranged from $5*10^{11}$ to $5*10^{13}$ /cm^2. Implants were conducted with both Ga^+ and As^+. Beam current densities were of the order of 10 nanoampere/ cm^2. All implants were done at room temperature (300 K). Following implantation the samples were rapid thermally annealed at 850^0 C for a total of 30 seconds. The results of PL on these samples is summarized in Table 4.3. Although an increasing dose is marked by a concomitant increase in the PL shift in the range ($5*10^{11}$ - $5*10^{12}$ / cm^2) there appears to be a limit to this positive correlation. At a dose of $5*10^{13}$ /cm ^{2} there is no recovery of luminescence after 30 seconds annealing. The trends seen for both the Ga^+ implantation and for the As^+ implantation are qualitatively the same in terms of the dose dependence of the PL shift.

Table 4.3. Blue shift of SD type samples with implant dose.

sample	unimplanted	implanted				
	peak position	peak position	shift	shift (meV)	species	Dose / cm^2
	(nm)	(nm)	(nm)			
SD10	867.2	860.2	− 7.1	11.8	As^+	5.00E+11
SD10	867.3	858.1	− 9.2	15.4	As^+	5.00E+12
SD10	867.7	no sig			As^+	5.00E+13
SD10	866.7	860.0	− 6.7	11.1	Ga^+	5.00E+11
SD10	867.7	861.7	− 6.0	9.9	Ga^+	5.00E+12
SD10	868.4	nosig			Ga^+	5.00E+13
SD15	905.4	898.4	− 7.0	10.7	As^+	5.00E+11
SD15	905.4	894.3	−11.2	17.1	As^+	5.00E+12
SD15	904.2	nosig			As^+	5.00E+13
SD15	905.7	896.3	− 9.4	14.4	Ga^+	5.00E+11
SD15	909.9	895.2	−14.6	22.4	Ga^+	5.00E+12
SD15	904.2	no sig			Ga^+	5.00E+13
SD20	916.0	908.5	− 7.5	11.2	As^+	5.00E+11
SD20	923.6	906.5	−17.1	25.4	As^+	5.00E+12
SD20	919.8	nosig			As^+	5.00E+13
SD20	917.6	907.3	− 10.3	15.4	Ga^+	5.00E+11
SD20	917.7	904.6	− 13.1	19.7	Ga^+	5.00E+12
SD20		no sig			Ga^+	5.00E+13

Chapter 5.

DISCUSSION

In this chapter a rationalization of the experimental data from the long term diffusion experiments of the superlattice structures (SL10) is provided. In doing so a linear model of diffusion has been utilized. Support for the assumptions of a weak composition and strain dependence of the diffusion coefficient (assumed in a linear model) is derived from an analysis of experimental results on the SD structures and the 100S3 and 311S3 structures. This rationalization is founded on the fact that theoretically calculated photoluminescence trends agree with the experimentally observed trends in the photoluminescence (PL) data.

The discussion is organized as follows. In the first half of this chapter a numerical model for the interdiffusion of the superlattice structure(SL10) is developed. The composition profiles so obtained are used to calculate the PL transition wavelengths and X-Ray diffraction profiles. It is shown that the model can explain the experimental results. Parameters which are required for the simulation were obtained from analysis of diffusion experiments conducted on the single and double well (SD) structures. It is further shown that the trends seen in the PL from the SD structures are also in agreement with the same model.

The latter half of this chapter is concerned with a discussion of the features observed in the ion implanted samples. A model of the ion implantation enhanced interdiffusion process is developed by numerically solving coupled diffusion equations for the vacancy and interstitial evolution, as well as the quantum well interdiffusion. A rationalization of the trends seen in the A1, A2, I1 and I2 structures is then provided.

5.1. Linear model for superlattice homogenization.

As was noted in the chapter on the experimental results (Chapter 4) interdiffusion of the SL10 superlattice structure was characterized by a red shift of the photoluminescence at short anneal times of 20 minutes which gradually decreased with increasing annealing times until 6 hours. At an anneal time of 12 hours ultimately the PL peak was blue shifted relative to the as grown peak. In rationalizing these experimental results it is necessary to calculate the composition evolution with annealing time. Once a composition profile has been calculated the corresponding strain in the structure can be evaluated. Knowledge of the composition and the strain is necessary in order to evaluate the confining potential for the both the electrons and the holes.

In order to calculate the composition evolution of the superlattice an integral solution of the diffusion equation has been adopted [54]. In this linear approximation the concentration dependence of the diffusion coefficient is neglected and the composition

evolution is computed by convolution of the initial concentration profile with a Gaussian point spread function. For the initial concentration profile we assume that the well-barrier interfaces are sharp and the concentration profile can be described by a rectangular wave. The Gaussian point spread function is the diffusion profile for a Dirac delta function shaped initial concentration profile.

If at t=0 the concentration profile is

$$c(x, 0) = \delta(x) \qquad ..5.1$$

then at time t the concentration profile c(x, t) goes to

$$c(x, t) = (e^{-x^2/4Dt}) / \sqrt{4\pi Dt} \qquad ..5.2$$

Since we are dealing with interdiffusion on the group III lattice the concentration c is the concentration profile of indium in the InGaAs/GaAs superlattice structure (SL10). In the above expressions D is the In-Ga interdiffusion coefficient. Equation (5.2) is the point spread function that convolutes the initial concentration profile. The initial concentration profile for the superlattice is a rectangular wave which is given as

$$c(x, t=0) = C_o \sum_{n=0}^{n=m-1} rect(x, nd) \qquad ..5.3$$

where $\quad rect(x, c) = 1 \quad$ for $\quad |x - c| \leq L$

$= 0$ otherwise.

In equation 5.3,

2L = thickness of the quantum well

C_o = is the initial amplitude of the concentration profile.

d = is the superlattice period.

m = number of wells in the superlattice.

A convolution of the initial concentration profile (5.3) with the point spread function (5.2) can be carried out to yield

$$c(x, t) = C_o/2 \sum_{n=0}^{n=m-1} erf[((x-nd)+L)/2\sqrt{Dt}] + erf[(L-(x-nd))/2\sqrt{Dt}]$$

.. 5.4(a)

where erf is the error function

$$\mathrm{erf}(x) = 2/\sqrt{\pi} \int_0^x e^{-t^2} dt$$

..5.4 (b)

The sequence of composition evolution with time for the case of the superlattice structure (SL10) considered in the experimental section(chapter 3) computed according to (5.4(a)) is depicted in Fig (5.1). As can clearly be seen, a initial square wave modulation adopts a sinusoidal form as time increases. A concentration independent diffusion coefficient of 10^{-18} cm^2/s at 850^0 C is assumed for these calculations. This interdiffusion coefficient was derived by measuring the thickness increase of the single

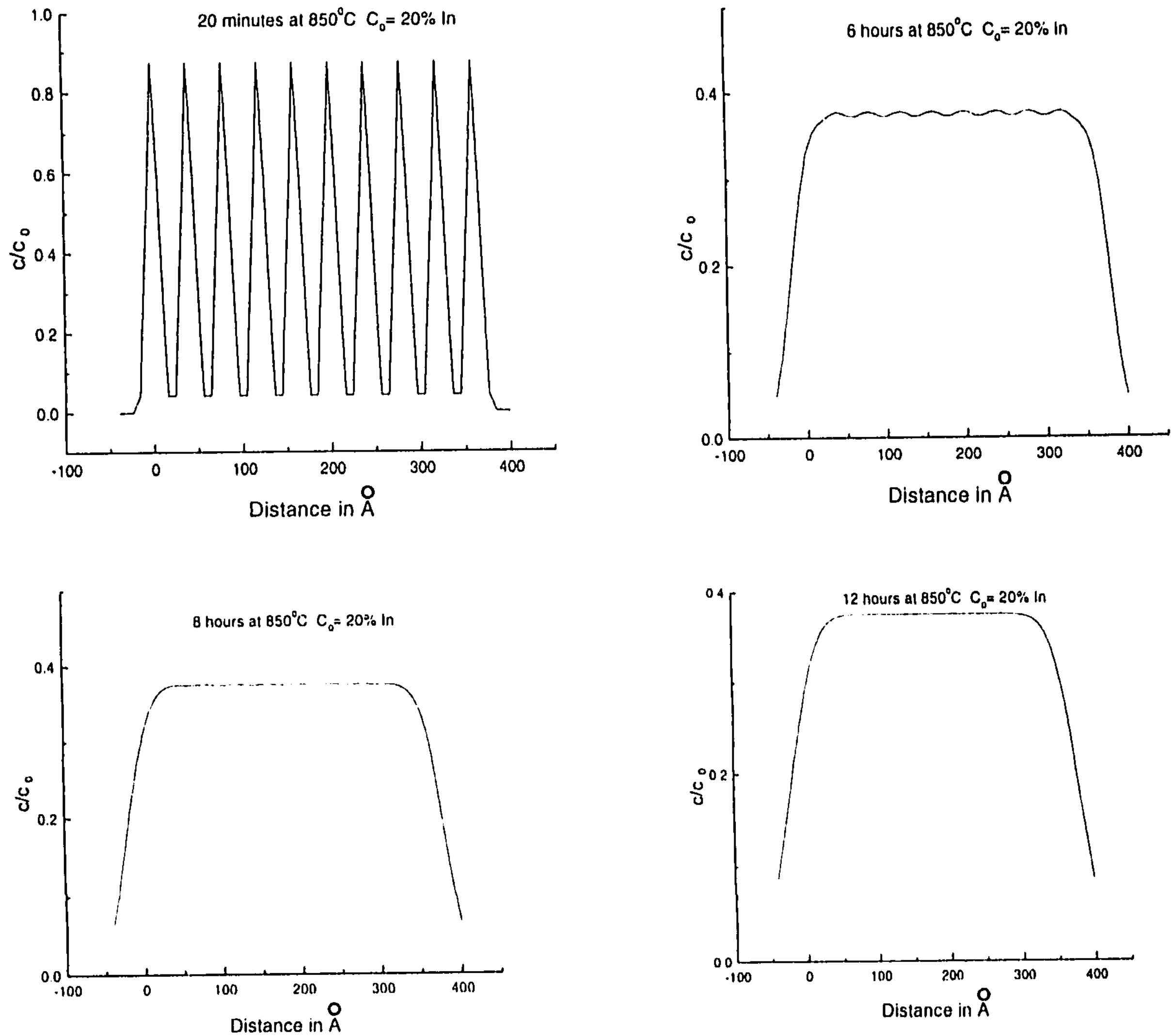

Fig 5.1 Evolution of the concentration of the SL10 superlattice computed in a linear diffusion approximation.

quantum well in the SD20 sample annealed for 8 hours at 850^0 C. The thickness increase was then equated to $4\sqrt{Dt}$. As can be seen the calculated temporal evolution of the structure is in qualitative agreement with the TEM micrographs provided in Fig (4.1) in Chapter 4.

5.1.2 Computation of strain in the superlattice.

Having obtained the temporal evolution of the composition we can then proceed to compute the evolution of the strain in the structure. The method that has been adopted to compute the strain in the structure is due to Nakajima [55].

In calculating the strain in such a compositionally graded structure Nakajima et al. proceed by dividing the structure into a number of elementary segments. At equilibrium the net force and the net moment on the structure have to be equal to zero. Equilibrium equations for the face force and moment on each of these segments can be derived. These equations account for the continuity of the displacement at the inter segment interfaces. The computed face forces and the moments enable calculation of the strains in each elementary segment. There are both in plane compressive strains and growth direction tensile strains (due to Poisson relaxation) in the structure. These strains determine the potential that the charge carriers see and a knowledge of their magnitude is therefore necessary for computation of the PL transition energies.

5.1.3. Computation of X-ray diffraction from the as grown and annealed structures.

The composition modulation determines the atomic scattering factor modulation that the structure presents to the probing X-rays. The strain in the structure determines the lattice parameter modulation. With a knowledge of the variation of these parameters as a function of depth in the sample, a kinematic estimate of the X-ray diffraction from the structure can be obtained.

In the kinematic approximation, X-Ray diffraction from a compositionally modulated structure is obtained by Fourier transforming the atomic scattering modulation. The amplitude of X -Ray diffraction in the kinematical approximation is given as

$$U = \sum_{n=1}^{n=k} F(n) e^{2\pi i \varphi_n / \lambda} \qquad ..5.5$$

where n is an atom plane number.

F(n) is the atomic scattering factor

φ_n is the path difference

λ is the wavelength of the X- rays.

Both the atomic scattering factor F(n) and the path difference φ_n are dependent on the angle of incidence of the X-Rays (θ).

The atomic scattering factor dependence on θ is calculated for the InGaAs/GaAs structure following the parameters provided in [56]. The path difference φ_n is obtained from the following equation:

$$\varphi_n = \sum_{i=1}^{i=n} 2d_i \sin(\theta) \qquad ..5.6$$

d_i is the spacing between planes i and i+1

For a compositionally modulated structure such as an $In_{1-x}Ga_xAs$ superlattice, diffraction from (004) planes (assuming the growth direction is [001]) will be characterized by an atomic scattering factor F given by

$F= 2(x\, f_{ga} + (1-x)\, f_{In})$ for group III constituted planes

$F= 2\, f_{As}$ for As constituted planes.

The strain in the structure and the consequent lattice parameter modulation is captured in the φ_n terms. The intensity of X-ray diffraction is the associated power spectrum of the amplitude U.

$$I = UU^* \qquad ..5.7$$

An implementation of the above scheme for the as grown SL10 structure results in the spectrum shown in Fig (5.2). The Bragg peak due to the substrate, the average superlattice peak and the first order satellites on either side of the average superlattice

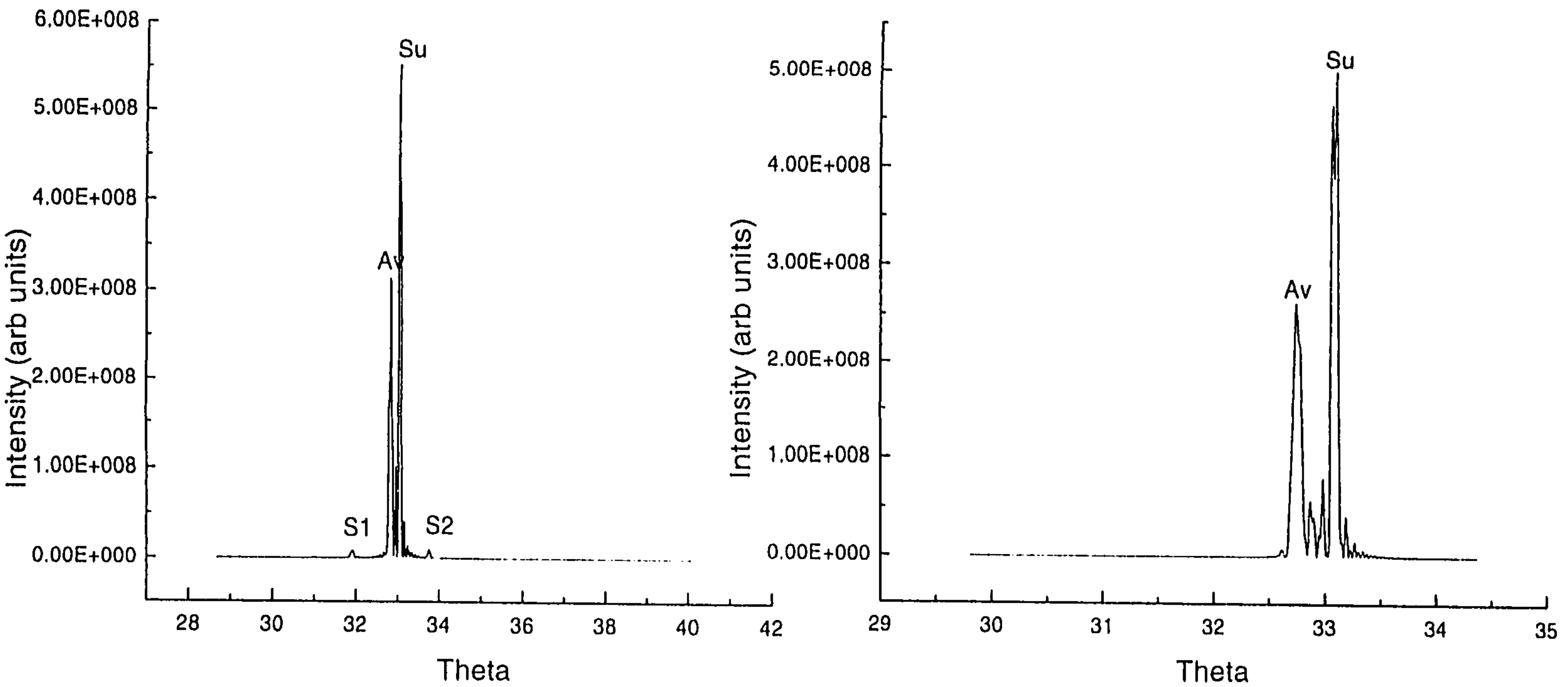

Fig 5.2 Computed X-ray diffraction from as grown SL10 superlattice.

Fig 5.3 X-ray profile from 8 hours annealed SL10 superlattice.

peak are easily discerned. The positions of these peaks are also in good agreement with the experimental values in Chapter 4 and the theoretical values calculated by Greer et al. [57]. Fig (5.3) presents the results of a similar calculation, for the (SL10) structure annealed for 8 hours. The disappearance of the satellite peaks in the calculated spectrum is once again in qualitative agreement with the experimental spectrum for the 8 hours annealed SL10 structure Fig (4.2).

5.1.4. Computation of the photoluminescent transition wavelengths.

Thus far the results of the linear diffusion model have only been in qualitative agreement with both the TEM and X-ray diffraction data. Validity of the linear diffusion model would however require consonance with the trends seen in the photoluminescence from the annealed SL10 structures.

In calculating the photoluminescent wavelength, it is necessary to evaluate the hole and the electron confinement energies for the potential presented by the composition and strain in the as grown and annealed structures. The key problem in evaluating the potential seen by the electrons and the holes is the computation of the band offset.

The band off-set in this work has been computed following the approach of Van De Walle [58]. In the model solid solution of Van De Walle , the band off-set dependence on both the composition and strain is considered. Two distinct steps are involved in the model solid theory. In the first step the band structure of the material is calculated

following first principles quantum mechanical calculations. The second step is to align the band structure so calculated on an absolute energy scale. Van De Walle discuss the choice of such an energy scale and also provide values for the energy positions of the valence and conduction band edges for a number of semiconducting materials.

The effect of strain on the valence and conduction band edges is then incorporated through an appropriate deformation potential, which acts to shift the valence and the conduction band edges in accordance with the strain imposed on the material. Van De Walle then proceeds to show how this scheme may be used to compute band alignments by simple subtraction of the appropriate parameters for the semiconducting materials constituting the heterostructure. The agreement with experimental data is good for heterostructures derived from III-V compound semiconductors.

5.1.5. The transfer matrix technique.

Once the calculation of the band offset has been accomplished, an evaluation of the confinement energy of electrons and the holes is achieved by solution of the time independent, one dimensional Schrödinger wave equation.

$$[\hbar^2/2m^* (\partial^2/\partial x^2) + V(x)]\ \psi = E\ \psi \qquad ..5.8$$

The symbols have their usual meaning

V(x) is the confining potential.

E is the eigen energy

ψ is the wavefunction.

m^* is the effective mass of the charge carrier.

Since the composition during diffusion continuously evolves and with it the strain and consequently the potential, a numerical transfer matrix technique following Ghatak et al. [59] is utilized to evaluate the eigen values from 5.8.

In this technique the confining potential is divided into a number of elementary segments and the amplitude of the wavefunction in one segment is related to the amplitude in the next segment via a transfer matrix which depends upon the wavevectors in the two segments. If a solution to equation (5.8) in segment i of the form

$$\psi_i = u_i^+ e^{-i\Delta_i} e^{ik_i x} + u_i^- e^{i\Delta_i} e^{-ik_i x} \qquad ..5.9$$

be considered, continuity of the wavefunction and the first derivative of the wavefunction (scaled with $1/m^*$) at inter segment interfaces results in the following transfer matrix relating the amplitudes

$[u_i^+ u_i^-]$ and $[u_{i+1}^+ u_{i+1}^-]$:

$$\begin{bmatrix} u_i^+ \\ u_i^- \end{bmatrix} = S_i \begin{bmatrix} u_{i+1}^+ \\ u_{i+1}^- \end{bmatrix} \qquad ..5.10$$

with

$$S_i = \begin{bmatrix} s_{11} & s_{12} \\ s_{21} & s_{22} \end{bmatrix}$$

$s_{11} = e^{-i\delta_i} / t_i \qquad s_{12} = r_i e^{-i\delta_i} / t_i$

$s_{21} = r_i e^{i\delta_i} / t_i \qquad s_{22} = e^{i\delta_i} / t_i$ ..5.11

k_i is the wave vector in the i'th segment.

d_i is the thickness of the i'th segment.

δ_i is $k_i d_i$

$t_i = 2k_i / (k_i + k_{i+1})$ and $r_i = (k_i - k_{i+1}) / (k_i + k_{i+1})$ ..5.12

The wavevectors k_i, k_{i+1} can be evaluated given a dispersion relationship between energy E and k. The dispersion relation suggested by Chaung et al. [60] is adopted to calculate the wavevector k for a given energy. Winter et al. [61], Ghatak et al. [59] show that if an energy E is a bound state energy corresponding to a certain potential profile containing n blocks (as defined earlier) $|u_n^+ / u_1^+|^2$ would show a resonance peak.

In calculating the bound state energies, the energy is allowed to vary from the deepest well in the structure to the level of the barrier. This deepest point is obtained from the band offset calculation. The successive transfer matrices S_1, S_2.. S_n are then evaluated as the dispersion relation is known. When the amplitude ratio $|u_n^+ / u_1^+|^2$ shows a

peak a bound state is detected. Similar considerations apply for the electrons and the holes, although the potentials to be considered are different. Amplitude ratios corresponding to the nominal well centers can be evaluated in the original superlattice structure to obtain the bound states; corresponding positions in the annealed structure are obtained to evaluate how these vary as a function of annealing.

Table 5.1 compiles the calculated bound state energies for the n=1 and n=2 levels for both the electrons and the holes as a function of annealing time. As can clearly be seen, as the structure anneals and the wells homogenize, the bound state energy rapidly falls and basically becomes negligible in the long term diffused structures. By computing the PL transition wavelengths the initial red shift and the subsequent blue shift in luminescence is replicated as in the experiments. Fig (5.4) is an example of the three resonances obtained for the case of electron energies in the case of a structure diffused for 6 hours.

The probable explanation for the behavior of the PL wavelengths is related to the falling confinement energy with increasing annealing time, and the rising nominal band gap value due to the diffusion of gallium into the heterostructure or equivalently indium diffusion out of the wells. The fall in the confinement energy would tend to red shift the luminescence, while diffusion of gallium would tend to blue shift the luminescence. Given the small periodicity of the initial heterostructure and consequently rapid thickening after small anneal times an initial redshift is discerned. The subsequent

Table 5.1. Results of the transfer matrix calculation for the transition wavelength, on annealing superlattice SL10 for varying periods of time.

Time	Electron Energy (eV)	Hole energy (eV)	Transition wavelength (nm)
		n =1	
As Grown	0.055	0.107	885.8
20 min	0.027	0.05	908.5
6 hours	0.011	0.021	888.7
12 hours	0.009	0.021	884.9
		n =2	
As Grown	0.058	0.115	878.8
20 min	0.029	0.067	896.4
6 hours	0.016	0.025	883.6
12 hours	0.012	0.034	875.5

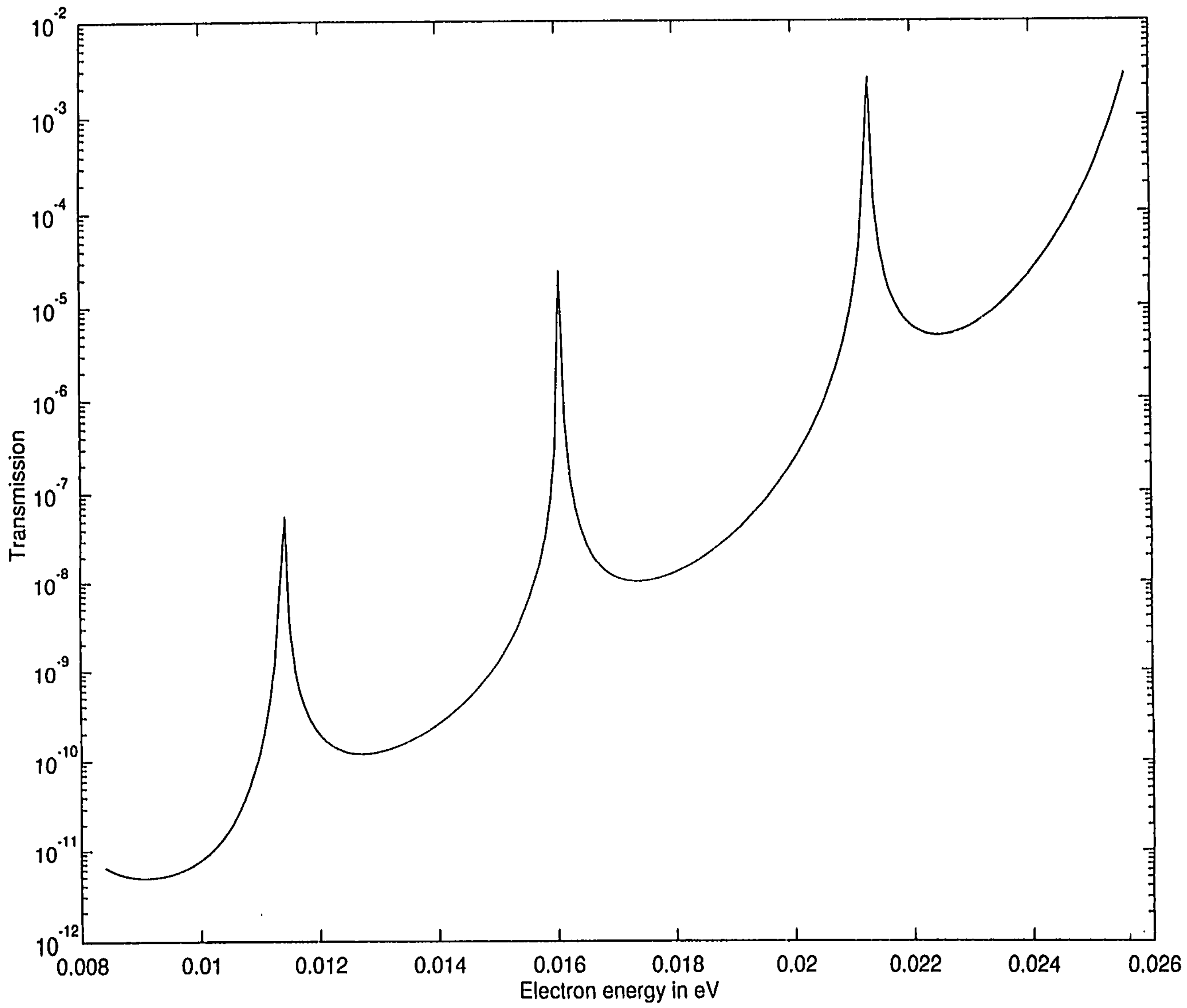

Fig 5.4 Results of the transfer matrix calculation for the energy of the electron in in the SL10 structure annealed for 6 hours.

gallium diffusion blue shifts the luminescence back across the luminescence of the as grown structure.

5.1.6. Discussion of the trends seen in the SD structures.

A linear model of diffusion appears to be capable of explaining the trends seen in the annealing of the SL10 superlattice structure. This necessitates examination of both the composition dependence and the strain dependence of the interdiffusion coefficient. If a linear model is adequate, both the composition dependence and the strain dependence should be small.

A preliminary examination of blue shift data from the single quantum well of the SD structures seems however to indicate otherwise. In Table 4.1 (Chapter 4) values for the blue shift of the nominally 10%, 15% and 20% InGaAs quantum wells after varying heat treatments were tabulated. Clearly an increasing blue shift with increasing In content was discerned.

However an increasing blue shift of the luminescence with increasing In content is not necessarily indicative of a strong composition dependence of the diffusion coefficient as the following argument shows. An initially rectangular well given as:

$$c(x, t=0) = C_o \, \mathrm{rect}(x, 0) \qquad ..5.13$$

$$= (C_o \text{ for } |x| \le L \quad \text{with the well thickness } 2L \text{ , } 0 \text{ otherwise })$$

would on interdiffusion for a period t in a linear approximation evolve into

$$c(x, t) = C_o/2[\,\mathrm{erf}((x+L)/2\sqrt{Dt}) + \mathrm{erf}((L-x)/2\sqrt{Dt})\,] \qquad ..5.14$$

where as before erf is the error function and

D is the interdiffusion coefficient for In-Ga or Al-Ga.

It is clear from the above expression that the concentration at any point x would scale with the initial amplitude of the rectangular profile C_o. The interplay of the indium concentration and well broadening would translate into a larger blue shift in accordance with the experimental observations, while the underlying diffusion coefficient did not vary at all from structure to structure.

In order to demonstrate numerically the above argument, blue shifts of InGaAs quantum wells of compositions varying from 10% to 25% indium were computed for idealized structures, consisting initially of a 60 $\overset{0}{A}$ InGaAs quantum well embedded between thick (2000 $\overset{0}{A}$) barriers. Table 5.2 compiles the blue shifts for wells of different In compositions. The PL blue shifts are obtained by following the same transfer matrix calculations as before using an error function potential given by (5.14). The numerically calculated and the experimentally observed shifts are comparable for the 15% and the 20% SD structures. The departure between the calculated value for the 25% indium well and the experimental value is probably due to the non planar morphology of

Table 5.2. Transfer matrix results for the blue shift of luminescence from wells of different indium contents diffused at 850^{0}C for 8 hours.

Indium Content (%)	Electron Energy (eV)	Heavy hole energy (eV)	Shift (meV) (calculated)	shift (experimental)
10	0.05	0.03	29.6	14.1
15	0.06	0.04	32.1	28.4
20	0.07	0.05	43.1	50.7
25	0.11	0.06	62.9	86.4

the well. As the indium content increases, the strain energy in the structure builds up and this tends to promote a morphological instability of the quantum well interface, a feature that has been noted in numerous studies, for e.g. in Cullis et al. [62].

In summary then the experimental results on the SD structures can be rationalized on the basis of a linear model of diffusion. Attempts to directly measure the composition profile across a diffused quantum well were only partially successful. Appendix 1 describes an attempt to obtain these profiles for an $In_{0.2}Ga_{0.8}As$ quantum well which was diffused for 8 hours at 750^0C and 800^0C respectively. The profiles appear to be physically realistic and the diffusion coefficients derived from a Boltzmann Matano analysis [63] are in agreement with those obtained from simple thickness increase determinations. However the uncertainty in the point spread function of the beam (as computed from Monte Carlo simulations) overshadows this estimation of the diffusion coefficients. Consequently only analysis of the increase in thickness was used to estimate the diffusion coefficients and simulate the interdiffusion of the superlattice SL10 structure.

5.1.7. Influence of strain on the diffusion coefficient.

The motivating idea behind comparison of the PL blue shifts of two otherwise identical structures grown on different substrate orientations, is the fact that in an elastically anisotropic solid, the diffusion flux may also be anisotropic [64]. Purdy

et al. [65] have also shown that strain can enhance the diffusion coefficient and this enhancement depends on the crystal orientation. The critical parameter which is responsible for this dependence is the generalized Y parameter [64]. This Y parameter depends on the elastic constants C_{11}, C_{12}, C_{44} of the cubic crystal and the direction of the flux [η_1 η_2 η_3]. Evaluation of the Y parameter following the equations developed in [64] show that for the case of $In_{0.2}Ga_{0.8}As$ the direction of maximum Y is [111] where it has a value of 13* 10^{11} dyne/cm^2. The direction of smallest Y is [100] where it has a value of 8* 10^{11} dyne/cm^2. The diffusion coefficient enhancement as a consequence of strain in the structure is shown in [65] to be:

$$2\eta^2 Y L \qquad ..5.15$$

where Y is the generalized elastic modulus,

η = dln(a)/dc, the change of the lattice parameter with respect to composition (c) and L is the mobility. Consequently given the anisotropy of Y, we should expect anisotropy of the diffusion coefficient in an elastically anisotropic solid. Evaluation of Y in the [311] direction of $In_{0.2}Ga_{0.8}As$ yields a value of $11*10^{11}$ dyne/cm^2 which lies in an intermediate position between the elastically soft [100] and the elastically hard [111] directions. Assuming that the mobility is independent of the crystallographic direction, we would expect a greater diffusion coefficient along [311] as compared to [100]. This is of course precisely what we see in our experiments on 100S3 and 311S3 structures.

Although the system being considered is elastically very stiff, with the compliance matrix elements in the 10^{11} dyne/cm^2 range, the difference that is seen in the blue shifts along the two different crystallographic directions is very small. (~ 6 nm for the $In_{0.15}Ga_{0.85}As$ quantum well). The reason for this is apparent when we examine the values of the interdiffusion coefficient. The interdiffusion coefficient was measured to ~ 10^{-18} cm^2/s for diffusion at 850^0 C. This would translate to a very small value of mobility. Using the Nernst -Einstein relationship leads to a mobility of the order of 10^{-28} [mol.sec/gm]. η is ~ -10^{-2}. The value of the diffusion enhancement due to strain is then ($2\eta^2 Y L$) ~ 10^{-20} cm^2/s. This enhancement is 2 orders of magnitude smaller than the nominal diffusion coefficient, leading to the conclusion that strain enhancements of the interdiffusion coefficient at these indium concentrations are not pronounced.

A second interesting aspect of the 100S3 and the 311S3 as grown structures is their PL peak positions. As PL transition wavelengths depend on the strains in the structure, it is illuminating to actually compute the strain tensor for the [311] oriented structure. In order to calculate the strain tensor referred to a set of axes defined by the <100> directions the method suggested by Hinckley et al. [66] is adopted. In this technique initial computation of the strain tensor proceeds in a co-ordinate system which is rotated with respect to the cube edges. The rotation matrix depends on the growth direction. The compliance matrix in this rotated coordinate system can be calculated. Strain computation proceeds by requiring no in-plane shears and no stresses normal to the

growth plane. The strain tensor so computed can be rotated back to an axis constituted by the cube edges. When this is done non -zero shear strains appear.

Since III-V compound semiconductor materials possess no inversion symmetry it can be shown that application of a shear strain would produce piezo-electric charges in the structure [67]. These piezo-electric charges would produce a potential which tends to tilt the quantum well in the [311] structure and hence alter the Hamiltonian of the quantum well /barrier system. Numerical estimates of the shear strain and the consequent piezo electric potential drop across the structure have been made. For the case of a $In_{0.10}Ga_{0.90}As$ quantum well, 60 Å thick, grown in a [311] orientation the potential drop due to the piezoelectric charges has been estimated to be only 22 meV produced as a result of shear strains [ε_{xy}=0.0024, ε_{xz}=0.0017, ε_{yz}=0.0025]. Similar calculations yield a value of ~32meV for a $In_{0.15}Ga_{0.85}As$ well of the same dimensions and a value of ~ 41 meV for a $In_{0.20}Ga_{0.80}As$ well. This piezo drop and the dependence of the hole effective mass on the orientation of the quantum well are probably responsible for the differences seen in the PL wavelengths from the [100] and the [311]A oriented structures.

In concluding this section on thermal interdiffusion studies of InGaAs/GaAs based quantum well structures it is worth while to point out that linear models of diffusion have been shown by other authors [68] to agree with diffusion data. This study seems to confirm those observations.

5.1.8. Discussion of ion implantation enhanced quantum well interdiffusion.

5.1.8.(a) Developing a model for ion implantation enhanced diffusion.

In rationalizing the many observations of quantum well interdiffusion under the influence of ion irradiation (which were documented in (Chapters 3 and 4)) a simple model of the interdiffusion process has been developed. It must be noted that there have been many attempts to model the creation and the diffusion of point defects introduced by ion implantation [69..72], involving both Monte Carlo type calculations and more recently Molecular Dynamic calculations. Attempts to obtain the evolution of point defect concentration during annealing have certain common features. The sink terms for the annihilation of vacancies and interstitials are of the form $K_v(C_v - C_v^0)$ where C_v is the instantaneous defect concentration and the C_v^0 is the equilibrium defect concentration. Generally two types of sinks for the destruction of free defects are considered. The first is the recombination of vacancies and interstitials as mentioned above and the second is the capture of point defects by extended dislocation loops.

In developing a phenomenological model for quantum well interdiffusion, enhanced by point defects introduced by ion implantation, the first step is to generate the profile of the vacancies produced in the sample for the given implant conditions, using TRIM simulations. As will be discussed later in this section by using TRIM profiles, anneal effects and complexity of the actual defect types (for e.g. divacancy formation which is influenced by the fluence) are ignored. Subsequently it is possible to follow the diffusion

of these initial defect concentration profiles numerically, by solving the diffusion equation corresponding to each kind of point defect. The diffusion equations to be solved are:

$$\partial C_v / \partial t = \partial / \partial x (D_v \partial C_v / \partial x) + S_v \qquad ..5.16(a)$$

$$\partial C_i / \partial t = \partial / \partial x (D_i \partial Ci / \partial x) + S_i \qquad ..5.16(b)$$

$$\partial C_s / \partial t = \partial / \partial x (D_s \partial Cs / \partial x) \qquad ..5.16(c)$$

The first equation governs the vacancy concentration C_v, the second the interstitial concentration C_i while the final equation gives the indium concentration for InGaAs/GaAs based quantum wells or Al for the case of GaAs/AlGaAs based quantum well structures. In the above equations D is the diffusion coefficient, S is a sink term and x is the spatial coordinate. It must be noted that the above three equations are coupled. The sink terms in the vacancy and interstitial equations couple the two evolution equations. The diffusion coefficient that the quantum well material experiences is determined by the instantaneous concentration of the vacancies. This couples the indium evolution equation and the vacancy evolution equation. In principle quantum well interdiffusion would also contribute a source term in the vacancy interdiffusion equation because of the Kirkendall effect, but this has been neglected in the model in the interests of simplicity.

In solving equations (5.16a, 5.16b) the initial defect profile is usually obtained from TRIM simulations. The difference between the initial vacancy profile and the interstitial profile is assumed to be small as in [70]. The diffusion coefficients for the defect species can be estimated from jump distances and migration enthalpies [73]. Following [74] the vacancy diffusion coefficient is taken as

$$D \sim \langle b^2 \rangle / 2\tau \qquad ..5.17(a)$$

where $\langle b \rangle$ is the jump distance and τ is the jump period given by

$$\tau = e^{\Delta G_v / kT} / \nu_0 \qquad ..5.17(b)$$

In the above equation ν_0 is the fundamental vibration frequency of an atom in the solid (~ 10^{13} Hz) and ΔG_v is the vacancy migration enthalpy. Following the literature [75], the interstitial diffusion coefficient is assumed to be an order of magnitude larger than the vacancy diffusion coefficient. In this calculation a diffusion coefficient of 10^{-11} cm^2/s for the vacancies (from 5.17) and 10^{-10} cm^2/s for the interstitials has been chosen at the annealing temperature of 850^0 C. The key issue in this simulation is the nature and distribution of the sink terms. As has already been mentioned two types of sink terms have been considered. Recombination of vacancies and interstitials is modeled after the early work of Brown et al. [74]. These authors show that if a vacancy is captured by a spherical sink representing an interstitial, the concentration of vacancies N(t), would change in time according to

$$N(t) = N(0)\left(1 - a/b + a/b \; \mathrm{erf}((b-a)/2\sqrt{Dt})\right) \quad ..5.18$$

a = radius of the sink. (~ order of the atom size)

b = distance of the vacancy from the sink. (since a finite difference solution is adopted, this distance is ≤ the thickness of a depth bin)

D is the vacancy diffusion coefficient.

In a similar way Brown et al. [74] also show that the capture of point defects by extended crystal defects like dislocations can be modeled as :

$$N(t) = N(0)\, e^{-1/2\, \alpha_0^2 \langle b^2 \rangle \, t / \tau} \quad ..5.19(a)$$

α_0 is a parameter implicitly related to the inter dislocation loop spacing R_D through :

$$\alpha_0^{-2} = R_D^2 /2 \; [-\gamma + \ln (2.0/ \alpha_0 r_d)] \quad ..5.19(b)$$

where γ is Euler's constant = 0.577 and r_d is of the order of the Burger's vector of the dislocation.

$\langle b \rangle$ is the distance traveled in one jump by the diffusing species.

τ is the jump period governed by the jump frequency and migration enthalpy as defined by 5.17(b).

It is clear from the above expression that the capture rates of the crystal defects would vary with the geometry of the dislocation loop ensemble in the crystal. Indeed second order processes like Ostwald ripening of dislocation loops have been reported in the silicon processing literature, [76,77] which would coarsen the loop size and change the interloop spacing as annealing progresses. This would translate to a temporal dependence of the α_0 parameter and hence capture rates. Evaluation of the rate of change of the α_0 parameter with data from the silicon processing literature [77] however failed to reveal a strong dependence on time and in the interests of simplicity a constant value has been utilized. The Burgers vector and the interloop spacing have been estimated from TEM micrographs and reveal that $\alpha_0 \sim 5*10^{-5} / \mathring{A}$.

5.1.8.(b) Numerical solution of the diffusion equations.

With the sink terms handled by the procedures above we can proceed to discretize the diffusion equations (5.16) using a finite difference approach. The method suggested by Patankar et al. [78] or the control volume formulation is adopted. The grid is equispaced (the spacing is dependent on the TRIM data bins) in the depth direction. The following discretization equation is easily derived for the configuration shown in Fig (5.5):

$$C_p[\Delta x / \Delta t + d_e / \delta x_e \quad + d_w / \delta x_w \quad] = (\quad d_e / \delta x_e) C_e \quad + (d_w / \delta x_w) C_w \quad + [\bar{S}(\Delta x) + C_p^0 (\Delta x / \Delta t)]$$

..5.20

In the above expression

C_p is the concentration at the point P.

C_e is the concentration at the point E, east of point P

C_w is the concentration at the point W, west of point P

d_e, d_w are the diffusion coefficients at points E and W.

C_p^0 is the concentration at an immediately prior time step at point P.

$\bar{S}$ is the average sink term which has been derived in the previous section.

While the diffusion coefficients of the vacancies and interstitials are assumed invariant with position and time, the diffusion coefficient for well evolution will depend on both position and time as it scales with the vacancy concentration. For the vacancy profile only recombination with interstitials determines the trap rate, while for interstitials recombination with vacancies and capture by dislocation loops determines the trap or the sink rate. The dislocation loop sinks are assumed to operate only in the bottom half of

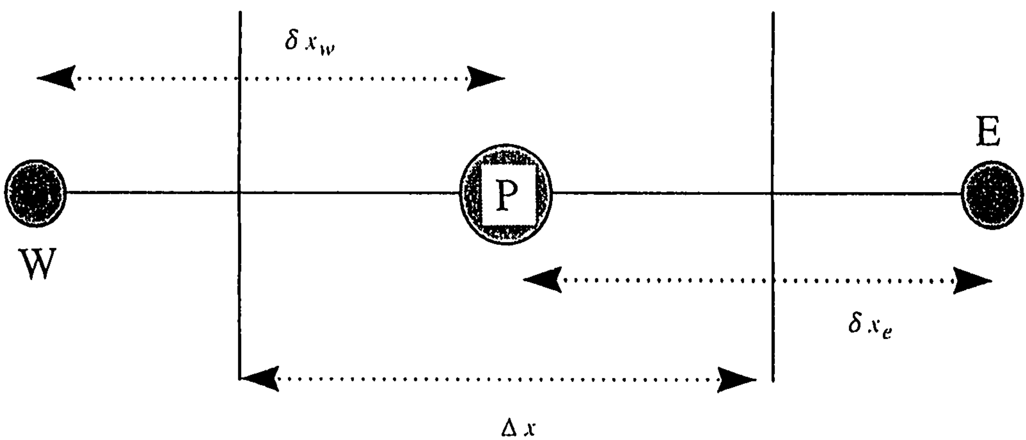

Fig 5.5 Node configuration for finite difference calculation.

the initial concentration profile (end of range loops) while recombination sinks(point defects of opposite kinds combining) operate over the entire range. The specific discretization equations for the vacancies, interstitials and quantum well material can be individually derived. The solution of this set of equations can then be carried out following a tridiagonal matrix scheme [78].

Finally in Fig (5.6) (a, b) we have the results of tandem solution of the vacancy, interstitial and well evolution equations. As can qualitatively be seen in this simulation for the case of a 6 MeV implant ($R_p \sim 2.3$ μm) into a $Al_{0.7}Ga_{0.3}As$ (1.7 μm) / GaAs (60 $\overset{0}{A}$) / $Al_{0.7}Ga_{0.3}As$ (1.7 μm) structure, well broadening after a 30 second anneal at 850^0 C can be substantial. The 60 $\overset{0}{A}$ quantum well has a nominal width now ~100 $\overset{0}{A}$ which is of the same range as the experimental data for the well thickness with HRTEM. However estimation of the sink terms renders the task of fitting the experimental data to the model difficult at best. Additionally for both AlGaAs/GaAs and InGaAs/GaAs only the defects introduced by ion implantation on the group III lattice need to be considered. TRIM simulations only provide the total defect concentration without regard to their III and V concentration. Consequently the interdiffusion enhancement would be overestimated in the above model as the TRIM defect outputs are used for the initial concentration profile of the defect species. In light of the above limitations, only a rationalization of the trends seen in the data is attempted rather than a rigorous comparison of the predictions of this model with experimental data.

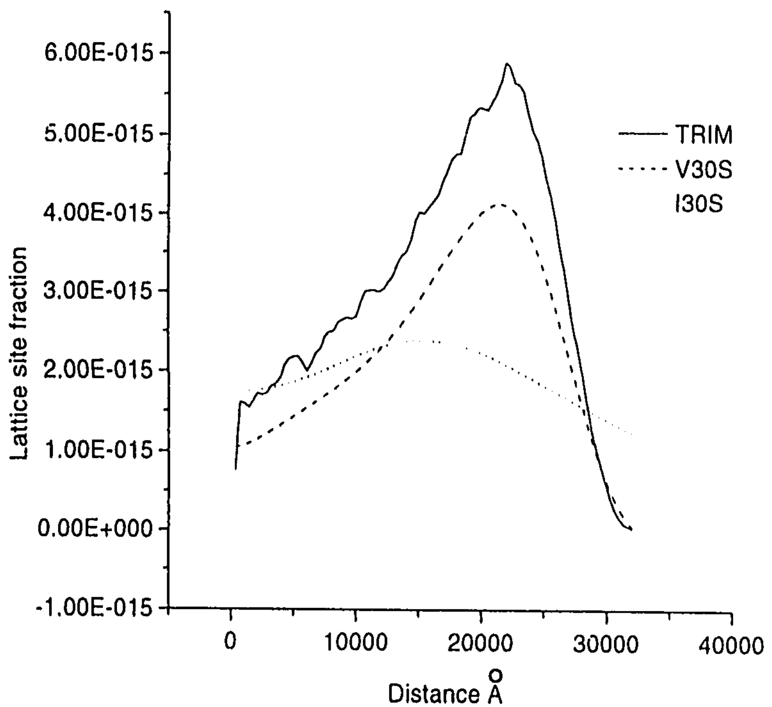

Fig 5.6 (a) Vacancy and interstitial evolution after annealing at 850^0 C for 30 seconds. (6 MeV implant).

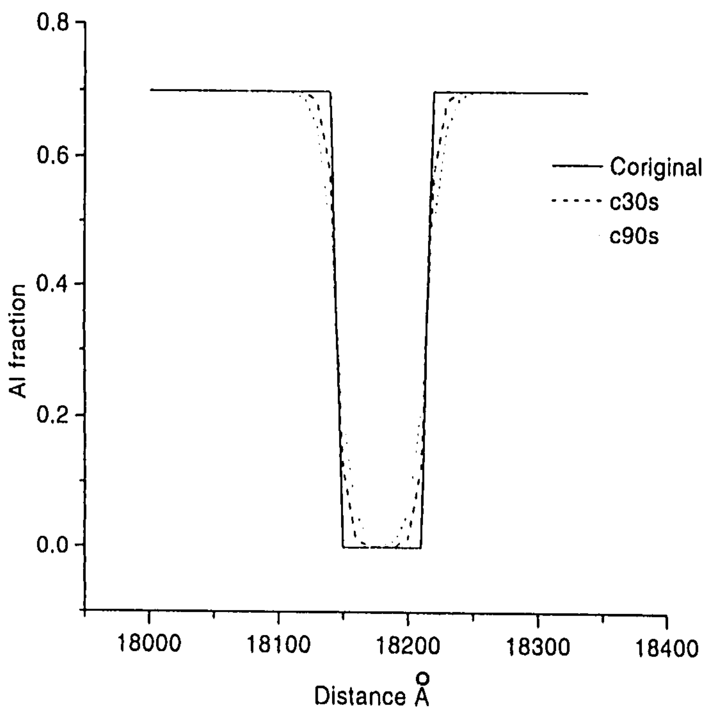

Fig 5.6(b) GaAs well evolution after 30 seconds and 90 seconds annealing at 850^0 C.

It must also be emphasized that in these simulations the experimentally established asymmetry of the AlAs/GaAs and the GaAs/AlAs interfaces and segregation effects [79] are ignored by choosing a rectangular composition profile at initial time for Al. Both effects lead to non square initial profiles for Al. The omission is once again in the interests of simplicity. One could just as easily begin with a non square profile and run the simulation.

5.1.9 Implications of model : General discussion of trends in implantation experiments.

The central conclusion from the above simulation is that the well broadening would depend on its position relative to the vacancy profile. Consequently a larger diffusional enhancement is expected when the well is situated at the peak of the initial vacancy profile as compared to a situation where the well is situated in the tails of the vacancy profile. This can be seen by performing another simulation, where well evolution is considered for a 2 MeV implant into the same structure as in the simulation leading to Fig (5.6). In this case the range of the ions is $R_p \sim 0.9\ \mu m$ and the annealing conditions are the same as the 6MeV implant, namely 30 seconds at 850^0C. For this implantation condition the well situated at a depth of 1.7 μm is in the tail of the vacancy distribution. In consequence it is clear that the broadening is less marked. Fig (5.7) shows the situation for this case. In a qualitative way then we can understand the dependence of the

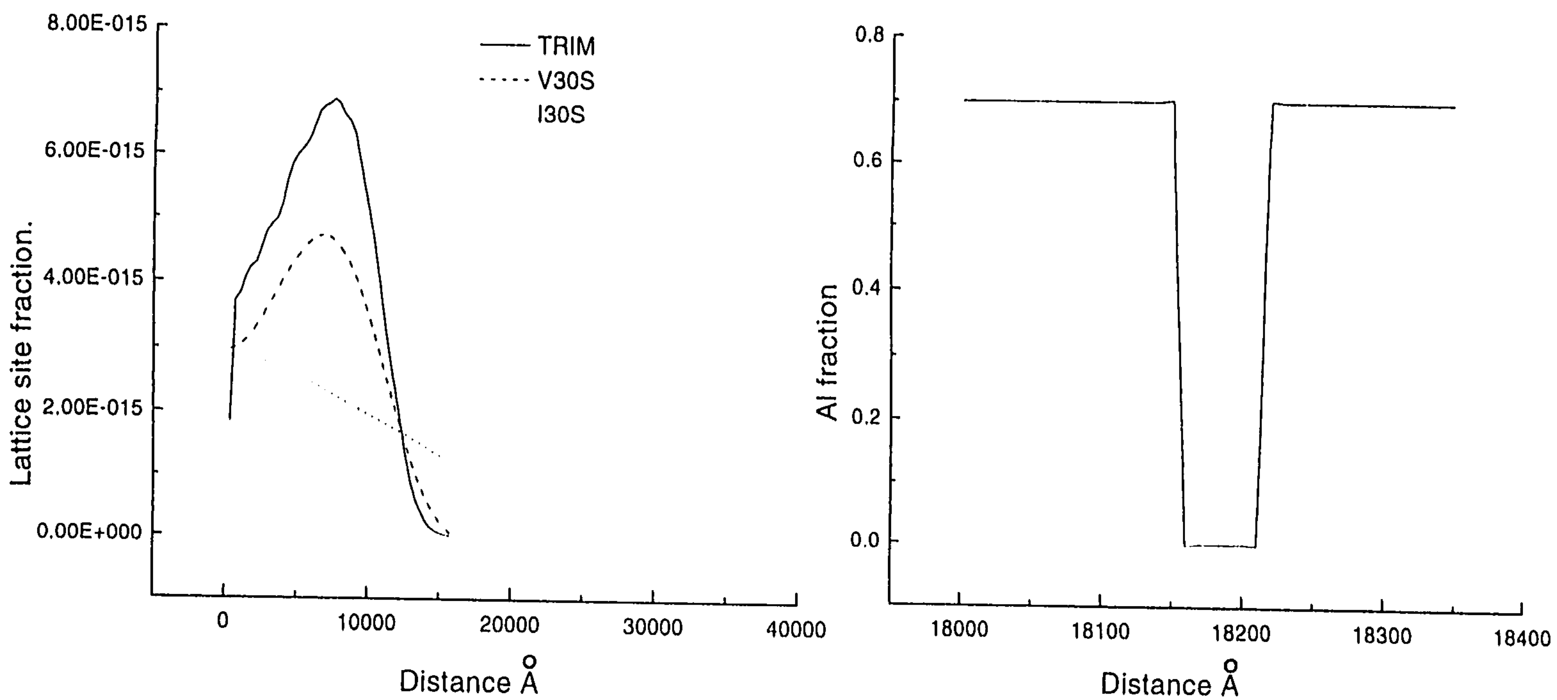

Fig 5.7(a) Evolution of the vacancy and interstitial profile after annealing at 850^0 C for 30 seconds. (2 MeV implant)

Fig 5.7(b) GaAs well after diffusion at 850^0 C for 30 seconds.

well width on the implantation energy, a feature that was documented in the experimental section of this thesis (Chapter 4). This simulation lends some numerical credence to claims in the literature that the well width and consequently the blue shift in luminescence depend on the vacancy profile produced by implantation, and the position of the well in this vacancy profile. [80, 81].

A distinct feature of the interstitial dislocation loops that were observed in the implanted and rapid thermally annealed samples was their tendency to cluster at the GaAs spacer layers in the AlGaAs cladding. (Structures A1, I1). Presumably energy minimizing calculations in the same spirit as calculations that have been performed on stable dislocation configurations in silicon based structures [82] would indicate the preferred habit of these dislocation loops. However their tendency to be located exactly at these planarization layers is intriguing. It is quite possible that effects more subtle than mere capture at an interface [74] are involved. Indeed the defects that are produced in the crystal as a result of ion implantation are electrically charged and would be subject to electrostatic forces. They drift under the influence of these forces to AlGaAs/GaAs interfaces where they are trapped due to the band gap discontinuity [83,84]. Bode et al. [84] conclude that ion implantation defects are charged and migrate under the influence of electrostatic fields. Their conclusions were based on disordering experiments with n-i-p type structures and p-i-n type structures where they were able to demonstrate reversal of disordered interfaces with reversal in the doping sequence. [84]. The absence of clustering of implantation damage at any specific location in the A2, I2 structures is

consequently understood in light of the above explanation of defect location. In both these structures there are no GaAs planarization layers.

Most of the above conclusions regarding the well width dependence on implant energy (which was simulated for AlGaAs/GaAs) structures can be readily extrapolated to the case of InGaAs/GaAs. The dependence of the well width and hence blue shift on implant energy is due to the same reasons advanced above. Clustering of defects at specific locations is once again understood along the same lines. A point that needs elaboration is however the 5 MeV implanted I1 sample where two distinct peaks are observed in the PL of the implanted and annealed sample. At first sight it may appear that the width of the two wells in the structure are different, since the wells are located at different positions in the initial vacancy profile. In order to gauge the difference in the extent of disordering a diffusion simulation was run on TRIM generated defect profiles. These defect profiles were generated for a structure whose configuration is :

GaAs (1.7 μm) / $In_{0.2}Ga_{0.8}As$ (60 $\overset{o}{A}$)/ GaAs (250 $\overset{o}{A}$)/ $In_{0.2}Ga_{0.8}As$ (60 $\overset{o}{A}$)/ GaAs (1.7 μm).

The quantum wells were assumed to have a rectangular indium profile to start with. This is once again an obvious simplification as indium segregation has been found in InGaAs wells grown on GaAs [85,86]. (As explained in the case of AlGaAs/GaAs the simulation can be run on non-square profiles without any modification of the code.) A marked difference in the extent of interdiffusion is not seen for the two wells, in

qualitative agreement with TEM results. The results for this simulation are in given in Figures 5.8 and 5.9. It is therefore plausible that differences in the quantum well compositions as (evidenced by pronounced fringes in dark field TEM micrographs) are responsible for the observed PL peak splitting.

The dependence of the blue shift on the temperature of implant in the I1 structures also merits closer examination. The dependence of the blue shift may be explained by the dependence of the damage profile on the implant temperature. As implantation proceeds, a self annealing process also operates whereby vacancies and interstitials which are in close proximity annihilate. The dynamic balance between the implantation induced defects and their destruction through this self healing process determines the number of defects which remain following the implantation. In very early work on this self annealing process Kinchin et al. [87] point out that this recombination process which leads to self annealing is thermally activated and would consequently be less pronounced as the implant temperature falls. In consequence then it is to be expected that for identical implantation conditions of dose and energy, lower temperature implants would produce a greater number of vacancy-interstitial pairs, which would then be available to enhance the interdiffusion coefficient during the subsequent rapid thermal anneal. A second aspect is the clustering of implant damage in the low temperature implanted sample. This may be rationalized on statistical grounds. If we consider a random walk in a lattice with a random distribution of traps (which simulates a diffusing interstitial which can be captured by either a vacancy or dislocation loop) the mean

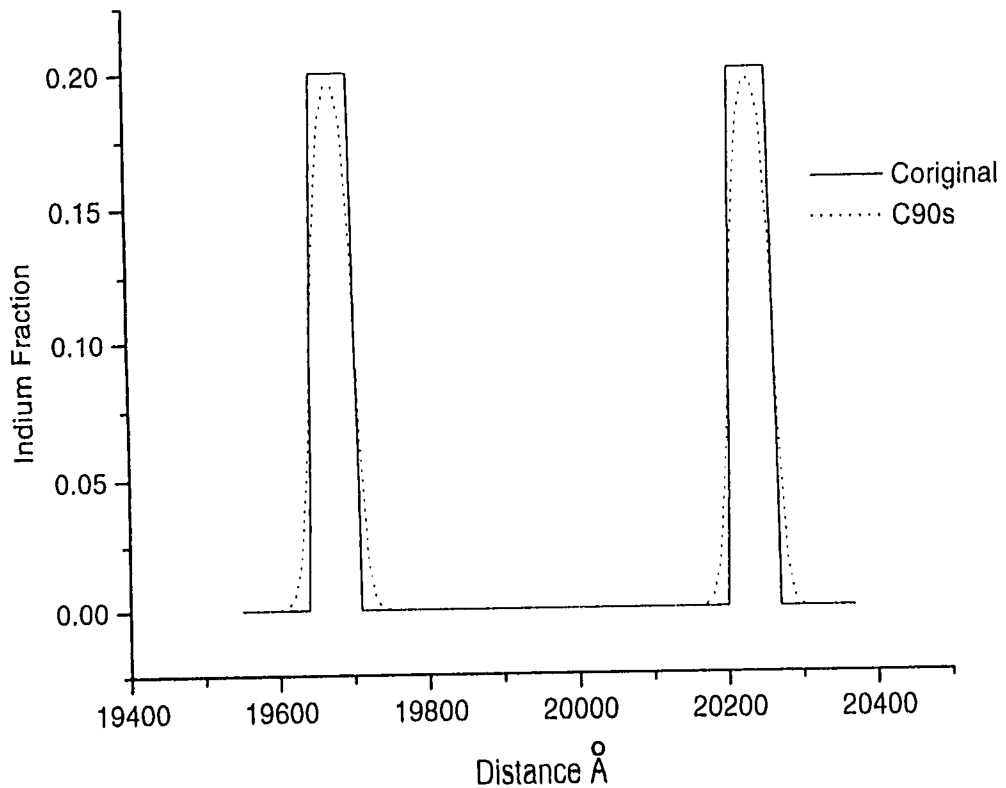

Fig 5.8 Evolution of $In_{0.2}Ga_{0.8}As$ quantum wells after diffusion at 850^0 C for 90 seconds. (5 MeV implant).

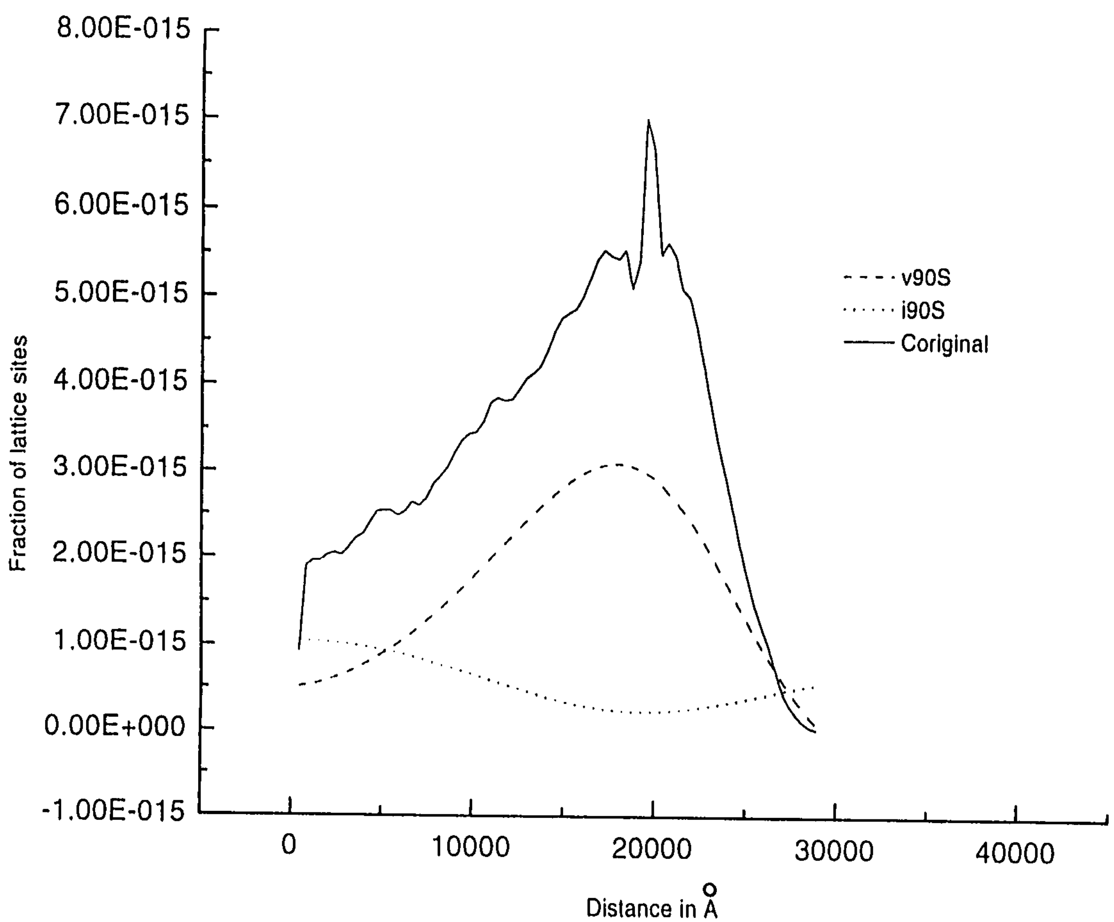

Fig 5.9 Evolution of the vacancy and interstitial concentration with 90 seconds annealing at 850^0 C.

square displacement of the random walker is expected to be dependent on the trap density [88]. As the probability of a given site in a lattice being a trap increases, the mean square displacement of the random walker before capture would accordingly fall. Clustering can be understood on these somewhat simplified grounds as a manifestation of reduced mean square displacement before capture in a lattice with a larger trap density.

Turning to implantation experiments on the SD samples we observe that the increase of the blue shift with the implant dose is not monotonic. In this observation is one of the main concerns of ion implantation enhanced quantum well interdiffusion. As the dose and energy increase, it is to be expected that a substantial fraction of the initial implant defect profile still remains following rapid thermal annealing. Point defects introduce levels into the band gap of a semiconductor, with the consequence that non-radiative recombination is facilitated. In time resolved studies on 33 keV and 100 keV As^+ (dose $10^{13}/cm^2$) implanted SD20 structures (Appendix 3) it was observed that the decay time of luminescence fell from 1.21 nanoseconds to 0.71 nanoseconds, indicating the increasing role of non-radiant recombination. This translates to reduced luminescent intensity to a point where no luminescence at all was observed in the case of the 300 keV ($5*10^{13}/cm^2$) implanted SD structures.

Another associated problem, apparent in the case of high energy implants (8 MeV implants on A1 AlGaAs/GaAs based structures), is the broadened linewidth of the PL from the GaAs wells. This can be traced to the collisional disordering of the quantum

well interfaces under the influence of a high energy implant which subsequent rapid thermal annealing is apparently unable to repair. The effects mentioned in this paragraph and the previous one serve to illustrate potential problems with implantation enhanced quantum well disordering for optoelectronic device integration.

In conclusion it is worthwhile to point out that excess defects which enhance quantum well interdiffusion can be introduced by methods other than ion implantation. In one method [90,91] the structure is capped with SiO_2 and rapid thermally annealed. For GaAs capped with SiO_2, outdiffusion of Ga into SiO_2 produces Ga vacancies in GaAs which can diffuse down to the underlying quantum wells and assist interdiffusion. In a second method an energetic laser pulse is used to irradiate the sample, creating a hot carrier plasma and throwing off energetic phonons in the crystal, thus creating lattice damage which can assist interdiffusion during the subsequent rapid thermal anneal [91]. The ultimate choice of the technique for technological application will depend on a combination of spatial selectivity, reproducibility and luminescence recovery.

Chapter 6

SUMMARY AND CONCLUSIONS

Two main experiments were conducted in the course of this work

1. **Annealing experiments on superlattice structures:**

a. Annealing experiments conducted on $In_{0.2}Ga_{0.8}As/GaAs$ superlattice structures revealed that an initial rectangular composition wave of indium with a period of 40 $\overset{0}{A}$ annealed out to a single thick (~ 400 $\overset{0}{A}$) indium enriched region after diffusion at 850^0 C for a period of 6 hours. Concomitant with this homogenization the satellite peaks in the X-ray diffraction from this structure also vanished over the same period of time. Photoluminescence from the annealing superlattice shows an initial redshift (~ 15 nm) with respect to the as grown peak at short annealing times (~ 20 minutes) followed by blue shift which carries the luminescence peak back across the position of the as grown peak at longer annealing times (~ 8 hours).

b. A linear model of diffusion which involves convoluting the initial concentration profile with a Gaussian point spread function, to obtain the evolution of the superlattice is capable of explaining the salient features of the annealing experiments. This model produces composition profiles in agreement with TEM results, X-ray

diffraction estimates in qualitative agreement with experimental spectra and PL transition energies which replicate the experimental trends.

c. Both strain and composition effects on diffusion do not appear to be marked in the composition range of indium studied. Trends seen in the PL from annealed single quantum wells in the composition range (10% - 20% indium) can be rationalized on the basis of a single, composition invariant interdiffusion coefficient. Trends seen in the PL from [100] and [311] A oriented structures suggest that in the composition range studied strain effects are also not marked.

2. Implantation enhanced quantum well interdiffusion.

a. Characterization experiments conducted on As^+ implanted AlGaAs /GaAs based structures suggest that the interdiffusion coefficient for the annealing conditions employed (850^0C)is enhanced by about three orders of magnitude over the interdiffusion coefficient for annealing in the absence of ion implantation.

b. (1-8) MeV level ion implants produce extended dislocation loops. These dislocation loops were found to be interstitial in character. The Burgers vector of these loops was found to be $[\bar{1}10]$.

c. The tendency of the dislocation loops to cluster at the GaAs planarization layers was observed in a variety of samples. This is probably a consequence of electrostatic effects.

d. The extent of interdiffusion between the quantum well and barrier was found to increase with increasing implant energy. The quantum well interdiffusion as a function of implant energy is related to the vacancy profile produced by the implantation. Interdiffusion is maximized when the well is located near the peak of the vacancy profile.

e. The temperature dependence of the blue shift can be rationalized on the basis of the thermal activation required for defect annealing. Lower temperatures of implantation (~77K) gave larger blue shifts than room temperature implants.

f. The magnitude of the blue shift is not a monotonic function of implant dose. For As^+ implantation doses that exceeded $10^{13}/cm^2$ single and double InGaAs quantum well structures ceased to luminesce. This probably has to do with the fact that annealing at 850^0C does not entirely remove non-radiant recombination centers introduced by ion implantation.

g. The ultimate choice of the technique for diffusional enhancement for technological application may lie in the trade off between reproducibility of blue shift, spatial selectivity and luminescence recovery.

Appendix 1

BASIC EQUATIONS OF DIFFUSION.

For the case of binary incoherent diffusion, the flux J_1 of component 1 is related to the gradient in the chemical potential ($\mu_1 - \mu_2$) through the equation [65] :

$$J_1 = -L\, d(\mu_1 - \mu_2)/dx \qquad ..A1.1$$

In the above equation L is the mobility and x is a spatial co-ordinate. The same equation can also be written in terms of the diffusion coefficient D and the gradient in composition C_1 of component 1 using

$$J_1 = -D_1\, d\, C_1/dx \qquad ..A1.2$$

The diffusion coefficient D_1 in equation (A1.2) can be expressed in terms of the mobility L and the free energy f using equation (A1.1). The free energy f can be written in terms of the chemical potentials of components 1 and 2 (μ_1, μ_2) as:

$$f = C_1\mu_1 + C_2\mu_2 \qquad ..A1.3$$

Since ($C_1 + C_2$) = 1 for a binary system we find as as result of the Gibbs Duhem equation [65] :

$$df / dC_1 = (\mu_1 - \mu_2) \qquad ..A1.4$$

Utilizing A1.4 in equation A1.1 we find that

$$J_1 = (-L \; d(\mu_1 - \mu_2) / dC_1) (dC_1 / dx)$$

$$= (-L \, d^2 f / dC_1^2) (dC_1 / dx) \qquad ..A1.5$$

The diffusion coefficient can be identified from the above equation and (A1.2) as equal to

$$D_1 = (-L \, d^2 f / dC_1^2) \qquad ..A1.6$$

In the above equation (A1.6), the diffusion coefficient can be identified as the product of two terms. The first is a purely kinetic term L and the second is a purely thermodynamic term, the curvature given by the free energy f - c dependence. The interdiffusion coefficient $\tilde{D}$ which is used in section 5.1 of the thesis can be written in terms of the intrinsic diffusion coefficients D_1 and D_2 of components 1 and 2 as

$$\tilde{D} = D_1 C_2 + D_2 C_1 \qquad ..A1.7$$

In the general case of multicomponent diffusion, the single diffusion coefficient of the binary case D, is replaced with a matrix of diffusion coefficients [D]. [D] is related to the mobility matrix [L] and a thermodynamic matrix [f] through:

$$[D] = [L] [f] \qquad ..A1.8$$

The elements of the thermodynamic matrix [f] are of the form

$$f_{ij} = \partial^2 f / \partial C_i \, \partial C_j \qquad ..A1.9$$

For the case of binary coherent diffusion the f in equation in (A1.6) is replaced by a quantity ϕ. This is related to f through

$$\phi = f + \eta^2 Y (C_1 - C_0)^2 \qquad ..A1.10$$

In the above equation the additional contribution is due to strain energy density in the crystal system. In A1.10 the term η is the change of lattice parameter a, with composition C_1

$$\eta = (1/a)\, da / dC_1 \qquad ..A1.11$$

Y is a generalized elastic constant which depends on both the crystallographic direction and elastic constants of the crystal. [65]. C_0 is a reference composition used to compute the strain energy.

Using A1.6 with f replaced by ϕ the coherent diffusion coefficient $\hat{D}$ can be calculated in terms of the incoherent diffusion coefficient D

$$\hat{D} = D + 2Y\eta^2 L \qquad ..A1.12$$

The enhancement of the diffusion coefficient due to strain in the system is hence $2Y\eta^2 L$. The same analysis can be extended to the case of multicomponent diffusion. In this case however it is necessary to consider the variation of lattice parameter with respect to several components. Consequently it is necessary to define parameters η_1, η_2 $..\eta_n$ which account for the variation of the lattice parameter with respect to components 1, 2 ..n. The matrix formulation of the diffusion coefficient (A1.7) can then be used with individual elements enhanced by strain related contributions.

Appendix 2.

MONTE CARLO/FOURIER TRANSFORM BASED COMPOSITION PROFILE ESTIMATION.

The central objective underlying this effort was to obtain the compositional profile across diffused InGaAs quantum wells and to extract values for the In-Ga interdiffusion coefficient. In order to do so, the experimental and computational procedures as detailed below have been followed.

The first step in the determination of the compositional profile is energy dispersive X-ray analysis of diffused samples in the JEOL 2010F scanning transmission electron microscope. When the sample is excited with an electron beam, characteristic X-rays depending on the elemental constitution of the probed volume are generated. Typically in this study spectra were acquired for 50 seconds. The total X-ray count rate during this period of time was ~1000-1300/second. The peaks of interest in this work are those due to Ga and In. The integrated intensity under a characteristic elemental peak is a measure of the concentration of the element in the volume probed by the electron beam. However the region "probed" by the exciting electron beam is larger than the volume determined by the incident beam diameter when it enters the sample; the electrons experience a number of scattering events which result in their spreading as they traverse the sample. Consequently it is necessary to "deconvolute" the experimentally determined

composition, by estimating the profile of the electron probe as it passes through the TEM foil.

Generally in the literature the probe current profile has been estimated by Monte Carlo simulations. Consequently the same procedure has been adopted in this work. A Monte Carlo simulation (suitably modified to account for the geometry of the samples analyzed in this work) is used to obtain the beam current distribution in the sample following the theory in [92]. In this simulation a spherical polar co-ordinate system is adopted and electron trajectories are simulated by considering a series of elastic scattering events. During each trajectory calculation, the effect of inelastic scattering is taken into account, by assuming that the electron loses energy as a function of distance travelled between elastic scattering events. Typically ~ 1500 trajectories are simulated to obtain sufficient statistics.

For the incident electron probe, a Gaussian current distribution with full width at half maximum of 5 $\overset{0}{A}$ and a convergence semiangle of 12 milliradian has been used. At every elastic scattering event the electron suffers a deflection through an angle Φ with respect to the incident direction, and through an azimuthal angle Ψ. The distance travelled between elastic scattering events, or the path length is determined by the screened Rutherford elastic scattering cross-section σ_E . For an electron incident with an energy E, σ_E is given by [93]:

$$\sigma_E = 5.21 * 10^{-21} (Z^2/E^2) (4\pi/\gamma(1+\gamma))(E + 511/E + 1022)^2 \quad cm^2 \qquad ..A2.1$$

In the above equation Z is the atomic number and γ is the charge screening factor.

The charge screening factor for estimation of the Rutherford scattering is obtained from Bishop et al. [94]. It is given by

$$\gamma = 3.4*10^{-3} Z^{0.67}/E \qquad ..A2.2$$

Following evaluation of σ_E and γ, the mean free path λ_p of an electron (with energy E) in the material is calculated using the expression:

$$\lambda_p = A / (N_A \, \rho \, \sigma_E) \, 10^7 \quad (nm) \qquad ..A2.3$$

In equation (A2.3) A is the atomic weight in (gm/mole) and N_A is Avagadro's number. At each scattering event, the deflection angle is obtained from:

$$\phi = \cos^{-1} (1-(2\gamma.rnd/1+\gamma-rnd)) \qquad ..A2.4$$

where rnd stands for a random value between 0 and 1. The azimuthal angle ψ is assigned any value lying between 0 and 2π. Each separate path length is related to the mean free path λ_p using the following equation:

$$st = -\lambda_p \ln (rnd) \qquad ..A2.5$$

Instead of calculating each individual inelastic scattering event, the electron is assumed to lose energy continuously as it travels through the material. This rate of inelastic energy loss is calculated following the relation of Bethe et al. [95]:

$$dE/ds = -78500 \, (\rho \, Z/AE) \ln(1.166E/J) \qquad ..A2.6$$

In equation (A2.6), J is the mean ionization potential in keV of the material. This represents the rate of energy loss due to all possible inelastic scattering events, and can be calculated using the expression provided by Berger and Selzer [96].

$$J = (9.7\,Z + 58.5/Z^{0.19})\,10^{-3} \quad \text{(keV)} \qquad ..A2.7$$

The amount of energy lost between successive collision events is $-\Delta E$ where

$$\Delta E = st\,(dE/ds) \qquad ..A2.8$$

After each path calculation, λ_p is re-evaluated to take into consideration the drop in electron energy. Trajectories are calculated until the electron exits the bottom of the foil. The foil thickness necessary for this calculation was obtained from E.E.L.S. (electron energy loss spectroscopy). Typically foils were about 200 nm thick.

Following estimation of the probe current distribution in the sample, the experimentally determined composition profile was deconvoluted point by point, by division in the Fourier Transform domain. The Fourier Transform of the experimental data and the estimated point spread function was carried out numerically with the software package Matlab [97]. The final profile was reconstructed utilizing a power spectrum estimation and Weiner Optimal Filtering [98] which reduces noise in the Fourier Transform by filtering out the high frequency components. Figures A2.1 and A2.2 show the final computed profiles of the single quantum well in the SD20 structure (single and double quantum well structure with InGaAs quantum wells) diffused at 750^0 C and 800^0C for 8 hours respectively.

The profiles are physically realistic because the centre of the quantum well is enriched in Ga as interdiffusion proceeds. Utilizing a Boltmann Matano approach [63] an average interdiffusion coefficient of $\sim 4*10^{-19}$ cm^2/s and $\sim 6*10^{-19}$ cm^2/s is obtained for the 750^0C and 800^0C diffused structures respectively. The uncertainity in this method of measuring the interdiffusion coefficient lies in the statistical deconvolution procedure. Since the raw data from energy dispersive X- Ray analysis is noisy to begin with (because of the Poisson process underlying photon counting) deconvolution further multiplies this uncertainity. Consequently rather large uncertainities (indicated in figures A2.1, A2.2) result. Nevertheless it is worth noting that the interdiffusion coefficients obtained by this method are in reasonable agreement with those calculated from the increase of the quantum well thickness. For the 850^0C diffused structure the increase in quantum well thickness yielded an inter diffusion coefficient value of $\sim 10*10^{-19}$ cm^2/s .

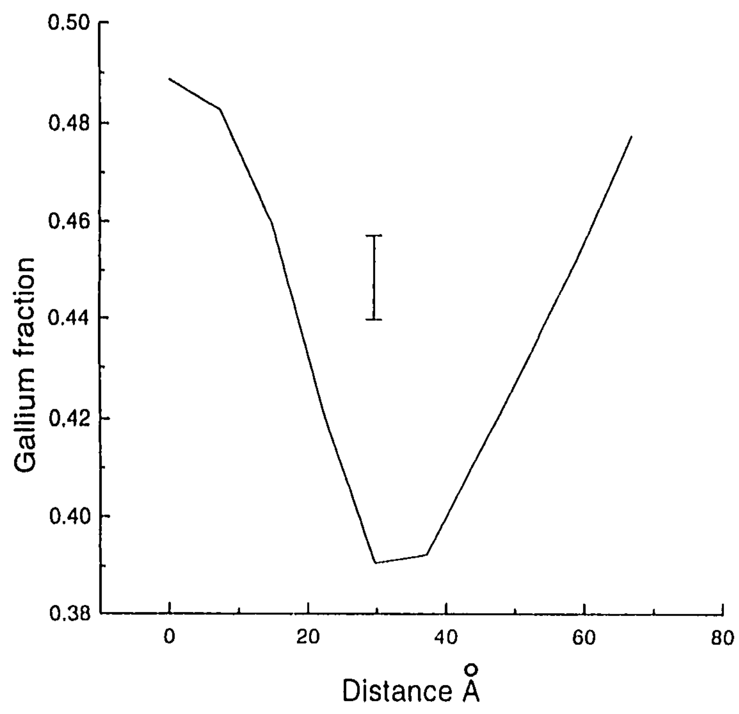

Fig A2.1 Deconvoluted profile of single quantum well in SD20 structure annealed at 750^0 C for 8 hours.

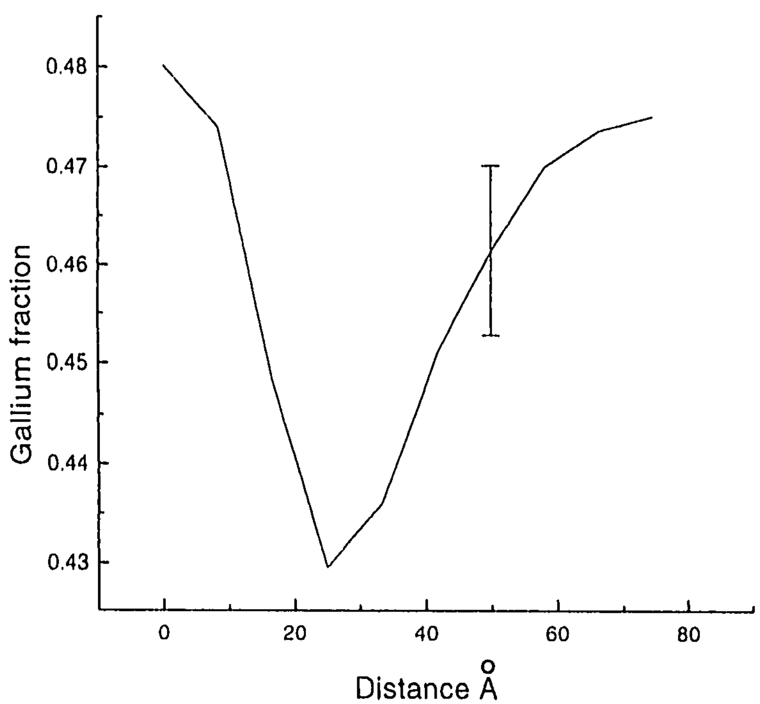

Fig A2.2 Deconvoluted profile of single quantum well in SD20 structure annealed at 800^0 C for 8 hours.

Code for Deconvolution.

```
% this function deconvolutes the supplied
% matrix

function [matrix,err] = deconar2(array,period,avcon)

 % array contains the convoluted sequence.
 % array first colomn contains the distances(angstrom)
 % array second colomn contains the concentrations.(fraction of ga)
 % array third colomn contains the thickness value.(angstrom)
 % period is the physical sampling interval.
 % av con contains the average concentration.(deduced from PL)


   k= length(array(:,2));
      for i= 1:k
        avarray(i,2) = avcon;
     end
        avarray(:,1) = array(:,1);
        avarray(:,3) = array(:,3);

 [c1,l1,r1] = mmonte(avarray(1,3),0.012,1000,avarray(:,2),avarray(:,1),period,avarray(1,1));


[c2,l2,r2]=
mmonte(avarray(1,3),0.012,1000,avarray(:,2),avarray(:,1),period,0.5*(avarray(1,1)+avarray(k,1)));
 [c3,l3,r3] = mmonte(avarray(1,3),0.012,1000,avarray(:,2),avarray(:,1),period,avarray(k,1));

 save 'c1.dat' c1 -ascii; save 'l1.dat' l1 -ascii; save 'r1.dat' r1 -ascii;
  save 'c2.dat' c2 -ascii; save 'l2.dat' l2 -ascii; save 'r2.dat' r2 -ascii;
 save 'c3.dat' c3 -ascii; save 'l3.dat' l3 -ascii; save 'r3.dat' r3 -ascii;

i=1;
while (i<=k)
 if(i<=3)
    conpr = c2 ;  l =l2; r=r2;
   else
     if((i>3)&(i<6))
      conpr = c2 ; l =l2; r=r2;
        else
      conpr = c2 ; l =l2;  r=r2;
     end
   end


 lower =  (array(i,1)-2) -(2*l-1)*4;
    upper = lower + (2*(l+ r)-2)*4;
       points = [ lower:4:upper];
    conseq = inter(array(:,2),array(:,1),period,points);
```

```
for j= l+r+1: length(conseq)
      conpr(j)=0;
     end
     fcons = fft(conseq);
           fconpr = fft(conpr);
             fdecon = fcons./fconpr;
              [phif,power,es,sig] = weiner(fdecon);
               phif= phif(1:length(fdecon));
                fdecon= fdecon.*phif;
               decon =abs(ifft(fdecon));
             array(i,2) = 0.5*( decon(l) +decon(l+1));
           end
     i = i+1;
   end
[s,a,b] = smooth(array);
matrix = s;


function[conpr,ll,lr]= mmonte(thick,thetae,nu,comp,dis,period,pos)


% m file for the implementation of Monte Carlo calculation.
% thick is the foil thickness.(this has to be in angstrom)
% thetae the beam convergence semiangle
% nu is the number of electrons to be simulated
% comp is the composition array.(fraction of Ga)
% dis is the distance array ( distances are in ao).
% period is the physical sampling interval.
% pos is the distance to the beam centre from the layer edge.  (in ang)
% xfr,xfl,arrays to store fractions of electrons which wind up in these
% spatial regions.
% distances are measured in multiples of 1 ao.

           xfl  = retzero(3000);
           xfr =  retzero(3000);


  count =0;
   for r= 0:6

%compute fractions in the radial regions.


         fracd= quad('profile', 0,6);
             fracn= quad('profile', r, r+1);
           frac= fracn/fracd;
         nuf = ceil(frac*nu);


for c = 1:nuf
```

```
 corde = [ 0 0 0 ];

  lp =retzero(3000);
  rp =retzero(3000);


    %initialize distance travelled and electron energy.

     lent=0;

     % energy is in kv.
       e= 200;
    upsilon = rand(1)*2.0*pi;  %azimuth about beam position
  rpos= r + rand(1);  %radial position within slice

%entry co-ordinates

     corde(1) = rpos*cos(upsilon);
       corde(2)= rpos*sin(upsilon);
     corde(3)= 0;

% compute the polar and azimuthal angle of entry
    phi= thetae;
    upsin= upsilon;


[z,rho,a] = zprof(comp,dis,period,pos,ceil(corde(1)/4));

   %z= atomic number
   %rho = density
   %a= atomic mass



 gamma= 3.4*(z^0.67)/(1000*e);
 err =0;
 while((corde(3)<thick) & (err==0))


    % charge screening factor

   fact1= 5.21*(z/e)^2*4.0*pi/(10^21);
   fact2= ((e+511)/(e+1022))^2;
   fact3= gamma*(gamma+1);
   sigmae= fact1*fact2/fact3;

  % crossection for elastic scattering.

    lambdap=a/(10^15*6.023*rho*sigmae);

    % in a0
```

```
radiust= abs(log(rand(1))*(-lambdap));

%distance travelled


lb =retzero(100);
rad = retzero(100);



con= ((upsin>=0)&(upsin<=0.5*pi))|((upsin>=1.5*pi)&(upsin<=2.0*pi));

if(con)
    y=1;
    lb(1)= ceil(corde(1)/4)*4;
      rad(1) = abs((lb(1)-corde(1))/(sin(phi)*cos(upsin)));
    if(radiust > rad(1))
      while( radiust > rad(y))
         y=y+1;
        lb(y) = lb(1) + (y-1)*4;
        rad(y)= abs((lb(y)-corde(1))/(sin(phi)*cos(upsin)));
     end
   end
else
  y=1;
  lb(1)= floor(corde(1)/4)*4;
     rad(1) = abs((lb(1)-corde(1))/(sin(phi)*cos(upsin)));
 if (radiust > rad(1))
  while(radiust > rad(y))
      y= y+1;
        lb(y) = lb(1) -(y-1)*4;
     rad(y) = abs((lb(y)-corde(1))/(sin(phi)*cos(upsin)));
   end
  end
end


for i =1:y
  if( rad(i) > radiust)
     rad(i) =0;
  end
end

 radb =retzero(50);

k=0; i=1;
 while((rad(i) ~=0) & (i<=y))
    k= k+1;
  radb(k) = rad(k);
   i = i+1;
 end
```

```
if (k==0)
 k=1;
end

 %locate the positions of boundaries
 rade= abs((thick-corde(3))/cos(phi));
  %radius to exit
 set=0;
if(radiust> rade)
   radiust= rade;
   cordf(3)=thick;
   cordf(1)= radiust*sin(phi)*cos(upsin) +corde(1);
   set=1;
 end
 % compute final position of electron
 if( ~set)
  cordf(1)= radiust*sin(phi)*cos(upsin)+corde(1);
  cordf(3)= radiust*cos(phi)+corde(3);
 end
cordf(2)= radiust*sin(phi)*sin(upsin) +corde(2);
% update lengths and energies
lent =lent + radiust;

s= k;
 for i =1:s
 if  ((upsin>=0)&(upsin<=0.5*pi))|((upsin>=1.5*pi)&(upsin<=2.0*pi))
    [z,rho,a]= zprof(comp,dis,period,pos,ceil((corde(1)+(i-1)*4)/4));
      else
      [z,rho,a]=zprof(comp,dis,period,pos,ceil((corde(1)-(i-1)*4)/4));
   end
 if (i==1)
    if(radiust > radb(1))
        los = loss(z,rho,a,e)*radb(1);
          e = e-los;
            else
        los= loss(z,rho,a,e)*radiust;
      e= e-los ;
    end
  end
if(i~=1)
    if(i~=s)
        los = loss(z,rho,a,e)*((radb(i)-radb(i-1)));
          e= e-los;
          else
       los = loss(z,rho,a,e)*abs((radiust-radb(i-1)));
    end
 end
end

if (corde(1) >0)
  if ((upsin>=0)&(upsin<=0.5*pi))|((upsin>=1.5*pi)&(upsin<=2.0*pi))
     post = ceil(corde(1)/4);
```

```
    for i = 1:s
     if (i==1)
        if(radiust >radb(1))
          rp(post) = rp(post) +radb(1);
             else
          rp(post) = rp(post) +radiust;
       end
    end
if (i~=1)
     if(i~=s)
       rp(post+i-1) = rp(post+i-1) + (radb(i)-radb(i-1));
         else
       rp(post+s-1) = rp(post+s-1) + (radiust-radb(i-1));
        if (radiust < radb(i-1))
         err =1;
       end
    end
  end
  end  % i for loop
else % of upsilon
  post = floor(corde(1)/4);
    diff = s- post;
    if (diff <0)
      if (radiust > radb(1))
        rp(post+1) = rp(post +1) +radb(1);
          else
        rp(post+1) = rp(post+1) +radiust;
      end
 if (s>1)
    for i = 2:s
      if(i~=s)
        rp(post+2-i) = rp(post+2-i)+ (radb(i) -radb(i-1));
          else
       rp(post+2-i) = rp(post+2-i)+ (radiust -radb(i-1));
      if (radiust < radb(i-1))
        err=1;
      end

      end
   end
  end % of s if

 else  % of diff
    if(radiust >radb(1))
      rp(post+1) = rp(post+1) +radb(1);
       else
     rp(post+1) = rp(post+1) +radiust;
   end
if(s>1)
for i = 2:s
  if (post+2-i) > 0
      rp( post+2-i)=rp(post+2-i)+ (radb(i) -radb(i-1));
```

```
          else
         if (i~=s)
          lp(i- (post +1)) = lp(i- (post +1)) + (radb(i) -radb(i-1));
          else
         lp(i- (post +1)) = lp(i- (post +1)) +(radiust-radb(i-1));
        if (radiust < radb(i-1))
           err =1;
          end


      end
    end
  end
end
end % of diff
end % of upsilon
else    % of corde
 if ((upsin>=0)&(upsin<=0.5*pi))|((upsin>=1.5*pi)&(upsin<=2.0*pi))
   post = abs(ceil(corde(1)/4));
  if (radiust > radb(1))
    lp(post +1) = lp(post +1) +radb(1);
     else
    lp(post +1) = lp(post+1) + radiust;
   end
 if(s>1)
  for i = 2:s
    diff = post +1 -s;
     if (diff>0)
       if(i~=s)
         lp(post +2 -i) = lp(post +2 -i) + (radb(i)-radb(i-1));
           else
         lp(post+2-i)  =  lp(post +2-i) + (radiust - radb(i-1));
       end
    else % of diff
   if (post +1-i) >0
    lp(post +2 -i) = lp(post +2 -i) + (radb(i)-radb(i-1));
    else
    if (i~=s)
      rp(i- post ) = rp(i- post ) + (radb(i) -radb(i-1));
       else
      rp(i-post) = rp(i-post ) +(radiust - radb(i-1));
    if (radiust < radb(i-1))
          err=1;
        end


        end
   end
  end
 end
end
else  % of upsin
```

```
  if(radiust > radb(1))
   lp(post +1 ) = lp(post+1) +radb(1);
    else
   lp(post +1) = lp(post +1) + radiust;
  end
if (s>1)
  for i = 2:s
  if(i~=s)
    lp(post+i) = lp(post +i) + (radb(i) -radb(i-1));
      else
    lp(post +i) = lp(post +i) +( radiust -radb(i-1));
  if (radiust < radb(i-1))
          err=1;
        end
end
 end
end
end
end

 if((set)& (lent>0)& (err==0))
   rp = rp/lent;
   lp = lp/lent;
 xfr = (rp+xfr);
 xfl = (lp+xfl);
end

 corde= cordf;
 [z,rho,a] = zprof(comp,dis,period,pos,ceil(corde(1)/4));
 gamma=  3.4*(z^0.67)/(1000*e);
 p= rand(1);
 phi= acos(1.0- 2.0*gamma*p/(1.0+gamma-p));
 upsin= 2.0*pi*rand(1);
          end
   if(err==0)
    count =count+1;
   else
    nu = nu +1;
   end

     end

  end

xfr = xfr/count;
xfl = xfl/count;


 [xfr,lr] = prune(xfr);
 [xfl,ll] = prune(xfl);
```

```
% append the two matrices and generate a continuous distribution


for p = 1:ll
   conpr(p) = xfl(ll-p+1);
 end
   for p= ll+1:ll+lr
      conpr(p) = xfr( p -ll);
 end

total = sum(conpr);
scale = 1.0/total;
conpr = conpr*scale;

xfr = conpr(ll+1:ll+lr);

for i = 1:ll
  xfl(i) =conpr(ll-i+1);
end




function [z,rho,a]= zprof(val,dis,period,pos,n)

%val contains the compostions of Ga.
%dis contains the distances at which these were recorded.
%period is the physical sampling interval.
%pos is the postion of the beam centre.
%n contains the offset to calculate the parameters
%at desired positions.

if (n>0)
      pos1 = pos + ((n-1)*4 +2);
        else
       n = abs(n);
   if (n>0)
      pos1 = pos - (n*4 + 2);
         else
   pos1 = pos- 2;
 end
end
  k= 2.0*inter(val,dis,period,pos1);
  z= k*(-9.0)+ 41;
  a = k*(-45.1) +189.74;
  latp = k*(-0.4054) + 6.059;
  rho1 = 6.641*(k*(-45.1)+189.74);
  rho = rho1/(latp^3);

 % this m file computes the value of the
% function at intermediate points using
% linear interpolation.
```

```
function r= inter(val,dis,period,points)

sz= length(dis);
 len = length(points);

for i = 1:len
 if((points(i))< dis(1))
     r(i) = 0.5;
      else
        if((points(i)) > dis(sz))
         r(i) = 0.5;
          else
     found =0; j=1;
      while((found==0)|(j<sz))
           if(points(i) ==dis(j))
               r(i) =val(j);
              found =1;
             else
               if((points(i)> dis(j))& (points(i)< dis(j+1)))
                 slope = (val(j+1)-val(j))/(dis(j+1) -dis(j));
                r(i) = val(j) + slope*(points(i) -dis(j));
              found =1;
            end
          end
        j=j+1;
      end
    end
   end
  end

% this function estimates the power spectrum.

function [phif,power,es,sig] = weiner(x)

% x is the fourier transform of a given function

% the first thing to do is to ifft and Welch window (Numerical recipes in C)
% Press et al.  pg 554.

seq= ifft(x);
     n = length(seq);
       k = ceil(n/2);
          for i = 1:n
             w(i) = 1.0 - ((i-k)/k)^2;
          end
  wss = sum(w.*w)*n;
  seq = seq.*w;
  fseq = fft(seq);

% now compute a periodogram estimate of the power spectrum.
p(1) =  fseq(1)*conj(fseq(1))/wss;
```

```
for i = 2:k-1
    p(i) = (fseq(i)*conj(fseq(i))+fseq(i)*conj(fseq(i)))/wss;
end
p(k) = fseq(k)*conj(fseq(k))/wss;

% At that point we have an estimate of the power spectrum.
% Next we need to extrapolate the noise to regions of signal power
% in order to estimate the weiner phif.
r= fliplr(p);
  power = [p r];
  l =length(x);
   tail = ceil(0.15*l);
   es = mean(p(k-tail:1:k));
   sig = p -es;
  for i = 1:length(p)
    if(sig(i)>0)
       phif(i) = sig(i)/p(i);
        else
       phif(i) =0;
     end
   end
  rev = fliplr(phif);
 phif = [phif rev];

function [sfilt,avp,phif] = smooth(array)

% this function smooths the supplied array
% by using a weiner optimal filter.
% the first thing to do is to interpolate the profile.

  for i = 1:(length(array(:,1))-2)


  step1 = (array(i+1,1) -array(i,1))/4;
       points = [array(i,1):step1:array(i+1,1)];
        r1= inter(array(:,2),array(:,1),0,points);
          step2 = (array(i+2,1) -array(i+1,1))/4;
       points = [array(i+1,1):step2:array(i+2,1)];
      r2 = inter(array(:,2),array(:,1),0,points);
    tot = length(r1) + length(r2);
   r= [r1 r2];

% next window (Welsh window) and compute the fourier transform
  mid = ceil(tot/2); sum =0;
     for j = 1:tot
          wj = 1.0 - ((j-mid)/mid)^2;
          sum = sum + (abs(wj))^2;
          r(j) = r(j)*wj;
     end
  f = fft(r);
  wss = tot*sum;
```

```
    % compute a power spectrum estimate.
   p(i,1) =  (abs(f(1)))^2/wss;
    for r= 2:mid-1
        p(i,r) = ( (abs(f(r)))^2 + (abs(f(tot-r)))^2)/wss;
    end
   p(i,mid) = (abs(f(mid)))^2/wss;
 end % of the outer for loop (i).

[row,col] = size(p);
  for k = 1:col
     avp(k) = mean(p(:,k));
  end

% use this average value of psd to compute the weiner filter coefficient


 noisep = mean(avp(col-2:1:col));
   sig = (avp -noisep);
    for i = 1: length(avp)
       if (sig(i) >0)
         phif(i) = sig(i)/avp(i);
        else
       phif(i) =0;
     end
  end
favp= fliplr(avp);
  avp = [avp favp];
    fphif = fliplr(phif);
      phif = [phif fphif];
       k= fft(array(:,2));
         k= k';
          k = k.* phif;
        p =abs( ifft(k));
      p=p';
   array(:,2) =p;
sfilt = array;
```

Appendix 3.

TIME RESOLVED PHOTOLUMINESCENCE

One of the practical concerns surrounding ion implantation enhanced quantum well interdiffusion is the effect of the procedure on the optical quality of the implanted structure. As discussed in Chapter 5 of the thesis, it was found that at As^+ doses exceeding $10^{13}/cm^2$ the single and double quantum well structures (SD) exhibited no luminescence. In order to probe the effect of ion implantation on the optical quality of the structure, it is necessary to study the luminescence life times following ion implantation and annealing.

Time resolved photoluminescence experiments were undertaken to determine the influence of implantation on the luminescence decay time. The excitation source for this experiment was a Rhodomin -640 dye laser which produced 5 pico second pulses. This dye laser was pumped by a frequency doubled Nd-YAG, mode locked laser. The excitation wavelength provided by the dye laser was 640 nm. The pulses were spaced ~ 13 nanoseconds apart. Following the acquisition of the luminescence decay, the falling portion of the intensity profile was fitted to an exponential function. This yields a value of (1.21 ± 0.01) nanosecond for the decay time in the case of the 33keV As^+ implanted SD20 structure and 0.71 nanosecond for the 100 keV As^+ implanted SD20 structure. Both samples received a dose of $10^{12}/cm^2$ of As^+ during implantation. Fig A3 provides

a representative spectrum from the 100 keV implanted SD20 structure. In both cases the sample was annealed at 850^0 C for 30 seconds following implantation. The significantly reduced luminescence decay time in the case of the 100 keV implanted structure is noteworthy. The reduced decay time in the case of the 100 keV implanted structure can be attributed to a larger number of defects which are produced by the higher energy implant and consequently can act as non-radiant recombination centres to quench luminescence. It is therefore not very surprising to find that the SD structures implanted with As^+ at 300 keV (dose of $10^{13}/cm^2$) did not luminesce at all after rapid thermally annealing at 850^0 C for 30 seconds. Consequently, as was discussed at some length in section (2.4.2) of the thesis, multiple lower energy implant anneal schemes can be adopted to achieve a greater shift of the band gap and luminescence recovery than a single high energy implant.

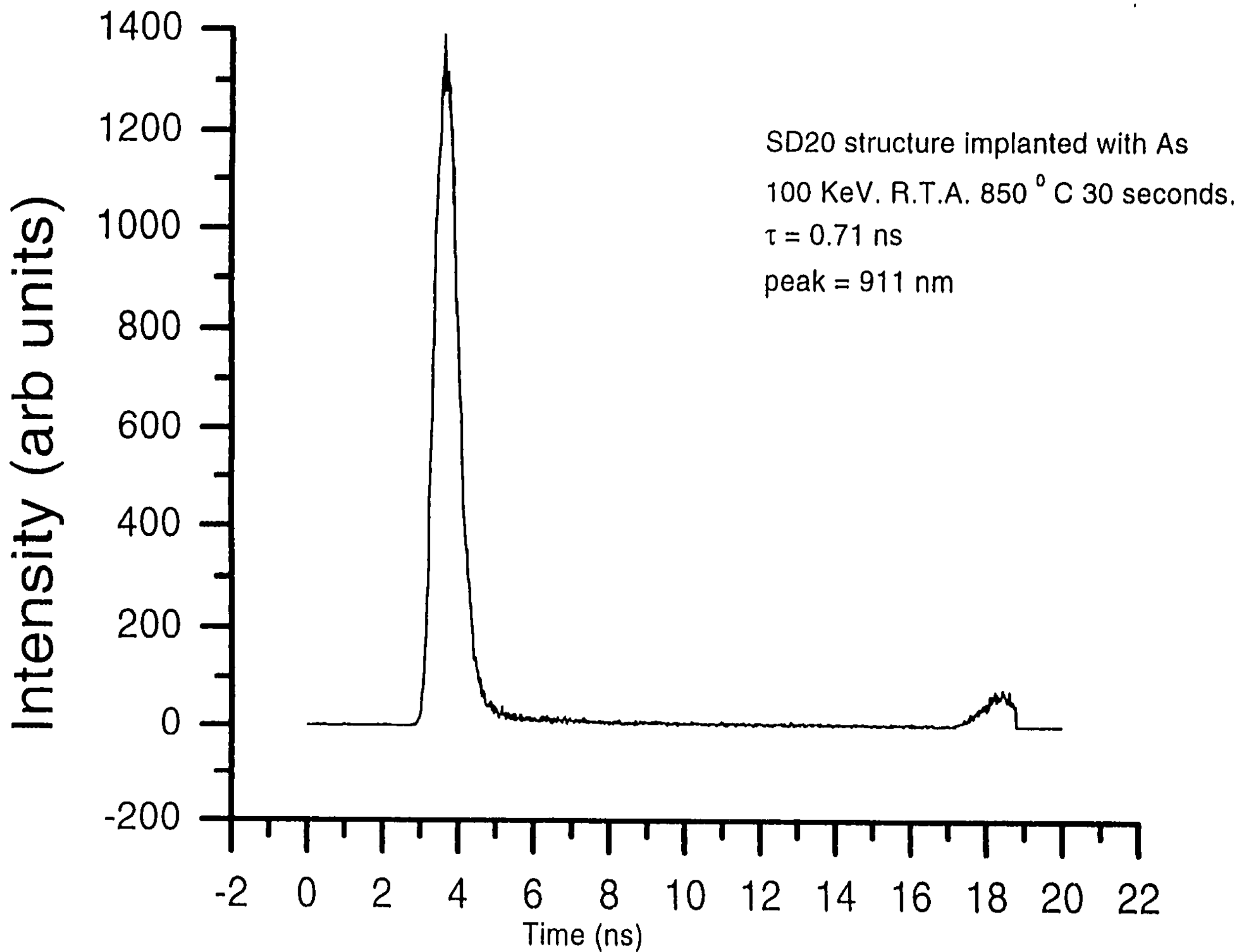

Fig A3 Time resolved spectrum from SD20 structure.

Appendix 4.

TRANSFER MATRIX CODE.

```
% transfer matrix calculation
% Chuang et al. Phy Rev (b) 43 (12) 9649
% Ghatak et al. I.E.E.E. Journal of quantum electronics
% Vol 24 No 8 (1988). (1524).

function [tfc,tfv] = transfer(c,d,pos,st,stp)
   % d: thicknesses are in angstrom.
   % C: concentrations are in fractions of Ga.
   % pos is the array which contains the positions at which
   % the amplitudes are logged.
   % st contains the strains in the structure in plane.
   % stp contains the perpendicular strains.



 % first find the maximum indium content

    maxin = min(c);

  % compute the potential in the well and barrier.
  % This serves as the limits to search for the eigen energies.

  i=1; found =0;
    while((i<=length(c)) & (found~=1))
       if c(i) == maxin
         post=i;
          found =1;
         else
       i= i+1;
    end
  end
 minst = st(post);
 minstp = stp(post);

[dec,deh,vcw,vch,c11,c12,a,b,zi,mh,mc] =params(maxin,minst,minstp);
tc= tmat(dec,vcw,c,d,st,stp,pos,1,vcw,mc,0);
tv= tmat(deh,vch,c,d,st,stp,pos,2,vch,mh,zi);
tfc= tc';
tfv= tv';

function [dec,deh,vc,vh,c11,c12,a,b,zi,mh,mc,ml,ki] = params(comp,st,stp)

% all these values are in electron volt.
```

```
 [deh,dec] = bandoset(comp,st,stp);
  a= -9.77*(comp) -6*(1-comp);
  b= -1.7*(comp) -1.8*(1-comp);
  c11 = 11.88*(comp) + 8.329*(1-comp);
  c12 = 5.38*(comp) + 4.526*(1-comp);
  vh = 2.0*a*(1.0-c12/c11)*st/3;
  vc = 2*vh;
  zi = -b*(1.0+ c12/c11)*st;
  mc= 0.067 - 0.04*(1-comp);
  gamma1 = 6.85*(comp) + 19.67*(1.0-comp);
  gamma2 = 2.1*(comp) + 8.37*(1-comp);
  mh = 1.0/(gamma1- 2.0*gamma2);
  ml = 1.0/(gamma1+ 2.0*gamma2);
  ki = 10.9*comp + 15.15*(1.0-comp);

  function [deltaev,deltaec] = bandoset(comp,st,stp);

 % st contains the value of the inplane strains.
 % stp contains the values of the perpendicular strains.
 % comp is in fraction of gallium
 % Phyrevb 39(3) 1872
 % returns the valence band offset

for i= 1 : length(comp)

      hydrostatic = (stp(i) + 2.0*st(i));

 % compute the position of the average valence band in the strained
 % semiconductor. ( InGaAs)

  latcomp = comp(i)*(-0.4054) + 6.059;
  evavg1= -6.92*comp(i) +(1.0-comp(i))*(-6.67);
  evavg2 = 3.0*comp(i)*(1.0-comp(i))*(-0.16)*(-0.4054)/latcomp;
  deav = 1.16*comp(i) +(1.0-comp(i))*1.00;
  evavg = (evavg1 + evavg2) + deav*hydrostatic ;

% next compute the splitting produced by the shear strains.

  dsoavg = 0.34*comp(i) +(1.0-comp(i))*0.38;
  b = -1.70*comp(i) +(1.0-comp(i))*(-1.8);
  de1= 2.0*b*( stp(i)- st(i));
  shearcor = (dsoavg/3) -0.5*de1;

% finally obtain the position of the heavy hole valence edge

 evlayer = evavg + shearcor;
 evgas = -6.92 + 0.34/3;
 deltaev(i) = abs(evgas-evlayer);


% next compute the positions of the conduction band.
```

```
% first obtain the value of the band gap in the InGaAs.

     ehh = 1.424 -1.06*(1-comp(i)) +0.08*(1-comp(i))^2;
        ecavg = (evavg + shearcor) + ehh;
     deac = -7.17*comp(i) +(1.0-comp(i))*(-5.08);

% finally obtain the position of the starined conduction edge.

     eclayer = ecavg + deac*hydrostatic;
     deltaec(i) =  abs(-5.29- eclayer);


end


function mat = tmat(eu,el,comp,dis,st,stp,pos,k,v1,m1,z1)

 % eu is the upper energy bound
 % el is  the lower energy bound
 % comp is the compostion array
 % dis is the distance array in angstrom
 % pos contains the positions at which the amplitude
 % is logged.
 % K is the number for computation in the valence
 % or conduction band.
 % v1 and m1 are required for the initial value of the
 % tranfer matrix.
 % for now assume that the energy range are divided into
 %  200 steps
 % st,stp are the values of the inplane and the transverse strains.



   step = (eu-el-0.002)/200;
    mat(1,:) = el+0.001:step:eu-0.001; % first row holds energy values.
     counte=0;
       for e= el+0.001:step:eu-0.001 % offset to prevent zeroes for k1.
    count =0;
 %initial value of transfer matrix.
 % assume d1 =0.
      [v2,m2,z2] = smat(comp(1),st(1),stp(1),k,eu);
          k1 = 0.5097*sqrt(m1*(e-z1-v1));
           k2 = 0.5097*sqrt(m2*(e-z2-v2));
          r1= (k1-k2)/(k1+k2);
         t1= 2.0*k1/(k1+k2);
     s(1,1)= 1.0/t1;
     s(2,2)= s(1,1);
     s(1,2)= r1/t1;
     s(2,1)= s(1,2);

  for i = 1:length(pos)
```

```
        if(i==1)
           lower= 1;
             upper = pos(i)-1;
          else
          lower = pos(i-1);
       upper = pos(i)-1;
   end
   for j= lower:upper
      [vj,mj,zj] = smat(comp(j),st(j),stp(j),k,eu);
      [vk,mk,zk] = smat(comp(j+1),st(j+1),stp(j+1),k,eu);
         m= mcomp(vj,mj,zj,vk,mk,zk,e,dis(j));
       s= s*m;
    end  % of j.
   count = count +1;
   ind = (count-1)*2 +1;
 a(ind:ind+1,1:2) =s;

   % log the value of the transfer matrix at this point.

 end % of the i  loop
  for j = pos(i):length(comp)-1
     [vj,mj,zj]= smat(comp(j),st(j),stp(j),k,eu);
     [vk,mk,zk]= smat(comp(j+1),st(j+1),stp(j+1),k,eu);
     m= mcomp(vj,mj,zj,vk,mk,zk,e,dis(j));
   s= s*m;
  end
% at this point we have the transfer matrix for
% the entire structure.
% the matrix a contains the values at the desired points.
% we compute the ratio of amplitudes at the desired points.
  counte = counte +1;
     for i = 1:length(pos)
          ind= (i-1)*2 +1;
            ar1 = a(ind:ind+1,1:2);
             ar2 = inv(ar1)*s;
       mat(i+1,counte)= (abs(ar2(1,1)/s(1,1)))^2;
   end % of i
  end %  of e

function [v,m,z] = smat(comp,st,stp,k,eu)

  if (k==1)
    if (comp ==1)
       % pure GaAs
        v= eu;
         m= 0.067;
         z=0;
    else
      [dc,dh,vc,vh,c11,c12,a,b,zi,mh,mc] = params(comp,st,stp);
      v= (eu-dc)+vc;  % this is necessary to convert to mev.
      m = mc;
      z= 0;
```

```
    end

    else
 if(comp ==1)
    v =eu;
    m = 0.377;
    z = 0;
 else
   [dc,dh,vc,vh,c11,c12,a,b,zi,mh,mc] = params(comp,st,stp);
   v= (eu-dh)+vh; % this is necessary to convert to mev.
   m= mh;
   z= zi;
 end

end

function m = mcomp(vj,mj,zj,vk,mk,zk,e,dis)

  kj = 0.5097*sqrt(mj*(e-zj-vj)); % adjust for mev
   kk = 0.5097*sqrt(mk*(e-zk-vk));
     rj= (kj-kk)/(kj+kk);
      tj= 2*kj/(kj+kk);
       factor = exp(-i*kj*dis);
     m(1,1) = factor/tj;
    m(1,2) = rj*factor/tj;
   m(2,1) = rj/(factor*tj);
  m(2,2) =  1.0/(factor*tj);

function [ latppa,latppe,s,sigma] = latparam(c,d)

% Nakajima J.A.P. 72 5213.
% first compute the matrix of elastic constants.
% concentrations are in the fraction of Ga.

 e= (c - 1.0)*(-.505E-04) + (c)*0.853E-04;
% compute the lattice parameter.
a=   c*(-0.4054) + 6.059;

  term1 = d.^3;
  term2 = sum(e.*term1);
  term3 = (e.*d);
  term4 = (term3./a);
  r1=   sum(term4*term2);
 % to compute terms r2,r3

 sum2= 0;
 sum3 = 0;
for i = 1:length(c)
  for j = 1:length(c)
   if (i~=1)
     k= 1:(i-1);
       t1 = add(a,d,k);
```

```
      else
     t1=0;
    end

   if (j~=1)
     k= 1:(j-1);
     t2 = add(a,d,k);
      else
     t2=0;
   end
   term(j) = 2*t1 -2*t2 +a(i)*d(i) -a(j)*d(j);
   lterm(j) = a(i) -a(j);
 end
  interm1= sum(term4.*term);
  lterm1 = sum(term4.*lterm);
   if (i~=1)
     k= 1:(i-1);
       dar = d(k);
         else
      dar=0;
    end
  interm2= 2*sum(dar) + d(i);

  sum2 = sum2 + 3*term4(i)*interm2*interm1;
  sum3 = sum3 + 6*term4(i)*interm2*lterm1;
 end
 r2 = sum2;
 r3 = sum3;
 r= (r1+r2)/r3;  % computes the value of R.

% compute the face force on each element and hence stress and strain.

 for i = 1:length(c)
   for j = 1:length(c)
     if (i~=1)
       k= 1:(i-1);
       t1= add(a,d,k);
        else
       t1=0;
     end

  if (j~=1)
     k= 1:(j-1);
     t2 = add(a,d,k);
      else
     t2=0;
   end
    fterm1(j) =  t1 -t2 +0.5*(a(i)*d(i) -a(j)*d(j));
    fterm2(j) =  a(j)-a(i);
 end

 f1 = sum(term4.*fterm1);
```

```
f2 = sum(term4.*fterm2);
f3 =  sum(term4);

pre =  e(i)*d(i)/(a(i)*f3);
f(i) = pre*((f1/r) +f2);
s(i) = (f(i)/(e(i)*d(i))) + d(i)/(2*r);

 sigma(i) = e(i)*s(i);
 latppa(i) = a(i)*(1.0 + s(i));
 nu = c(i)*0.31 +(1.0 - c(i))*0.36;
 latppe(i) = a(i)*( 1.0 -(2.0*nu*s(i))/(1.0-nu));
end


function asum = add(a,b,k)

% this function supports the computation of stresses and strains in
% in the hetrostructure.

aar = a(k);
bar = b(k);
asum = sum(aar.*bar);
```

Appendix 5.

CODE FOR THE DIFFUSION CALCULATION.

```
function [cv,ci,c] = conevol(cvi,cin,dis,time,st,j,k)

 % cvi is the concentration of interstials
 % cin is the con of In to start with.
 % time is the time at which the cin is desired.
 % st is the time step to be utilized.
 % j is the upper end of the block containing well and k is lower.

cpov = cvi;
cpoi = cvi;
steps = ceil(time/st);
difv = 1.0E5;
difi = 1.0E6;

for i = 1:steps
    cpin = dsolve(cpoi,cpov,dis,st,2,difi);
    cpvn = dsolve(cpov,cpin,dis,st,1,difv);
    stp = length(cin);
    r=1;  sep =0;
    for q = 1:stp
          slope = (cpvn(j)-cpvn(k))/(dis(j)-dis(k));
           cpn(r) = cpvn(k) + sep*slope;
           disn(r) = dis(k)+ sep*10;
           sep = sep +10; r = r+1;
        end
      cinn = disolve(cin,cpn,disn,st);
   cpoi= cpin; cpov = cpvn; cin =cinn;
 end
cv = cpov; ci = cpoi; c=cin;


function con = dsolve(frac1,frac2,dis,dt,type,dif)

% this function solves the diffusion equation
% and returns updated values for the concentration
% matrix. The concentrations are entered in fractions
% of Ga or the fraction of lattice sites which are
% populated by defects . Time indicates the time at which
% the value of the concentration matrix is desired.
% distances are entered in angstrom.
% dt is the time increment.
```

```
% a diffusivity of 10^-11(v),10^-10(i) cm2 / s is assumed.
% a nearest neighbour jump distance is assumed for the group three lattice.
% also assumed is a 2 ang radius for vacancy. alpa =0.00005 (b ~ 4 angstrom and Rd = 1000 angstrom)
% first  we have compute the values of the C and D matrix.
% type is 1 for vac , 2 for int.

cpo= frac1;
 dx(1) = (dis(2)-dis(1))/2;
   d1 = 2*dx(1);
    [s1,s2] = sink(dx(1),dt,type,0);
     a(1) =  dx(1)/dt + (dif)/d1 ; b(1) = (dif)/d1; c(1) =0;
       d(1)= s1*frac2(1)*dx(1) + cpo(1)*(dx(1)/dt);
         n = length(frac1);
       dx(n) = (dis(n) -dis(n-1))/2;
     a(n) =  dx(n)/dt + (dif)/(2.0*dx(n)); b(n) =0;
   c(n) = (dif)/(2.0*dx(n));
  [s1,s2] = sink(dx(n),dt,type,1);
d(n) = s1*frac2(n)*dx(n) + s2*frac1(n)*dx(n) + cpo(n)*(dx(n)/dt);

[k,p] = max(frac1);

for i = 2:n-1
      dx(i) = 0.5*(dis(i+1) -dis(i-1));
       dxe(i)= dis(i+1)-dis(i);
         dxw(i) = dis(i)- dis(i-1);
           a(i) = (dx(i)/dt) + (dif/dxe(i)) +(dif/dxw(i));
              b(i) =(dif/dxe(i));
                c(i)= (dif/dxw(i));
             if (i<p)
                 [s1,s2] = sink(dx(i),dt,type,0);
                   else
                 [s1,s2] = sink(dx(i),dt,type,1);
            end
       d(i) = s1*frac2(i)*dx(i) + s2*frac1(i)*dx(i) + cpo(i)*(dx(i)/dt);
 end

% we then utilize the TDMA algorithm (Patankar et al.)
% compute the values of P,Q.

 p(1) = b(1)/a(1);
 q(1) = d(1)/a(1);

 for i = 2:n
   p(i) = b(i)/(a(i) - c(i)*p(i-1));
   q(i) = ( d(i) + c(i)*q(i-1))/(a(i) - c(i)*p(i-1));
 end

ncpo(n) = q(n);

for i = n-1:-1:1
  ncpo(i) = p(i)*ncpo(i+1)+q(i);
end
```

```
con = ncpo;


function conin = disolve(cin,cv,dis,dt)

% This function solves the In/AL con evolution with time.
% cin is the initial In con.
% cv is the vacancy con
% dis is the distances.
% dt is the time increment.

 cpo= cin;
  dx(1) = (dis(2)-dis(1))/2;
   d1 = 2*dx(1);
    dp = cv(1)*(0.01)/(5.0E-19); de = cv(2)*(0.01)/(5.0E-19);
     df= 2*dp*de/(dp+de);
      a(1) =  dx(1)/dt + df/d1 ; b(1) = df/d1; c(1) =0;
       d(1)=  cpo(1)*(dx(1)/dt);
        n = length(cin);
        dx(n) = (dis(n) -dis(n-1))/2;
       dp = cv(n)*(0.01)/(5.0E-19);dw = cv(n-1)*(0.01)/(5.0E-19);
      df= 2.0*dp*dw/(dp+dw);
     a(n) =  dx(n)/dt + df/(2.0*dx(n)); b(n) =0;
    c(n) = df/(2.0*dx(n));
  d(n) =   cpo(n)*(dx(n)/dt);

for i = 2:n-1
    dx(i) = 0.5*(dis(i+1) -dis(i-1));
      dxe(i)= dis(i+1)-dis(i);
        dxw(i) = dis(i)- dis(i-1);
          dp = cv(i)*(0.01)/(5.0E-19); de = cv(i+1)*(0.01)/(5.0E-19);
          dw = cv(i-1)*(0.01)/(5.0E-19);
            dfe= 2*dp*de/(dp+de);
             dfw = 2*dp*dw/(dp+dw);
          a(i) = (dx(i)/dt) + (dfe/dxe(i)) +(dfw/dxw(i));
         b(i) =(dfe/dxe(i));
      c(i)= (dfw/dxw(i));
    d(i) = cpo(i)*(dx(i)/dt);
end

% we then utilize the TDMA algorithm (Patankar et al.)
% compute the values of P,Q.

  p(1) = b(1)/a(1);
  q(1) = d(1)/a(1);

  for i = 2:n
   p(i) = b(i)/( a(i)-c(i)*p(i-1));
   q(i) = ( d(i) + c(i)*q(i-1))/(a(i) -c(i)*p(i-1));
  end
```

```
 ncpo(n) = q(n);

 for i = n-1:-1:1
   ncpo(i) = p(i)*ncpo(i+1)+q(i);
 end

conin = ncpo;

function [s1,s2] = sink(thick,dt,type,inc)

% thick is the thickness of the section in the F.D. calculation
% dt is the time increment
% type is the flag for int or vac calculation.(1=vac 2 =int)
% inc is the flag for inclusion of both vac recombination
% (inc=1 for both)
% and dislocation elimination

 if (type ==1)
   s1= eli(2,thick,dt); s2=0;
  else
   if (inc==0)
    s1= eli(2,thick,dt); s2=0;
      else
    s1= eli(2,thick,dt); s2= disl(dt);
  end
 end


function frac = disl(time)

 % this function computes the fraction of interstials
 % trapped at dislocations

 term1 = 0.00005^2*8*time/(4.65*(1.0E-6));
 frac = (exp(-term1) -1)/time;

function frac = eli(a,b,time)

 % b is the distance of the vacancy
 % a is the vacancy radius.

 term1 = 1.0 -a/b;
 term2 = (a/b)*erf((b-a)/(2.0*100000*time));
 f = term1 + term2;
 frac = (f-1)/time;
```

Appendix 6

CONTRAST COMPUTATION WITH THE TWO BEAM THEORY OF DYNAMICAL DIFFRACTION.

The purpose of this appendix is to demonstrate that the two beam dynamical theory of electron diffraction can be employed to compute the contrast from annealed superlattice SL10 structures. This would support the interpretation of the micrographs 4.1.4 and 4.1.5 shown in Chapter 4 of the thesis.

In the two beam theory of electron diffraction, electron wave propagation in the crystal is described in terms of a transmitted wave and a diffracted wave. (Hence the name two beam theory). In the first approximation absorption is neglected and the variation in intensity of the transmitted and the diffracted wave as a function of depth in an undistorted crystal is described in terms of two coupled ordinary differential equations:

$$d\phi_0/dz = (\pi i/\varepsilon_g)\,\phi_g \quad ..A6.1$$

$$d\phi_g/dz = (\pi i/\varepsilon_g)\,\phi_0 + 2\,\pi i s \phi_g \quad ..A6.2$$

In the above equations ϕ_0 and ϕ_g are the amplitude of the transmitted and the diffracted wave respectively. z indicates the direction of propagation. s is the deviation from the Bragg position. The parameter ε_g is called the extinction distance and is given by

$$\varepsilon_g = \pi V_c \cos(\theta_b) / F_g \qquad ..A6.3$$

In equation A6.3 V_c is the volume of the unit cell of the crystal, and F_g is the structure factor for the diffracting plane. θ_b is the Bragg angle.

For the case of the undistorted crystal the coupled differential equations (A6.1 and A6.2) can be solved to yield the intensity of the transmitted and diffracted wave at a depth t in the crystal. The solution for this case can be shown to be [99]:

$$\left|\phi_g\right|^2 = (\pi/\varepsilon_g)^2 \sin^2(\pi t s_{eff})/(\pi s_{eff})^2 \qquad ..A6.4$$

In equation A6.4 s_{eff} is related to the deviation from the Bragg position s and the extinction distance ε_g through the equation

$$s_{eff} = \sqrt{s^2 + 1/\varepsilon_g^2} \qquad ..A6.5$$

In order to calculate the contrast from the diffused superlattice structure SL10, an estimate of the indium concentration profile is obtained through the linear diffusion model outlined in section 5.1 of Chapter 5. Subsequently the strain in the structure can be obtained through the method outlined in section 5.1.2. If the crystal is set such that the substrate region is in an 'edge on' position with respect to the (002) reciprocal lattice

vector, it is possible to compute the contrast from the diffused structure utilizing equation A6.4. The contrast depends on the thickness of the crystal. Normally TEM foils are wedge shaped. However in this simplified calculation the foil is assumed to be of constant thickness. (500 $\overset{0}{A}$). The calculation is based on the column approximation. In this approximation the local value of the deviation s and the extinction distance ε_g are used to compute the contrast from a selected slice (column) of the sample. The contrast due to the entire sample is then obtained by considering a number of such slices.

Fig A6 shows the indium concentration profile from the SL10 superlattice structure diffused at 850^0C for 12 hours and the corresponding computed contrast. The dark region corresponding to the homogenized superlattice and the bright tail can easily be discerned. The edge of the sample has been clipped in the process of sample preparation and consequently the rising edge on the left seen in Fig A6 cannot be discerned in micrograph 4.1.5. This computation suggests that the contrast seen in micrograph 4.1.5 arises from a region that is slightly enriched in indium. This situation is to be expected on long term (several hours) annealing.

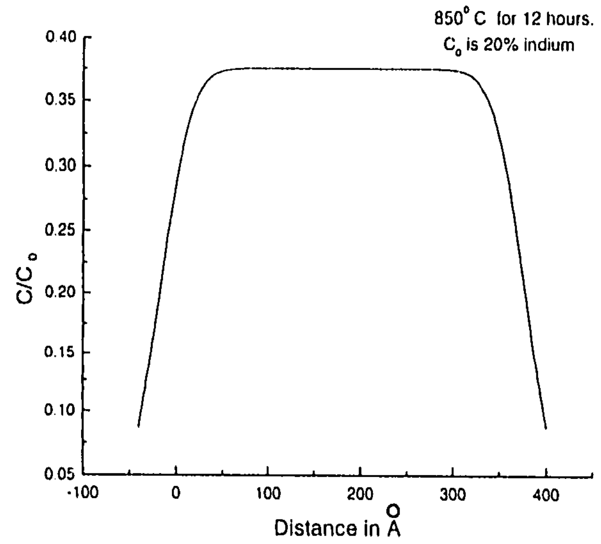

Fig A6.1 Indium concentration profile.

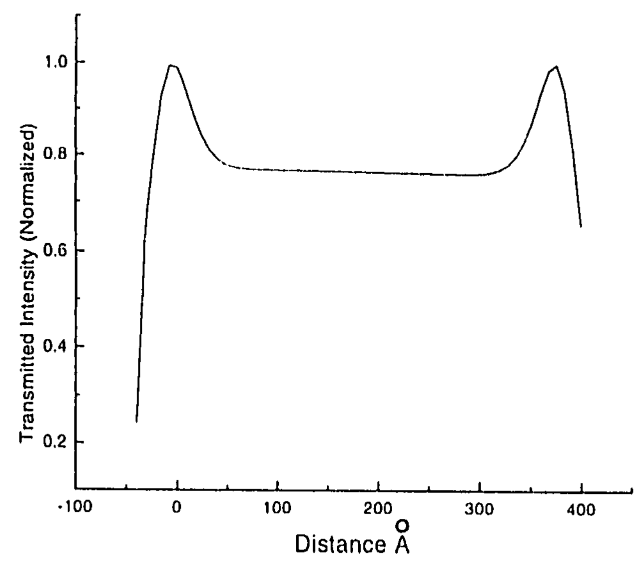

Fig A6.2 Computed transmitted intensity.

REFERENCES.

[1] Okada.T., Ph.D. thesis McMaster University (1996).

[2] Grovenor.C.R.M., 'Microelectronic Materials' Institute of Physics publishing (1989).

[3] Adachi.S., Journal of Applied Physics (53) 8775 (1982).

[4] Nahory.R.E., Pollack.M.A., Johnston.W.D., Barns. R.L., Applied Physics Letters (33) 659 (1978).

[5] Stringfellow.G.B., Journal of Crystal Growth (58) 194 (1982).

[6] Norman.A.G., Booker.G.R., Journal of Applied Physics (57) 4715 (1985).

[7] McDevitt.T.L.,Mahajan.S.,Laughlin.D.E., Bonner.W.A., Keramidas.V.G., Physical Review (B) (45) 6614 (1992).

[8] Peiro.F.,Cornet.A.,Morante.J.R.,Clark.S.,Williams.R.H., Applied Physics Letters (59) 1957 (1991)

[9] Glas.F., Journal of Applied Physics (62) 3201 (1987).

[10] Lapierre.R.R., Master's thesis McMaster University (1994).

[11] Philips.B.A.,Norman.A.G.,Seong.T.Y.,Mahajan.S., Booker.G.R., Skowronski.M., Harbison.J.A., Keramidas.V.G., Journal of Crystal Growth (140) 249 (1994).

[12] Spencer.B.J., Voorhees.P.W., Davis.S.H., Journal of Applied Physics 73(10) 4955 (1993).

[13] Solomon.G.S., Trezza.A., Marshall.A.F., Harris.J.S., Physical Review Letters 76(6) 952 (1996).

[14] Grundmann.M., Ledentsov.N.N., et al. Physica Status Solidus (b) (188) 249 (1995).

[15] Bimberg.D., Ledentsov.N.N., et al. Physica Status Solidus (b) (194) 159 (1996).

[16] Fafard .S., Leonard .D., Mertz.J.L., Petroff .P.M., Applied Physics Letters 65(11) 1388 (1994).

[17] Tan.T.Y., Gosele.U., Yu.S., Critical reviews in Solid State and Material Science 17(1) 47 (1991)

[18] Guido.J., Holonyak.N., Hseih.K.C., Kaliski.R.W., Plano.W.E., Burtham.P.D., Thorton.R.L., Epler.J.E., Paoli.T.L., Journal of Applied Physics (61) 1372 (1987).

[19] Mei.P., Yoon.H.W., Venkatesan.T., Schwarz.S.A., Harbison.J.P., Applied Physics Letters(50) 1823 (1987).

[20] Deppe.D.G., Holonyak.N.Jr, Journalof Applied Physics (66) R93 (1988).

[21] Zucker.E.P., Hashimoto.A., Fukunaga.T., Watanabe.N., Applied Physics Letters (54) 564 (1989).

[22] Fleming.R.M., McWhan.D.B., Gossard.A.C., Weigmann.W., Logan.R.A., Journal of Applied Physics (51) 357 (1980).

[23] Joncour.M.C., Charasse.M.N., Burgeat.J., Journal of Applied Physics 58(9) 3373 (1985).

[24] Wong.S.L., Nicholas.R.J., Martin.R.W., Thomson.J., Wood.A., Moseley.A., Carr.N., Journal of Applied Physics 79(9) 6826 (1996).

[25] Gerald.B., 'Wave mechanics applied to semiconductor heterostructures 'Halsted Press. New York. (1988).

[26] Dingle.R., Festkoper Probleme XV 21 (1975).

[27] Tsu.R., Esaki.L., Applied Physics Letters (22) 562 (1973).

[28] Esaki.L., Chang.L.L., Physical Review Letters (33) 495 (1974).

[29] Esaki.L., Tsu.R., IBM Journal of Research (14) 61 (1970).

[30] Dingle.R., Weigmann.W., Henry.C.H., Physical Review Letters (33) 827 (1974).

[31] Van Der Ziel .J.P., Dingle .R., Miller.R.C., Weigmann.W., Nordland.W.A., Applied Physics Letters (26) (8) 463 (1975).

[32] Nakamura .S., Physics World (11)2 31 (1998).

[33] Bhattacharyya.P.K., Dutta.N.K., Annual Review of Materials Science (23) 79

(1993).

[34] Kittel.C., ' Introduction to Solid State Physics' Wiley (1986).

[35] Colley.P.Mcl., Lightowlers.E.C., Semiconductor Science and Technology (2) 157 (1987).

[36] Colbourne.D.P., Cassidy.D.T., IEEE Journal of Quantum Electronics Vol(29), No1, 62 (1989).

[37] Hovel.H.J., Semiconductor Science and Technology (7) A1-A9 (1992).

[38] Biersack.J.P., Haggmark.L.G., Nuclear Instruments and methods (174) 257 (1980).

[39] Ziegler.J.F., Biersack.J.P., Littmark.U., ' The stopping and range of ions in solids' Permagon Press (1985).

[40] Lindhard.J., Scharff.M., Physical Review (124) 128 (1961).

[41] Brandt.W., Kitagawa.M., Physical Review (b) (25) 5631 (1982).

[42] Allard.L.B., Aers.G.C., Charbonneau.S., Jackman.T.E., Williams.R.L., Templeton.I.M., Buchanan.M., Stevanovic.D., Almeida.F.J.D., Journal of Applied Physics (72) 422 (1992).

[43] Charbonneau.S., Poole.P.J., Piva.P.G., Aers.G.C., Koteles.E.S., Fallahi.M., He.J.J., McCaffrey.J.P., Buchanan.M., Dion.M., Golberg.R.D., Mitchell.I.V., Journal of Applied Physics 78 (6) 3697 (1995).

[44] Charbonneau.S., Poole.P.J., Feng.Y., Aers.G.C., Dion.M., Davies.M., Goldberg.R.D., Mitchell.I.V., Applied Physics Letters 67 (20) 2954 (1995).

[45] Poole.P.J., Charbonneau.S., Aers.G.C., Jackman.T.E., Buchanan.M., Dion.M., Goldberg.R.D., Mitchell.I.V., Journal of Applied Physics 78 (4) 2367 (1995).

[46] Wan.J.Z., Simmons.J.G., Thomson.D.A., Journal of Applied Physics (81) 765 (1997).

[47] Cibert.J., Petroff.P.M., Werder.D.J., Pearton.S.J., Gossard.A.C., English.J.H., Applied Physics Letters (49) 223 (1986).

[48] Piva.P.G., Poole.P.J., Charbonneau.S., Koteles.E.S., Buchanan.M., Aers.G.C., Roth.A.P.,Wasilewski.Z.R.,Beauvais.J.,Goldberg.R.D., Superlattices and Microstructures 15(4) 385 (1994).

[49] Cibert.J., Petroff.P.M., Physical Review (B) (36) 3243 (1987).

[50] Matthews.J.W., Blakeslee.A.E., Journal of Crystal Growth (29) 273 (1975).

[51] Edmondson.B., Williamson.G.K., Philosophical Magazine (9) 277 (1964).

[52] Poole.P.J., Charbonneau.S., private communication.

[53] Digital Micrograph 2.1 Gatan Inc (1994).

[54] Bracewell.R.N., 'The Fourier Transform and it's applications'. McGrawHill New York (1965).

[55] Nakajima.K., Journal of Applied Physics 72 (11) 5213 (1991).

[56] Sales.K.D. Acta Crystallographica (A) (43) 42 (1987).

[57] Greer.A.I., Spaepen.F., in 'Synthetic Modulated Structures ' ed Chang.L.L., Geisen.B.C., Academic Press Orlando (1985).

[58] Van De Walle.C.G., Physical Review (b) 39 (3) 1871 (1989).

[59] Ghatak.A.K., Thyagarajan.K., Shenoy.M.R., I.E.E.E. Journal of Quantum Electronics 24 (8) 1524 (1988).

[60] Chaung.S.L., Physical Review (b) 43 (12) 9649 (1991).

[61] Weisbuch.C., Vinter.B., 'Quantum Semiconductor Devices' Academic Press Boston (1991).

[62] Cullis.A.G., Pidduck.A.J., Emeny.M.T., Journal of Crystal Growth (158) 15 (1996).

[63] Shewmon.P.G., ' Diffusion in Solids' McGraw Hill New York (1963).

[64] Larche.F., Cahn.J.W., Acta Metallurgica Vol(30) 1835 (1982).

[65] Purdy.G.R., Brechet.Y.M., Acta Materialia Vol 44 (12) 4853 (1996).

[66] Hinckley.J.M., Singh.J., Physical Review (b) (42) 3546 (1990).

[67] Los.J., Fasolino.A., Catellani.A., Physical Review (b) 53 (8) 4630 (1996)

[68] Gillin.W.P., Sealy.B.J.,Homewood.K.P., Optical and Quantum Electronics (23) S975 (1991).

[69] Myers.S.M.,Amos.D.E., Brice.D.K., Journal of Applied Physics (47)1812 (1976).

[70] Posselt.M., Schmidt.B., Murthy.C.S., Fuedal.T., Suzuki.K., Journal of the Electrochemical Society 144 (4) 1495 (1997).

[71] Conrad.U., Urbassek.H.M., Radiation effects and defects in solids (127)27 (1993).

[72] Sayed.M., Jefferson.J.H., Walker.A.B., Cullis.A.G., Nuclear Instruments and Methods in Physics Research (b) (102) 218 (1995).

[73] Ourmazd.A., Scheffer.M. M.R.S. Bulletin XV 24 December (1992).

[74] Brown.W.L., Fletcher.R.C., Wright.K.A., Physical Review (92) 591 (1953).

[75] Chao.H.S., Crowder.S.W., Griffin.P.B., Plummer.J.D. , Journal of Applied Physics (79) 2352 (1996).

[76] Park.H.Y., Jones.K.S., Law.M.E., Journal of the Electrochemical Society 141 (3) 759 (1994).

[77] Liu.J., Chaudry.S., Jones.K.S., Law.M.E., Solid State Electronics 38 (7) 1305 (1995).

[78] Patankar.S.V., ' Numerical Heat Transfer and Fluid Flow' McGrawHill New York (1980).

[79] Braun.W., Trampert.A., Dawerzitz.L., Ploog.K.H., Journal of Crystal Growth 175/176 part 1 156 (1997).

[80] Piva.P.G., Poole.P.J., Buchanan.M., Champion.G., Templeton.I., Aers.G.C., Williams.R., Wasilewski.Z.R., Koteles.E.S., Charbonneau.S., Applied Physics Letters 65 (5) 621 (1994).

[81] Poole.P.J., Piva.P.G., Buchanan.M., Aers.G.C., Roth.A.P., Dion.M., Wasilewski.Z.R., Koteles.E.S., Charbonneau.S., Beauvais.J., Semiconductor Science and Technology (9) 2134 (1994).

[82] Chou.C.T., Cockyane.D.J.H., Zou.J., Krinh∅j.P., Jagadish.C., Physical Review (b) (52) 17223 (1995).

[83] Tersoff .J., Physical Review Letters (65) 887 (1990).

[84] Bode.M., Ourmazd.A., Cunningham.J., Hong.M., Physical Review Letters 67 (7) 843 (1991).

[85] Nagle .J., Landesman.J.P., Larive.M., Mottet.C., Bois.P., Journal of Crystal Growth (127) 550 (1993).

[86] Muraki.K., Fukatsu.S., Shiraki.Y., Ito.R., Journal of Crystal Growth (127) 546 (1993).

[87] Kinchin.G.H., Pease .R.H., Reports on progress in Physics Vol XVIII 1 (1955).

[88] Weiss.G.H., Havlin.S., Journal of Statistical Physics (37) 17 (1984).

[89] Koteles.E.M., Elman.B., Melman.P., Chi.J.Y., Armeinto.C.A., Optical and Quantum Electronics 23 (7) 779 (1991).

[90] Shi.S., Kam Wa Li.P., Miller.A., PamulaPati.J., Cooke.P., Dutta.M., Semiconductor Science and Technology (9) 1564 (1994).

[91] Ooi.B.S., Hamilton.C.J., McIlvaney.K., Bryce.A.J., DelaRaue.R.M., Marsh.J.H., Roberts.J.S., I.E.E.E . Photonics Technology Letters. 9 (5) 587 (1997).

[92] Joy.D.C. , EUREM 88 proceedings 1 23 (1988).

[93] McGibbon.A., Ph.D. thesis Glasgow University (1987).

[94] Bishop.H.E., in 'Use of Monte Carlo Calculations in electron probe microanalysis and scanning electron microscopy' eds Heinrich.K.F.J., et al. NBS publication 5 (1976).

[95] Bethe.H.A., Annalen . de. Phys . (5) 325 (1930).

[96] Berger.M.J., Selzer.S.M., Nat. Acad. Sci. Nat. Res. Council Pub (1133) 205 (1964).

[97] Matlab4. The Math Works Inc (1994).

[98] Press.W.H., Teukolsky.S.A., Vetterling.W.T., Flannery.B.P. ' Numerical Algorithms in C. The art of scientific programming .' Cambridge University Press New York (1988).

[99] Hirsch.P., Howie.A., Nicholson.R.B., Pashley.D.W., Whelan.M.J., ' Electron microscopy of thin crystals.' Robert . E. Krieger Publishing Company Malabar Florida (1977).